

IN-SITU ELECTROCHEMICAL SPECTROSCOPY AND PROBE MICROSCOPY STUDIES OF
ELECTRODEPOSITION

BY

JEREMY JAY HATCH

DISSERTATION

Submitted in partial fulfillment of the requirements
for the degree of Doctor of Philosophy in Chemistry
in the Graduate College of the
University of Illinois at Urbana-Champaign, 2011

Urbana, Illinois

Doctoral Committee:

Professor Andrew A. Gewirth, Chair
Professor Gregory S. Girolami
Assistant Professor Ryan C. Bailey
Professor Paul V. Braun

ABSTRACT

Electrodeposition is widely used for industrial applications to deposit films, coatings, and adhesion layers. The diversity of materials that can be deposited has led to numerous studies of electrodeposition processes. This thesis explores two electrochemical systems: 1) the electrodeposition of chromate to form thin films on Au, and 2) the effect of functionalization and concentration on the behavior of quaternary ammonium levelers proposed for electroplating Cu in through-silicon vias (TSVs).

The first study investigates the mechanism and morphology of chromate deposition, a process of which has significant importance both industrially and environmentally. Electrodeposition of chromate on Au was studied using cyclic voltammetry (CV), surface enhanced Raman spectroscopy (SERS), *in-situ* electrochemical scanning tunneling microscopy (EC-STM), and *in-situ* electrochemical atomic force microscopy (EC-AFM). CV results show the evolution of the deposited species as a function of scan cycle. SERS reveals the presence of intermediate species during the deposition process as well as the dual mixed Cr^{III}/Cr^{VI} nature of the surface oxide film that is formed. *In-situ* EC-AFM shows that the reduced form of the oxide film, α -Cr₂O₃, is oriented in a (3×3)R30° adlattice relative to the Au(111) surface. A mechanism for the electrodeposition of chromate on Au is proposed based on the results of this study.

The second electrochemical system explored in this thesis revolves around Dodecyltrimethyl ammonium bromide (DTAB), benzyldimethylhexadecyl ammonium chloride (BDAC) and thonzonium bromide (ThonB) and their potential use as leveling

additives. Electroplating measurements show that while each of the proposed levelers inhibits the onset of bulk Cu deposition at a Cu(poly) disk electrode, the concentration and potential dependence of this behavior depends on the functionalization of the additive. Surface enhanced Raman spectroscopy (SERS) results show that DTAB displays no potential dependent behavior, while both BDAC and ThonB exhibit substantial potential dependent behavior, the nature of which depends on headgroup functionality. This study demonstrates that functionalization of amphiphilic quaternary ammonium surfactants can have a significant impact on the effectiveness of the leveler.

Dedicated to my family and friends; in particular, to my wife Mary and our children Kimberly, Jennifer, Timothy, and Jason.

Acknowledgments

My time here at the University of Illinois at the Urbana-Champaign campus has had a great influence on me as a person and a scholar. I have learned a lot about myself in addition to the technical skills that I have acquired. As my graduate studies come to a close, I wish to give thanks to those that took part in this stage of my life.

To my advisor, Andrew Gewirth, I am grateful for the support that he has supplied throughout my graduate career. Andy was always there to provide guidance and support. His counsel was always insightful and often presented a way to approach a problem that I had not previously considered. I could tell that he always wanted to see me succeed.

Special thanks go to my committee members: Greg Giralomi, Ryan Bailey, and Paul Braun. I appreciate the time and effort they put into their work. I am grateful for the advice and support that I have received from them.

I would be truly ungrateful if I did not acknowledge my fellow Gewirth Group members, both present and past. Tighe Spurlin, Scott Shaw, Karen Stewart set an excellent example as senior group members. I would like to thank Ezra Egberton for his help in learning the basics of surface enhanced Raman spectroscopy. Sung Ean Bae was instrumental in teaching me how to do electrochemical scanning tunneling microscopy. Andrew Campbell taught me about atomic force microscopy. I would also like to thank Matt Thorum for his insightful comments, searching questions and outdoor activities. The rest of the group members have been wonderful companions through this arduous task, thanks to Matt Thorseth, Joe Buthker, Brandon Long, Dennis Butcher, Claire Tornow,

Clinton King, Nicole Honesty, Laura, Tom, Adele and the many others that visited our group as fellow researchers and collaborators.

Finally, I would like to thank my family for their enduring support of my educational pursuits and goals. My wife Mary was there with me through the ups and downs, the long nights, and stressful burdens that accompany graduate school and rearing a family. Her love and kindness gave me strength to persevere. My children, Kimberly, Jennifer, Timothy and Jason, gave me joy and a burning desire to complete what I had started.

I could not have completed my education without the support and encouragement of all of those who stood with me, thank you.

Table of Contents

CHAPTER 1. INTRODUCTION	1
CHAPTER 2. EXPERIMENTAL	25
CHAPTER 3. POTENTIAL DEPENDENT CHROMATE ADSORPTION ON GOLD	46
CHAPTER 4. INFLUENCE OF AROMATIC FUNCTIONALITY ON QUATERNARY AMMONIUM LEVELERS FOR CU PLATING.....	74
APPENDIX A. CORROSION OF 316L STAINLESS STEEL, HAYNES ALLOY 230, AND HAYNES ALLOY 617	99
APPENDIX B. ROUGHENING MACROS.....	116
APPENDIX C. COLLET DESIGN FOR ROTATING EXPERIMENTS.....	118
APPENDIX D. EC-STM FLUID CELL	119
APPENDIX E. SUPPLEMENTAL INFORMATION TO CHAPTER 4.....	120
AUTHOR'S CURRICULUM VITAE	121

Chapter 1. Introduction

1.1. Electrode-Solution Interface

Investigation of the reactions that occur at the electrode-solution interface is relevant to a diverse range of electrochemical processes, such as corrosion,¹⁻³ deposition,⁴⁻⁶ electrorefinement of metals,^{7, 8} energy storage⁹ and catalysis.^{10, 11} As such, there is great interest in understanding the kinetic and mechanistic properties of the electrochemical reactions which transpire in the electrode-solution interfacial region. The work presented in this thesis appertains to the formation of thin films via electrodeposition.

Electrodeposition is broadly defined as the process by which a material is deposited by passing current through an electrolytic solution resulting in the formation of an insoluble product which forms on the electrode surface and includes processes such as electroplating, underpotential deposition, and electrophoretic painting.¹² Electrodeposition can occur at either the anode or the cathode; for example, electroplating metal is a reductive process taking place at the cathode while some electrophoretic paints are applied using an anodic process. Although electrodeposition can be used for the formation of bulk deposits, it is used widely in industry to deposit thin films on substrates in order to achieve new surface properties such as corrosion resistance.

The significance of understanding the processes which occur in the electrode-solution interfacial region has led to the development of several surface sensitive techniques: scanning tunneling microscopy, atomic force microscopy, surface infrared

spectroscopies, surface Raman spectroscopies, electrochemical quartz crystal microbalance, and others.¹³ These techniques can be divided into two basic groups: surface morphology mapping and chemical identification. The combination of these methods together with *in-situ* electrochemical control can provide deep insight into the mechanistic and morphologic changes that occur as electrochemical processes take place.

Scanning probe microscopies, scanning tunneling microscopy (STM) and atomic force microscopy (AFM) in particular, are extremely useful for probing changes made to the morphology of the surface. The STM was developed by Binnig and Rohrer in 1982 at IBM Zurich.¹⁴ The STM is capable of a mapping out atomic-scale (as well as larger) structural images of conducting substrates by probing the electron density of surface states.¹⁵ The atomic-scale resolution is achievable because of the sensitivity of the tunneling current to the distance, $W(\text{\AA})$, between the tip and substrate. The correlation of distance to tunneling current is given in Equation 1.1.¹⁵

$$i_t \propto \rho_s(0, E_F) e^{-1.025\sqrt{\phi \cdot W}} \quad (1.1)$$

where i_t is the tunneling current, ρ_s is the local density of states, ϕ is the work function of the substrate, and E_F is the Fermi level of the substrate. The exponential proportionality of current and distance allows for vertical resolution (z perpendicular to the surface) of less than 0.1 \AA and a lateral resolution (x and y parallel to the surface) on the order of 1 \AA .¹⁵ A typical STM experiment is carried out by bringing a sharp metal tip (often W or PtIr alloy) into close proximity with a conductive substrate, on the order of 1 nm. At this distance the statistical instance of electron tunneling is high.¹⁵ By applying a bias voltage between the

tip and substrate, a tunneling current is induced. The tunneling current is converted to voltage which is then amplified and compared to a reference voltage corresponding to the current setpoint that was chosen with the STM software. The z axis piezoelectric device is used to equalize the difference between the tunneling and setpoint currents by adjusting the height of the tip relative to the surface according to the difference between the two voltages in the feedback loop. The tip is rastered across the surface in the x and y plane by applying a saw-tooth voltage to the x piezoelectric device and ramping the voltage of the y piezoelectric device with each step in the x direction. Thus, the recorded changes in the z direction combined with the successive line-scans in the x and y directions provides a topographical image of the substrate's surface. AFM was invented by Binnig, Quate, and Gerber in 1986 at IBM Zurich.¹⁶ AFM is similar to STM in that a sharp tip is rastered across the surface of the substrate utilizing a piezoelectric device. In contrast to STM, AFM does not require that the substrate be conductive, and the tip is often brought into contact with the surface. In AFM the tip (often Si₃N₄) is attached to a cantilever. A laser is reflected off of the cantilever onto a position sensitive CCD detector. As the tip is rastered across the surface, it is deflected by forces that exist between the tip and the surface in accordance with Hooke's Law (Eqn. 1.2)

$$F = -kx \tag{1.2}$$

where F is the restoring force exerted by the cantilever, k is the spring constant, and x is the displacement of the cantilever from its equilibrium state. These deflections are detected by changes in the laser position on the detector, producing a topographical map of the surface.

In this thesis, surface enhanced Raman spectroscopy (SERS), was utilized to determine chemical speciation during electrochemical experiments. SERS was first observed by Fleischman *et al.* in 1974¹⁷; although they attributed the unusually high quality signal to an increase in surface concentration of the analyte as a result of the increased surface area the roughened Ag electrode that they were using. Jeanmarie and Van Duyne¹⁸, as well as Albrecht and Creighton¹⁹, later discovered that the signal increase observed by Fleischman *et al.*, was actually a product of “surface enhancement” of the Raman cross section.

SERS follows the same selection rules as normal Raman spectroscopy; the analyte is considered Raman active if there is a net change in the polarizability of the molecule as it vibrates.²⁰ Polarizability is a proportionality constant that describes the ease of inducing a dipole moment in a molecule via an electric field.²⁰

$$\alpha = \frac{\mu_i}{E} \quad (1.3)$$

where α is the polarizability of the molecular bond, μ_i is the induced dipole moment, and E is the electric field which induces the dipole. This interaction of the electric field of the impinging light with the molecule can be visualized as a change in the shape of the electron cloud of the molecule.

The coupling of the electric field vector with the induced dipole relates to the sum of the cosines of the incident frequency of light (ν_0), the incident frequency plus the frequency of the molecular vibrations ($\nu_0 + \nu_k$), and the incident frequency minus the frequency of the molecular vibrations ($\nu_0 - \nu_k$) shown in Eqn. 1.4.²¹

$$\mu_i = \alpha_0 E_0 \cos(2\pi\nu_0 t) + \frac{\alpha_k E_0}{2} \{ \cos[2\pi(\nu_0 + \nu_k)t + \phi] + \cos[2\pi(\nu_0 - \nu_k)t - \phi] \} \quad (1.4)$$

The coupling behavior, $(\nu_0 + \nu_k)$ and $(\nu_0 - \nu_k)$, can cause a shift in energy of the scattered light directly correlated to the energy of the molecular vibrations of the molecule. However, the statistical instance of an inelastically scattered photon from a molecule is about 1 in 10^7 photons scattered.²¹ This low instance of Raman scattered light requires that a high concentration of the analyte as well as an intense uniform light source (*i.e. a laser*). These conditions limit the use and practicality of normal Raman spectroscopy, nevertheless, the enhancements observed in SERS make it possible to acquire signal from very dilute systems.

The surface enhancement observed in the SERS experiment is two-fold: there is an electromagnetic field enhancement (EM) and a smaller chemical enhancement (CE).²²⁻²⁴ The EM enhancement is considered to be the largest contributor of the two enhancement mechanisms. The relationship of the SERS intensity to the enhancement mechanisms can be approximated as shown in Eqn. 1.5.²⁴

$$I_{SERS} \propto G_{EM} \sum_{\rho, \sigma} |(\alpha_{\rho\sigma})_{nm}|^2 \quad (1.5)$$

In the presence of a metal surface the enhancement factor from the EM fields of the incident light and the scattered light on the surface are represented by G_{EM} . The EM enhancement is directly related to the interaction of the incident light and the substrate. It is governed by the optical properties of the substrate, the wavelength of the incident light, and the morphology of the surface.²⁴ The process of enhancement involves several

phenomena such as the excitation of the surface plasmon and the lightning-rod effect.²³ The molecule specific part of the relationship, the sum term $(\alpha_{\rho\sigma})_{nm}$ gives rise to the CE enhancement factor. CE enhancement occurs only when a molecule is chemisorbed to a surface and involves the photon-driven charge transfer between the molecule and surface and the coupling of the electron-hole pair and the adsorbed molecule.^{22, 24} The nature of the enhancement mechanisms necessarily makes SERS a surface sensitive technique.

1.2. Uses and Remediation of Chromate

Chromium(VI) oxoanions have broad industrial applications and large environmental implications which have generated considerable interest.²⁵⁻³⁴ Aside from chrome plating, chromate and its polymers have been used in paper milling, leather tanning, as pigments, adhesion layers and in corrosion prevention processes.^{25, 35, 36} Particular regard has been given to the adhesion and corrosion prevention capabilities of chromium (VI) oxoanions.^{25, 37-42}

Chromate containing solutions are often employed as adhesive primers for paints and sealants on plastics and some metals. On plastics, chromate functions as an etchant that produces micro defects in the surface prior to electroplating.³⁷ Chromium(VI) oxoanions are also used in etching, pickling and stripping solutions for metal finishing providing for stronger adhesion of electrodeposits.²⁵

A conversion coating is a thin film formed on a metal surface by converting part of the surface into the coating via electrochemical processes.²⁵ Conversion coatings are usually applied for corrosion resistance, but they also confer increased electrical insulation,

decorative aesthetics, the facility to adsorb lubricants, and provide suitable platform for the application of paint or dye.⁴³ Chromate conversion coatings (CCC) are among the most effective for corrosion/paint adhesion of aluminum, zinc, magnesium, cadmium, and their alloys.²⁵ The composition of CCCs ranges from 100 % Cr^{III} to 100 % Cr^{VI} depending on the pretreatment of the surface and pH of the solution used in the formation of the coating.⁴³ Though CCCs are typically formed under open circuit conditions, applying a potential to the surface also has an impact on the properties and chemical make-up of the coating.^{38, 44, 45}

Equally, the subjects of toxicity and environmental contamination have also received considerable attention. It is now well established that chromate is both a carcinogen and mutagen.^{46, 47} The high solubility of chromate in aqueous media leads to rapid diffusion within the environment.⁴⁸ Although chromates are naturally occurring, the vast majority of sites contaminated with Cr^{VI} compounds are near landfills and industrial waste sites.⁴⁷ Research into the harmful impacts of chromium(VI) oxoanions has triggered efforts to find alternatives to chromium(VI) oxoanions in industrial processes as well as ways to improve industrial waste streams in order to reduce human and environmental exposure.^{35, 49-55}

The hazardous nature of chromate combined with its high mobility in the environment has led to extensive remediation efforts.^{29, 36, 44, 56} Considering the relatively low toxicity of trivalent chromium and the low solubility of the majority of Cr^{III} compounds, most remediation efforts focus on the reduction of Cr^{VI} to Cr^{III}.⁵⁷ Remediation treatment processes can be divided into two broad groups: chemical treatment (CT) and physical treatment (PT). Chemical and physical treatment methods are often combined for the most

effective results. Two of the most common methods are soil washing (SW) a PT and permeable reactive barriers (PRBs) a CT.^{55, 57, 58}

In SW, the soil is removed from the site and cleaned using a high pressure system. After it has been cleaned it is then replaced. While SW is effective for removal of chromate contamination from the larger particles, it does not always effectively remove the contamination from the fine particles, and can require additional treatment.⁵⁷

PRBs are formed by creating a containment barrier that forces the flow of ground water through a “gate” of “zero valent” iron nanoparticles. The particles then reduce the Cr^{VI} to Cr^{III} which is then immobilized.⁵⁵ Although PRBs are less expensive and time consuming than many of the other processes, questions remain concerning the reliability and durability of the barrier-gate.⁵⁹

In spite of its toxic nature, chromate remains the preference in many of the industrial processes listed above due to the difficulty in finding a suitable replacement.^{25, 60-}

⁶³ Understanding the electrochemical reduction of Cr^{VI} to Cr^{III} at a metal surface is vital for the improvement of alternative methods of obtaining the desired surface properties afforded through traditional Cr^{VI} processes as well as the evaluation of new remediation methods.

1.3. Organic Additives Used in Cu Electrodeposition

Electrochemical deposition of metals was first demonstrated in the early 1800's by Brugnatelli, utilizing a voltaic pile supplied by his associate, Allisandro Volta.⁶⁴ Industrial electroplating began to expand around 1840 following the electroplating patents awarded

to George and Henry Elkington, for the electrodeposition of gold and silver utilizing a potassium cyanide electrolytic solution.^{64, 65}

Cu is among the most common metals electrodeposited, and electrodeposition processes are used for plating Cu onto printed circuit boards, electroforming, decorative plating, and electrorefining.⁵ Electrodeposited Cu provides a wide range of mechanical and physical properties which are useful for a wide range of engineering and decorative functions.⁵ Thinly deposited Cu films are also used widely as adhesion layers for zinc and hard chromium finishes.⁵ Over the last 15 years, Cu electrodeposition has also become extremely important in the microelectronics industry.^{66, 67}

Interconnect circuitry, for microelectronic devices, is normally manufactured in one of two ways, “subtractive processing” (SP) or “additive processing” (AP).⁶⁸ SP is accomplished by depositing a continuous layer of metal on a dielectric substrate. A lithographic template is used to transfer the interconnect circuitry pattern to the metal surface. Following the pattern transfer, the unwanted metal is removed by etching it away. Prior to Cu interconnects, SP is the traditional way in which Al interconnects were formed. In standard AP methods, the interconnect circuitry pattern is lithographically transferred to the dielectric. The pattern is then etched into the dielectric material, and metal is then plated into the pattern forming the interconnect circuitry (Figure 1.1). AP methods have traditionally been used for making high-end printed circuit boards.⁶⁸

In the late 1990’s the material of choice for interconnect circuitry changed from Al to Cu. The switch from Al to Cu was driven by three technological advantages provided by Cu.⁶⁹⁻⁷¹ The first is that Al interconnect circuitry was limited by the difficulty in etching features smaller than 100 nm, while depositing Cu in sub 100 nm features was easier. The

second reason for transitioning to Cu is that Cu has a high resistance to electromigration; allowing for smaller circuit dimensions to be attained without sacrificing the lifetime of the device. Third, the lower resistivity of Cu compared to Al allows for shorter resistive-capacitive delay times as well as the ability to produce smaller circuit dimensions without additional heat generation.

Naturally, the initial focus on Cu deposition was thought of in terms of traditional electroless deposition, physical and chemical vapor deposition methods (PVD and CVD respectively) that had been successfully used for Al deposition.⁷²⁻⁷⁷ It was widely accepted that optimum adhesion of Cu to barrier films was accomplished through PVD, but that bulk deposition of Cu by PVD methods often contain voids due to the geometric constraints of the high aspect ratio features.⁶⁸ Similarly, electroless deposition and CVD of Cu produced defects which limited the reliability of the deposit.⁶⁸ In the 1990's, IBM developed a unique AP method which they termed the damascene process, for depositing Cu interconnects.⁶⁹ In the damascene process, a Cu seed layer is deposited onto the wafer, via PVD, to provide electrical conductivity to the surface and a well adhered layer for the foundation of the bulk Cu deposit. Cu is then electroplated onto the surface.⁷⁸ Excess Cu is then removed from the wafer field via chemical mechanical planarization, leaving only filled Cu interconnects.

The transition from Al interconnects to Cu interconnects in the semiconductor industry has led to numerous studies concerning the electrodeposition of Cu and the effects that different bath inorganic and organic molecules (additives) have on the deposit that is formed.⁷⁹⁻⁸⁹ Cu electrodeposition from an additive free acidic solution is expected to produce conformal film growth that has similar defects to those observed in electroless deposition, PVD and CVD methods. The overall function of the additives to the

electroplating bath is to promote complete filling of the damascene features by accelerating Cu deposition at the bottom of the features relative to the wafer field (*i.e.* “*bottom-up filling*” or “*superfilling*”).⁸⁵ Organic additives typically fall into one of three categories: Suppressor (also called Inhibitor), Accelerator (also called Brightener), and Leveler.^{5, 90, 91}

Suppressors are often polyethylene/polypropylene glycol (PEG/PPG) type polymers that range in molecular weight from approximately 1000 to 10,000.^{68, 92} Suppressors, in combination with Cl^- or Br^- , form monolayer films on the copper surface that block interfacial charge transfer during Cu deposition.⁹²⁻⁹⁴ A second property of suppressors is to reduce surface tension, improving the wettability of the surface.⁶⁸

Accelerators typically contain sulfonic acid functionalization and disulfide linkages, such as bis(3-sulfopropyl)-disulfide (SPS). Their purpose is to lower the charge transfer energy for the Cu^{2+} to Cu^+ reduction.^{89, 95, 96} The concentration of the additives is dilute (2 ppm-1000 ppm)⁶⁸ in the plating bath leading to diffusion controlled adsorption to the surface. The smaller molecular weight accelerator diffuses more rapidly into the damascene features than the suppressor.⁶⁸ The accelerator competitively displaces any suppressor molecules on the surface.⁹⁷ Shape-induced concentration field-effects create a wide range of additive fluxes along the different surfaces of the damascene feature (*i.e.* *deep corners < bottom < walls < top corners*).⁶⁹ The rapid diffusion, competitive displacement and gradient in additive concentration along the different surfaces are responsible for the bottom-up fill process.

One of the side effects of the superfilling process is that accelerated growth of the Cu deposit over the damascene feature creates “overfill bumps” (Figure 1.2).⁹⁷ Levelers are used to increase the planarity of the surface prior to CMP by preventing overfilling of

features. Typically, levelers contain amine or aromatic functionality, such as thiourea or Janus Green B respectively.^{90, 95, 98}

The continued exploration of new chemistries for Cu electroplating is driven by the changing exigencies of the microelectronics industry. The ever increasing demand for smaller and faster electronic devices has led to the development of new packaging technology and new interconnections. Similar to the damascene process, Cu has been designated as an optimal material for making other microelectronic interconnects, in particular, through silicon vias (TSVs).⁹⁹⁻¹⁰⁵

In three-dimensional (3D) packaging of microelectronic devices, TSVs display several advantages over traditional two-dimensional (2D) packaging interconnects: 3D devices uses less space than 2D devices, shorter signal delays due to shorter electrical distances, incorporation of assorted technologies in a single package and lower parasitic waste heat/power consumption.^{99, 100} TSVs pass through the silicon semiconductor and connect the front side device to the back of the wafer (Figure 1.3). Currently there are two methods for producing TSVs, blind-via filling (more common) and through-via filling.^{99, 100} Blind-via filling is accomplished in a manner similar to damascene filling discussed earlier with the exception that the feature sizes are much deeper. The resulting copper plug is then exposed by thinning the backside of the wafer (Figure 1.4). Through-via filling is accomplished by first thinning the wafer and depositing a seed layer on the backside of the wafer. The via is then filled and the seed layer is removed (Figure 1.4).

TSV technology presents a whole new set of difficulties that need to be overcome at each stage of the process such as handling thinned wafers⁹⁹ and applying uniform copper seed layers to such high aspect ratio features.¹⁰⁶ Similarly, complete void free

electrochemical filling of TSVs provides new challenges to copper electroplating chemistries due to the very high aspect ratio and overall depth of the features.^{101, 107} The increased depth of the feature leads to problems with mass transport of Cu ions into the via,^{102, 108} wettability of the feature,¹⁰⁸ and increased deposition time.^{109, 110}

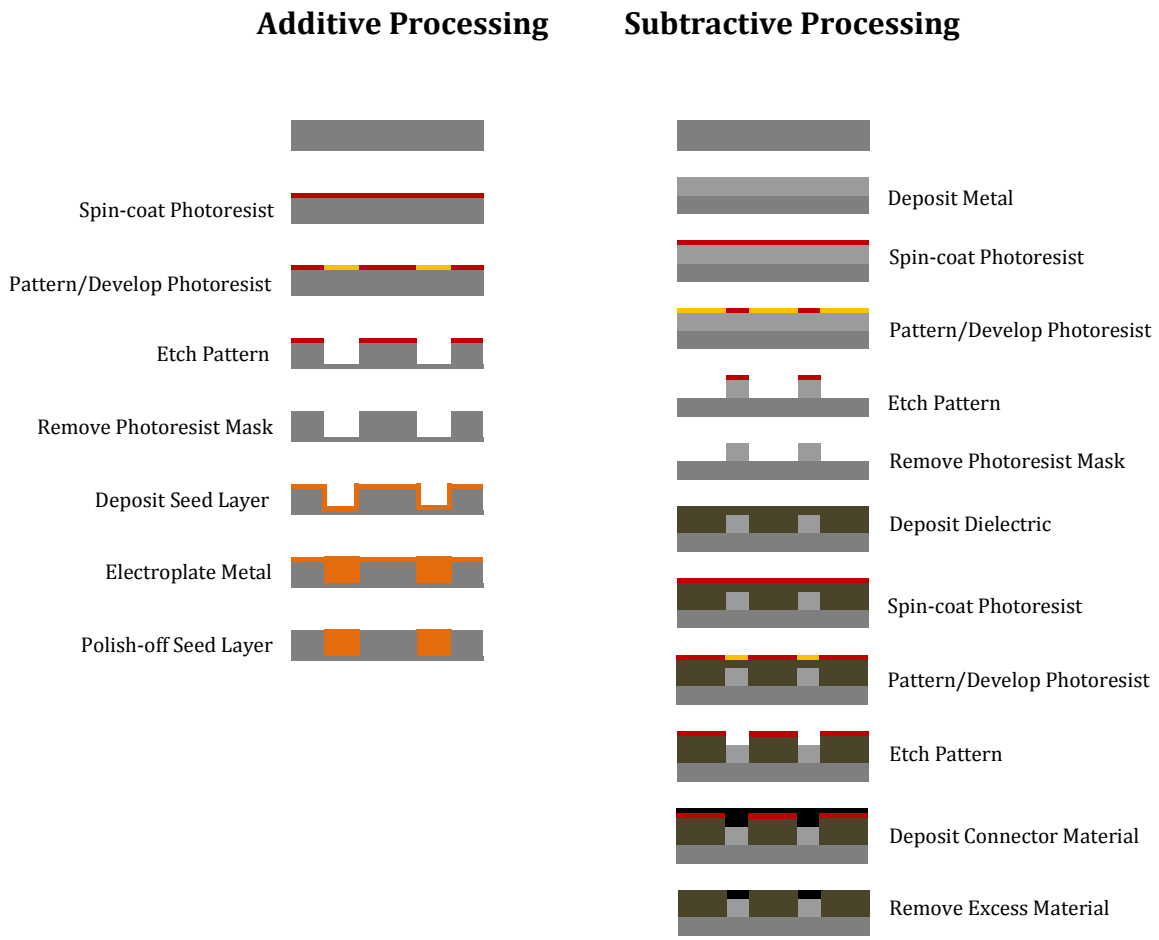


Figure 1.1: Comparison of the subtractive and additive manufacturing processes used to make interconnects.



Figure 1.2: Representation of “over-fill bumps” which are bumps that form over features that undergo superfilling (see reference 12). They are caused when the electroplated material continues to deposit at a higher rate than the wafer field after the feature has been filled completely.

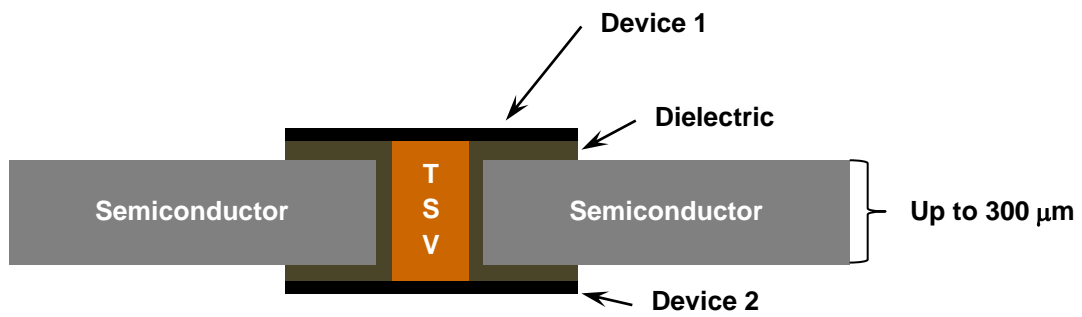


Figure 1.3: Schematic of a through silicon via (TSV). The TSV passes through the entire wafer in order to connect devices on both sides.

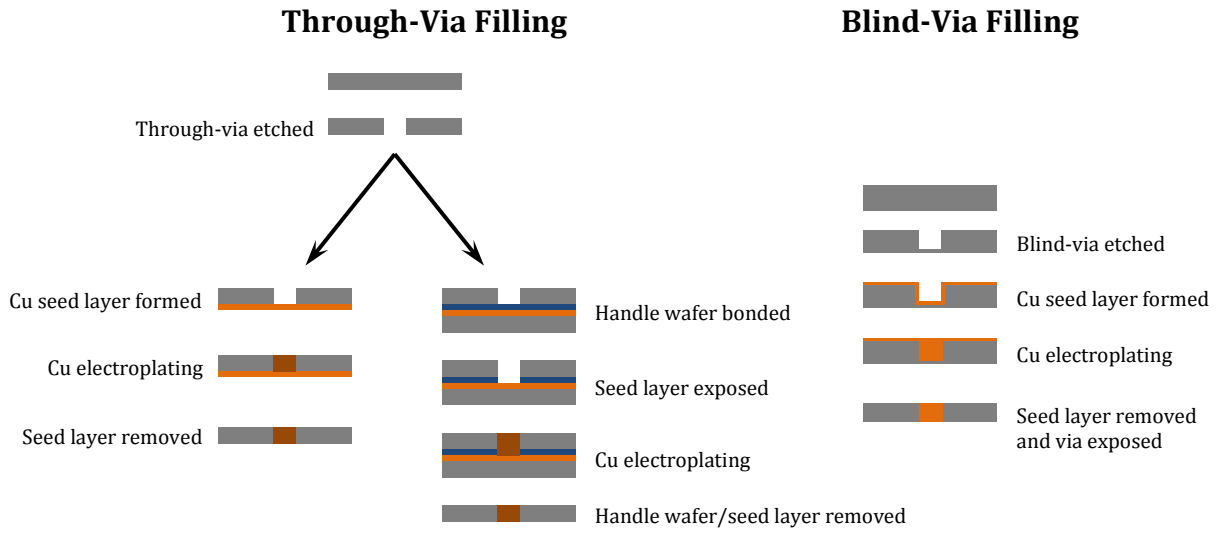


Figure 1.4: Comparison of the two predominant ways to form a through silicon via. Through-via filling is further broken down into two possible approaches for achieving the via.

1.4. References

1. M. C. Li, C. L. Zeng, S. Z. Luo, J. N. Shen, H. C. Lin and C. N. Cao, *Electrochimica Acta*, **48**, (12), 1735-1741, (2003)
2. K. F. Khaled, *Materials Chemistry and Physics*, **125**, (3), 427-433, (2011)
3. K. D. Ralston and N. Birbilis, *Corrosion*, **66**, (7), (2010)
4. A. B. Cezar, I. L. Graff, Y. Rikers, W. H. Schreiner and N. Mattoso, *Electrochemical and Solid State Letters*, **14**, (3), D23-D25, (2011)
5. J. W. Dini, *Modern Electroplating*, Fourth Edition ed, John Wiley & Sons, Inc.: (2000)
6. J. Lee, I. Oh, S. Hwang and J. Kwak, *Langmuir*, **18**, (21), 8025-8032, (2002)
7. A. Watt, *The Electro-Plating and Electro-Refining of Metals*, 2nd ed, C. Lockwood and Son: London, (1911)
8. L. D. Redden and J. N. Greaves, *Hydrometallurgy*, **29**, (1-3), 547-565, (1992)
9. (2007)
10. E. A. Franceschini, G. A. Planes, F. J. Williams, G. J. A. A. Soler-Illia and H. R. Corti, *Journal of Power Sources*, **196**, (4), 1723-1729, (2001)
11. A. A. Gewirth and M. S. Thorum, *Inorganic Chemistry*, **49**, (8), 3557-3566, (2010)
12. Electrodeposit, Electrolysis. *Merriam-Webster Online Dictionary*. 2011. <http://www.merriam-webster.com> (March 3, 2011).
13. A. T. Hubbard, *The Handbook of Surface Imaging and Visualization*, CRC Press: New York, 1995.
14. G. Binnig and H. Rohrer, *Surface Science*, **126**, (1-3), 236-244, (1983)
15. H. J. Guntherodt and R. Wiesendanger, *Scanning Tunneling Microscopy*, 1 ed, Springer-Verlag: New York, 1993, 'Vol.' 1: General Principles and Applications to Clean and Adsorbate-Covered Surfaces.
16. G. Binnig, C. F. Quate and C. Gerber, *Physical Review Letters*, **56**, (9), 930-933, (1986)

17. M. Fleischmann, P. J. Hendra and A. J. McQuillan, *Chemical Physics Letters*, **26**, (2), 163-166, (1974)
18. D. L. Jeanmaire and R. P. Vanduyne, *Journal of Electroanalytical Chemistry*, **84**, (1), 1-20, (1977)
19. M. G. Albrecht and J. A. Creighton, *Journal of the American Chemical Society*, **99**, (15), 5215-5217, (1977)
20. D. A. McQuarrie and J. D. Simon, *Physical Chemistry a Molecular Approach*, University Science Books: Sausalito, (1997)
21. M. Urban, *Vibrational Spectroscopy of Molecules and Macromolecules on Surfaces*, John Wiley & Sons Inc.: New York, (1993)
22. A. Kudelski, *Surface Science*, **603**, (10-12), 1328-1334, (2009)
23. M. Moskovits, in *Surface-Enhanced Raman Scattering: Physics and Applications*. 2006, 'Vol.' 103, pp 1-17.
24. D.-Y. Wu, J. F. Li, B. Ren and Z.-Q. Tian, *Chemical Society Reviews*, **37**, 1025-1041, (2008)
25. D. Pletcher and F. C. Walsh, *Industrial Electrochemistry*, 2nd ed, Chapman and Hall: London, (1990)
26. A. Ahlberg Tidblad and G. Lindbergh, *Electrochimica Acta*, **36**, (10), 1605-1610, (1991)
27. B. Beverskog and I. Puigdomenech, *Corrosion Science*, **39**, (1), 43-57, (1997)
28. V. Brunetti, H. M. Villullas and M. Lopez Teijelo, *Electrochimica Acta*, **44**, (17), 2843-2851, (1999)
29. W. J. Clark, J. D. Ramsey, R. L. McCreery and G. S. Frankel, *Journal of the Electrochemical Society*, **149**, (5), B179-B185, (2002)
30. I. Frenzel, H. Holdik, V. Barmashenko, D. Stamatialis and M. Wessling, *Journal of Applied Electrochemistry*, **36**, (3), 323-332, (2006)
31. M. B. Fritzen, A. J. Souza, T. A. G. Silva, L. Souza, R. A. Nome, H. D. Fiedler and F. Nome, *Journal of Colloid and Interface Science*, **296**, (2), 465-471, (2006)
32. K. S. Henry, J. C. Petura, S. Brooks, S. Denticio, S. A. Kessel and M. Harris, *Canadian Geotechnical Journal*, **44**, 814-839, (2007)

33. M. W. Kendig, A. J. Davenport and H. S. Isaacs, *Corrosion Science*, **34**, (1), 41-49, (1993)
34. S. D. Yim and I.-S. Nam, *Journal of Catalysis*, **221**, (2), 601-611, (2004)
35. D. Golub and Y. Oren, *Journal of Applied Electrochemistry*, **19**, (3), 311-316, (1989)
36. C. M. Welch, O. Nekrassova and R. G. Compton, *Talanta*, **65**, (1), 74-80, (2005)
37. S. Ebnesajjad, *Adhesives Technology Handbook*, 2nd ed, William Andrew Publishing: Nowich, NY, (2009)
38. G. M. Brown, K. Shimizu, K. Kobayashi, G. E. Thompson and G. C. Wood, *Corrosion Science*, **33**, (9), 1371-1385, (1992)
39. W. J. Clark and R. L. McCreery, *Journal of the Electrochemical Society*, **149**, (9), B379-B386, (2002)
40. L. Juffs, A. E. Hughes, S. Furman and P. J. K. Paterson, *Corrosion Science*, **44**, (8), 1755-1781, (2002)
41. W. R. McGovern, P. Schmutz, R. G. Buchheit and R. L. McCreery, *Journal of the Electrochemical Society*, **147**, (12), 4494-4501, (2000)
42. L. Xia and R. L. McCreery, *Journal of the Electrochemical Society*, **145**, (9), 3083-3089, (1998)
43. J. R. Davis, *Corrosion of Aluminum and Aluminum Alloys*, ASM International: Materials Park, OH, 1999.
44. J. D. Ramsey and R. L. McCreery, *Journal of the Electrochemical Society*, **146**, (11), 4076-4081, (1999)
45. J. D. Ramsey, L. Xia, M. W. Kendig and R. L. McCreery, *Corrosion Science*, **43**, (8), 1557-1572, (2001)
46. E. Gaggelli, F. Berti, N. D'Amelio, N. Gaggelli, G. Valensin, L. Bovalini, A. Paffetti and L. Trabalzini, *Environmental Health Perspectives*, **110**, 733-738, (2002)
47. T. J. O'Brien, S. Ceryak and S. R. Patierno, *Mutation Research/Fundamental and Molecular Mechanisms of Mutagenesis*, **533**, (1-2), 3-36, (2003)
48. C. Gong and R. J. Donahoe, *Applied Geochemistry*, **12**, (3), 243-254, (1997)
49. J. Fang, Z. Gu, D. Gang, C. Liu, E. S. Ilton and B. Deng, *Environ. Sci. Technol.*, (2007)

50. G. E. Fryxell, J. Liu, T. A. Hauser, Z. Nie, K. F. Ferris, S. Mattigod, M. Gong and R. T. Hallen, *Chem. Mater.*, **11**, (8), 2148-2154, (1999)
51. M. Ginder-Vogel, T. Borch, M. A. Mayes, P. M. Jardine and S. Fendorf, *Environmental Science & Technology*, **39**, (20), 7833-7839, (2005)
52. S. R. Qiu, H. F. Lai, M. J. Roberson, M. L. Hunt, C. Amrhein, L. C. Giancarlo, G. W. Flynn and J. A. Yarmoff, *Langmuir*, **16**, (5), 2230-2236, (2000)
53. F. J. Rodriguez, S. Gutierrez, J. G. Ibanez, J. L. Bravo and N. Batina, *Environ. Sci. Technol.*, **34**, (10), 2018-2023, (2000)
54. F. Rodriguez-Valadez, C. Ortiz-Exiga, J. G. Ibanez, A. Alatorre-Ordaz and S. Gutierrez-Granados, *Environ. Sci. Technol.*, **39**, (6), 1875-1879, (2005)
55. R. T. Wilkin, C. M. Su, R. G. Ford and C. J. Paul, *Environmental Science & Technology*, **39**, (12), 4599-4605, (2005)
56. B. L. Hurley and R. L. McCreery, *Journal of the Electrochemical Society*, **150**, (8), B367-B373, (2003)
57. R. Bewley, *CL:AIRE Technical Bulletin*, **TB14**, 1-4, (2007)
58. B. A. Manning, J. R. Kiser, H. Kwon and S. R. Kanel, *Environmental Science & Technology*, **41**, (2), 586-592, (2007)
59. J. T. Nurmi, P. G. Tratnyek, V. Sarathy, D. R. Baer, J. E. Amonette, K. Pecher, C. Wang, J. C. Linehan, D. W. Matson, R. L. Penn and M. D. Driessen, *Environmental Science & Technology*, **39**, (5), 1221-1230, (2005)
60. M. Trueba and S. Trasatti, *Advanced Materials Research*, **38**, 14-26, (2008)
61. R. L. Twite and G. P. Bierwagen, *Progress in Organic Coatings*, **33**, (2), 91-100, (1998)
62. G. P. Bierwagen, D. Battocchi, A. Simões, A. Stammess and D. E. Tallman, *Progress in Organic Coatings*, **59**, (3), 172-178, (2007)
63. F. Berger, J. Delhalle and Z. Mekalif, *Electrochimica Acta*, **53**, (6), 2852-2861, (2008)
64. M. Schlesinger, *Electroplating*, John Wiley & Sons, Inc.: (2000)
65. G. Elkington and H. Elkington, B. P. Office, 8447, (1840).
66. C. L. Beaudry and J. O. Dukovic, *Interface*, **13**, (4), 40-44, (2004)
67. T. Ritzdorf, *ECS Transactions*, **6**, (8), 1-11, (2007)

68. J. Reid, in *Handbook of Semiconductor Manufacturing Technology*. Second ed., CRC Press: 2007, pp 16-1 – 16-47.
69. P. C. Andricacos, C. Uzoh, J. O. Dukovic, J. Horkans and H. Deligianni, *Ibm Journal of Research and Development*, **42**, (5), 567-574, (1998)
70. D. C. Edelstein, G. A. Saihalasz and Y. J. Mii, *Ibm Journal of Research and Development*, **39**, (4), 383-401, (1995)
71. D. C. Edelstein, J. Heidenreich, R. Goldblatt, W. Cote, C. Uzoh, N. Lustig, P. Roper, T. McDevitt, W. Motsiff, A. Simon, J. O. Dukovic, R. Wachnik, H. Rathore, R. Shultz, L. Su, S. Luce and J. Slattery, Technical Digest, IEE International Electron Devices Meeting. 773-776. 1997
72. N. Misawa, S. Kishii, T. Ohba, Y. Arimoto, Y. Furumura and H. Tsutikawa, VMIC Conference. 353-358. 1993
73. T. Q. Nguyen, Electrochemical Society Proceedings, ECS Meeting. 120. 1997
74. T. Q. Nguyen, L. J. Charneski and D. R. Evans, *Journal of The Electrochemical Society*, **144**, (10), 3634-3639, (1997)
75. Y. Shacham-Diamand and S. Lopatin, *Electrochimica Acta*, **44**, (21-22), 3639-3649, (1999)
76. Y. Shacham-Diamand and S. Lopatin, *Journal of Microelectronic Engineering*, **37**, 77, (1997)
77. Y. Shacham-Diamand and V. M. Dubin, *Journal of Mircroelectronic Engineering*, **33**, 47-58, (1997)
78. P. C. Andricacos, *Electrochemical Society Interface*, **8**, (1), 32, (1999)
79. W.-P. Dow, C.-C. Li, M.-W. Lin, G.-W. Su and C.-C. Huang, *Journal of The Electrochemical Society*, **156**, (8), D314-D320, (2009)
80. W.-P. Dow, C.-C. Li, Y.-C. Su, S.-P. Shen, C.-C. Huang, C. Lee, B. Hsu and S. Hsu, *Electrochimica Acta*, **54**, (24), 5894-5901, (2009)
81. W.-P. Dow and C.-W. Liu, *Journal of The Electrochemical Society*, **153**, (3), C190-C194, (2006)
82. W.-P. Dow, M.-Y. Yen, S.-Z. Liao, Y.-D. Chiu and H.-C. Huang, *Electrochimica Acta*, **53**, (28), 8228-8237, (2008)

83. W.-P. Dow, M.-Y. Yen, C.-W. Liu and C.-C. Huang, *Electrochimica Acta*, **53**, (10), 3610-3619, (2008)
84. J. J. Kelly, C. Tian and A. C. West, *Journal of The Electrochemical Society*, **146**, (7), 2540-2545, (1999)
85. T. P. Moffat, D. Wheeler, S. K. Kim and D. Josell, *Journal of The Electrochemical Society*, **153**, (2), C127-C132, (2006)
86. M. J. Willey and A. C. West, *Journal of The Electrochemical Society*, **154**, (3), D156-D162, (2007)
87. M. Tan and J. N. Harb, *Journal of The Electrochemical Society*, **150**, (6), C420-C425, (2003)
88. R. Akolkar and U. Landau, *Journal of The Electrochemical Society*, **156**, (9), D351-D359, (2009)
89. T. P. Moffat, B. Baker, D. Wheeler and D. Josell, *Electrochemical and Solid State Letters*, **6**, (4), C59-C62, (2003)
90. B. Bozzini, C. Mele, L. D'Urzo and V. Romanello, *Journal of Applied Electrochemistry*, **36**, (9), 973-981, (2006)
91. B. Bozzini, C. Mele, L. D'Urzo, V. Romanello and G. Giovannelli, *Transactions of the Institute of Metal Finishing*, **84**, (4), 177-187, (2006)
92. J. P. Healy, D. Pletcher and M. Godelough, *Journal of Electroanalytical Chemistry*, **338**, 155-165, (1992)
93. K. S. Herbert, S. Adhikari and E. Houser, *Journal of The Electrochemical Society*, **152**, C324, (2005)
94. V. D. Jovic and B. M. Jovic, *Journal of the Serbian Chemical Society*, **66**, 935, (2001)
95. E. E. Farndon, F. C. Walsh and S. A. Campbell, *Journal of Applied Electrochemistry*, **25**, 574, (1995)
96. N. Zhukauskaite and A. Malinauskas, *Protection of Metals*, **25**, 132, (1989)
97. T. P. Moffat, J. E. Bonevich, W. H. Huber, A. Stanishevsky, D. R. Kelly, G. R. Stafford and D. Josell, *Journal of The Electrochemical Society*, **147**, (12), 4524-4535, (2000)
98. Y.-B. Li, W. Wang and Y.-L. Li, *Journal of The Electrochemical Society*, **156**, (4), D119-D124, (2009)

99. S. Q. Gu, U. Ray, Y. Li, A. Chandrasekaran, B. Henderson and M. Nowak, Interconnect Technology Conference (IITC), 2010 International. 1-3. 2010
100. B. Kim, C. Sharbono, T. Ritzdorf and D. Schmauch, 56th Electronic Components and Technology Conference. 838-843. 2006
101. E. Delbos, L. Omnès and A. Etcheberry, *Microelectronic Engineering*, **87**, (3), 514-516, (2010)
102. P. Dixit and J. Miao, *Journal of The Electrochemical Society*, **153**, (6), G552-G559, (2006)
103. M. Facchini, T. Carlson, A. Vignon, M. Palkovic, F. Catthoor, W. Dehaene, L. Benini and P. Marchal, Design, Automation & Test in Europe Conference & Exhibition. 923-928. 2009
104. J. U. Knickerbocker, P. S. Andry, L. P. Buchwalter, A. Deutsch, R. R. Horton, K. A. Jenkins, Y. H. Kwark, G. McVicker, C. S. Patel, R. J. Polastre, C. D. Schuster, A. Sharma, S. M. Sri-Jayantha, C. W. Surovic, C. K. Tsang, B. C. Webb, S. L. Wright, S. R. McKnight, E. J. Sprogis and B. Dang, *Ibm Journal of Research and Development*, **49**, (4.5), 725-753, (2005)
105. O. Lühn, C. Van Hoof, W. Ruythooren and J. P. Celis, *Electrochimica Acta*, **54**, (9), 2504-2508, (2009)
106. O. Lühn, C. Van Hoof, W. Ruythooren and J. P. Celis, *Microelectronic Engineering*, **85**, (10), 1947-1951, (2008)
107. C. Fang, A. Le Corre and D. Yon, *Microelectronic Engineering*, **88**, (5), 749-753, (2011)
108. P. Dixit, X. Chen, J. Miao, S. Divakaran and R. Preisser, *Applied Surface Science*, **253**, (21), 8637-8646, (2007)
109. K. Kondo, T. Yonezawa, D. Mikami, T. Okubo, Y. Taguchi, K. Takahashi and D. P. Barkey, *Journal of The Electrochemical Society*, **152**, (11), H173-H177, (2005)
110. O. Lühn, J. P. Celis, C. Van Hoof, K. Baert and W. Ruythooren, ECS Transactions. 123-133. 2007

Chapter 2. Experimental

2.1. General Procedures

2.1.1. Cleaning Procedure

All Glass, Teflon, and Kel-F materials (glassware) were cleaned prior to use. The cleaning procedure involves a two-step process. Following a quick rinse with DI water the glassware and other items were placed in a Nochromix (Godax Laboratories)/concentrated H_2SO_4 acid bath for 8 to 12 hours. Upon removal the glassware was rinsed with DI water to remove excess acid. Second, the glassware was placed into a 6 N nitric acid bath for a minimum of 6 hours. The glassware was then removed from the nitric acid bath and rinsed with deionized (DI) water to remove excess nitric acid. After rinsing with DI water, the glassware was then rinsed with boiling ultra-pure water (Millipore Inc., 18 $\text{M}\Omega/\text{cm}$) and left to dry.

Two additional cleaning methods were used in addition to the one mentioned previously. Rubber O-rings, gold coated AFM clips, and Cu wire pseudo reference electrodes were soaked in 50 % H_2SO_4 and then rinsed with DI and boiling ultra-pure water as described previously. AFM clips and wires were only allowed to soak for 10 to 15 min., and O-rings were allowed to soak overnight. Piranha cleaning solution (70% H_2SO_4 + 30% H_2O_2) was used to clean noble metal electrodes prior to use in STM experiments. The piranha cleaning solution was made directly before use, and parts were

allowed to soak for 1 to 2 hrs. Immediately following the soak, the parts were rinsed with DI and ultra-pure water in the manner described previously.

2.1.2. Solution Preparation

Solutions used in the chromate deposition study were prepared from ultra-pure water (Milli-Q UVplus, Millipore Inc.; 18.2 M Ω /cm). Reagent grade Na₂CrO₄ (Baker, 99.1%), KCl (Aldrich, 99.999%), and HCl (Baker, UltrexII) were used for preparing solutions. Cyclic voltammetric measurements, STM, and AFM experiments were carried out using flame annealed Au-on-glass substrates (Arrandee) as the working electrode; where flame annealing forms a quasi (111) textured surface.

Solutions used in the Cu leveler experiments were prepared from ultra-pure water (Milli-Q Reference, Millipore Inc.; 18.2 M Ω /cm) and high purity H₂SO₄ (Optima, Fisher Scientific). Dodecyltrimethyl ammonium bromide (DTAB)(>98%), thonzonium bromide (ThonB)(>98%) and benzyldimethylhexadecyl ammonium chloride (BDAC)(>98%) were obtained from Sigma-Aldrich and were used throughout the study. In addition to the quaternary ammonium salts, CuSO₄ (99.999% Sigma-Aldrich) was also added to the plating solutions. Two different pH regions were studied, pH = 1 and pH = 3.3. In the case of the pH 3.5 solutions, a neutral solution was carefully adjusted by adding a calculated amount of 0.1 M H₂SO₄. The pH was then determined using an *UltraBasic* UB-5 pH meter (Denver Instruments) and the final adjustment of pH was made by adding either acid or base dropwise to the solution as appropriate.

2.2. Surface Preparation

2.2.1. Mechanical Polishing Procedure

Single and polycrystalline working electrodes, 10-12.5 mm in diameter and 2-3 mm thick, were purchased from Monocrystals Inc. Prior to each experiment, the working electrode was mechanically polished to a mirror finish according to the following procedure:

- The crystalline disk was attached (using double sided scotch tape acquired from 3M) to a stainless steel polishing dye in order to maintain an even surface, and in the case of single crystals, to maintain the crystallographic plane of the surface.
- A small amount of diamond polishing suspension (Buehler) was added to the polishing pad along with ultra-pure water.
- Polishing was then performed either by hand in a figure eight pattern or on a polishing wheel depending on the metal being polished.
- The crystal was then rinsed with ultra-pure water, and an optical microscope was used to verify the surface before continuing to the next polishing grit.
- Following each polishing step, the crystal was removed from the polishing dye, rinsed with ultra-pure water, sonicated for 1-2 minutes, and then rinsed with ultra-pure water again in order to remove leftover polishing grit. This step was repeated 3 times before moving onto the next polishing step. Note that over polishing the crystal may result in the formation of pits in the surface during sonication.

The initial polishing grit was usually 9 μm , although, 800 grit sandpaper was used as the starting point for crystals that had large defects or scratches. The final polishing step was always completed on the day of the experiment and as close to the start of the experiment as was possible in order to minimize surface contamination. For electrochemical and Raman experiments, the surface was typically polished to 0.25 μm , and polished to 0.05 μm for probe microscopy experiments. Following the final step, the working electrode was transported under ultra-pure water in order to prevent atmospheric contamination of the surface.

2.2.2. Gold on Glass Preparation

11 mm \times 11 mm Gold-on-glass samples that were used for EC-STM and EC-AFM experiments were acquired from Arrandee. The surface was prepared for use by annealing it with a H_2 flame for ~ 10 min. according to literature.¹¹ The flaming procedure consisted of heating the entire surface evenly for the first 5 min. and then focusing on the center of the surface. The sample would glow at a deep red color. If the color increased passed orange, the surface would warp and the sample was no longer usable. Either a torch or a pipet can be used for the flaming procedure. It is harder to control a torch than a pipet for this procedure. It should be noted that a pipet emits a yellow/orange flame that makes it difficult to see the gold surface, leading to overheating of the surface.

2.2.3. Surface Roughening

Both Cu(poly) and Au(poly) surfaces were roughened prior to surface enhanced Raman experiments. Both types of surfaces were roughened utilizing oxidation/reduction

cycles in 0.1 M KCl. The roughening cycles were based on methods reported by Tian *et al.*²

The procedure for roughening is outlined as follows:

- The crystal was attached to the end of a metal plunger via vacuum and subsequently placed in contact with the roughening solution in a hanging drop configuration.
- Au(poly) disks were electrochemically roughened by cycling the potential between -0.26 V and 1.24 V vs. Ag/AgCl, in a 0.1 M KCl solution for 10 minutes. The macro that was developed for the roughening procedure is included in Appendix A.
- Cu(poly) disks were electrochemically roughened by cycling between -400 mV and 400 mV vs. Ag/AgCl in a solution of 0.1 M KCl. The macro developed for this roughening procedure is located in Appendix A.
- The final step in the electrochemical roughening procedure holds the potential of the surface sufficiently negative of the potential of zero charge (pzc) to cause desorption of Cl^- from the surface.
- The working electrode was then immediately rinsed with copious amounts of ultra-pure water in order to remove as much Cl^- as possible.

2.3. Electrochemical Experiments

2.3.1. General

Electrochemical measurements were performed in a three electrode cell using a CHI 760C or CHI 760D potentiostat (CH Instruments). Solutions were purged with Ar before use for approximately 1 h and an Ar atmosphere was maintained in the cell during

all electrochemical measurements. A Ag/AgCl reference electrode was utilized for most experiments, and all potentials reported are referenced to Ag/AgCl.

Counter electrodes were made of Au, Pt, or graphite. Au and Pt counter electrodes were prepared by first rinsing with ultra-pure water and then holding them in a H₂ flame to remove impurities. Graphite counter electrodes were prepared by immersing the electrode in the solution to be used for ~10 min. and then rinsing with copious amounts of boiling ultra-pure water.

All working electrodes were prepared as described previously. In the chromate study a Au(111) or Au(poly) disk obtained from Monocrystals Inc. was utilized. The Cu leveler study used a 1.25 cm diameter Cu (poly) disk (Monocrystals Inc.) for cyclic voltammetry and impedance vs. potential experiments, and a 1.0 cm diameter Cu (poly) disk (Monocrystals Inc.) was for all other electrochemical experiments. Working electrodes were maintained in the hanging drop configuration throughout the course of each experiment.

2.3.2. Cyclic Voltammetry

Cyclic voltammetry (CV) was performed in a two-compartment, glass/glass-Teflon electrochemical cell, described previously, or in a one compartment glass cell shown in Figure 2.1. The reference electrode was connected to the electrochemical cell via a capillary salt bridge. The counter electrode for the one-compartment cell was located in a sidearm of the cell and separated with a porous glass frit.

2.3.3. Rotating Disk Electrode (RDE) Experiments

RDE measurements were obtained using a Pine Model MSR Speed Control rotator. A custom Kel-F collet, shown in Figure 2.2 (Appendix B), was designed to mate with the xxx shaft of the rotator. In addition to the custom collet, an addition funnel (Figure 2.3) was modified to attach to the top of the electrochemical cell for the purpose of degassing solutions that would foam excessively.

2.3.4. Differential Capacitance Measurements

Differential capacitance measurements were obtained using impedance vs. potential experiments. The excitation frequency was set to $f = 10$ Hz and the amplitude was set to 5 mV. The impedance is related to capacitance through Eqn. 2.1.³

$$C = \frac{1}{\omega \cdot R \cdot \tan\theta} \quad (2.1)$$

$$\omega = 2\pi f \quad (2.2)$$

where R is the measured impedance in ohms and θ is the phase change between the real and imaginary components of the impedance.

2.4. Electrochemical Scanning Tunneling Microscopy (EC-STM)

EC-STM measurements were carried out using a Nanoscope III E electrochemical scanning tunneling microscope (Digital Instruments). Substrates were held in position on the EC-STM base using an Invar mount and Kel-F fluid cell with Teflon O-ring designed by

our lab (pictured in Appendix C). The fluid cell was modified such that a Ag/AgCl no-leak reference electrode (Cypress) could be used during experiments; a gold wire was also used as a reference electrode. EC-STM imaging was carried out with the surface of the sample acting as the working electrode.

EC-STM tips were prepared by electrochemical etching of a tungsten wire (0.25 mm in diameter) in 2.0 M KOH, followed by insulation with Apiezon Wax W in order to reduce the area in contact with the electrolyte. Insulating the tip in this manner aids in minimizing Faradaic current noise. Tips were placed in the scanning head at least 1 hour prior to use to reduce the amount of thermal drift during imaging. During imaging, tip potentials were maintained in electrochemically stable potential regions, determined by cyclic voltammetry, in order to minimize Faradaic reactions at the tip. As a result, the tip/sample bias was largely controlled by the surface potential. EC-STM images were recorded in constant height mode, unless otherwise indicated, and were analyzed utilizing WSxM software version 4.0 (Nanotec).⁴

Samples that were too small for the fluid cell were potted using Scotchcast Electrical Resin (3M). The sample was mounted to a thin steel disk with silver print (GC Electronics). After the silver print was dry, a small amount of super glue was added to the base of the sample as a sealant. The mounted sample was then placed in a Teflon mold (Figure 2.4). The Scotchcast resin was mixed per the company's instructions and added to the mold via extrusion through a syringe needle (to remove air bubbles), completely covering the sample. The resin was then allowed to cure overnight before removing the sample from the mold. Excess resin covering the sample was removed by mechanical polishing as described in section 2.2.1.

2.5. Electrochemical Atomic Force Microscopy (EC-AFM)

AFM measurements were carried out in contact mode with a PicoSPM 300 type afm300s scanner (Molecular Imaging, currently Agilent Technologies) which was controlled with a Nanoscope III E controller (Digital Instruments, currently Veeco). Silicon nitride contact mode AFM tips were acquired from Agilent Technologies. Tips were prepared for experiments by rinsing with ethanol followed by ultra-pure water and finally irradiated with UV light for ~10 min. Calibration was conducted using freshly cleaved mica as described in the Veeco NanoScope Command Reference Manual (version 5.12 revision B); the spacing of Au(111) atoms was also used as an internal standard. Raw data files were exported from the Nanoscope E version 4.23 software (Digital Instruments) and analyzed using WSxM version 4.0 (Nanotec Electronica) ⁴. Typical scan rates for lattice resolved imaging were 8-12 Hz; longer range imaging was performed at slower scan rates, 2 Hz.

In-situ EC-AFM experiments were performed using a custom Teflon fluid cell (Figure 2.5). The cell was pressed against the working electrode forming a seal. Contact was made with gold-on-glass substrates through a pogo-pin that passed through the cell. The potential was controlled by a CV-27 (BAS). Both the reference and counter electrodes were Pt wire. The Pt quasi reference electrode potential was converted to the Ag/AgCl scale.

2.6. Raman Spectroscopy

Raman spectroscopy experiments were performed using a custom instrumental set-up (Figure 2.6). Illumination of the sample was carried out by focusing one of three light

sources on the sample. The possible light sources were a HeNe laser at 632.8 nm (Meredith Instruments), a 532 nm diode laser (B&W Tek Inc.), or a 671 nm diode laser (CrystaLaser LC). The laser beam passed through a notch filter to remove stray wavelengths from the source. Following the rest of the beam's path, it was focused onto the sample at a 45° angle of incidence. The light scattered from the sample was collected using a camera lens (Cannon 85 mm lens) and then focused onto the slit with a second lens. An edge filter was placed 1.5 inches in front of the slit in order to remove the intense Rayleigh line. A SpectraPro 2300i double monochromator (SpectraPro) with a 1200 grooves/mm grating was used to disperse the Raman scattered light onto a charge coupled detector (CCD) (Andor) which was cooled to -80 °C using a Neslab RTE 10 Refrigerated Bath (Thermo Electron Corporation).

Calibration was accomplished using a Ne spectral calibration lamp. In order to avoid damage to the CCD, the slit was closed to 0.1 μm, the acquisition time was reduced to the shortest time allowable in the software (0.0001 s), and a neutral-density filter was placed in front of the slit. Following acquisition of the calibration spectrum, the peaks were assigned and the units were changed from wavelength to wavenumber.

2.6.1. Normal Raman Spectroscopy

Two methods were utilized to collect Raman spectra from powder samples. The first method was performed by attaching a piece of double-sided tape to a glass slide and adding the powder to the tape. The second method was employed specifically for hazardous materials or ones that did not adhere to the tape well. Samples were instead contained between two glass slides. The two glass slides were cleaned with piranha solution for ~30 min. and an O-ring was cleaned in 50 % H₂SO₄ as described previously.

Following the cleaning step, the O-ring was placed on one of the slides creating a “well.” The well was then filled with the sample, and the other slide was placed on top of the well enclosing the sample (Figure 2.7). The container was held together with electrical tape.

Spectra of solution/liquid samples were collected using a 1 cm × 1 cm quartz cuvette. The cuvette was cleaned and prepared according to the general cleaning procedures explained previously for glassware.

2.6.2. *In-situ Surface Enhanced Raman Spectroscopy (SERS)*

SERS experiments were performed at room temperature in a spectroelectrochemical cell described previously⁵⁵ and shown below in Figure 2.8. The Ag/AgCl reference electrode was attached to the cell via a capillary salt bridge. The counter electrode, either Au or Pt, was prepared in the same manner as described in section 2.3.1. The counter electrode was then fitted into the cell via a Teflon fitting. The working electrode was held in place on the end of the plunger with Teflon tape.

The working electrode was mechanically polished and then electrochemically roughened as described in section 2.2.3. Following the roughening step, the appearance of both the Cu(poly) and Au(poly) surfaces were dull reddish brown. Note the Au(poly) surface displayed the best enhancements when the surface had a green sheen in addition to the reddish color described above. A gold wire coiled into a spring was pressed against the back of the working electrode in order to achieve electrical contact.

A second method for producing enhancement of the Raman signal is accomplished by utilizing shell isolated nanoparticle enhanced Raman spectroscopy (SHINERS).⁶ SHINERS were provided by Stefano Boulos of the C. Murphy research group at the University of Illinois at Urbana-Champaign. An aqueous suspension of SHINERS particles

was applied to the surface using a clean pipet; the solvent was then allowed to evaporate under a stream of N₂. When the surface is dry, the working electrode is ready for use.

Data acquisition times ranged from 30 s to 5 min. depending on the intensity of the spectral peaks. In order to find areas of the crystal that demonstrated the highest intensity enhancement effects, open circuit potential spectra were obtained for several spots. Two different methods were utilized to obtain *in-situ* potential control during the collection of spectra. The first method, using a CV-27 potentiostat (BAS), was to step the potential in 50 mV increments and hold the potential while the spectrum was acquired. The second method was to collect spectra while the potential was actively swept. This was accomplished by choosing a sufficiently slow sweep rate, so that each spectrum was acquired over a small potential window, on the order of 10 to 50 mV.

2.7. Spartan Calculations

Optimal geometries of the levelers were constructed by using the Spartan 08 program⁷⁷ using the ab initio Hartree–Fock method and a 3-21G* basis set. After energy minimization, the Spartan program was utilized to find the normal vibrational modes and frequencies associated with each leveler.⁸

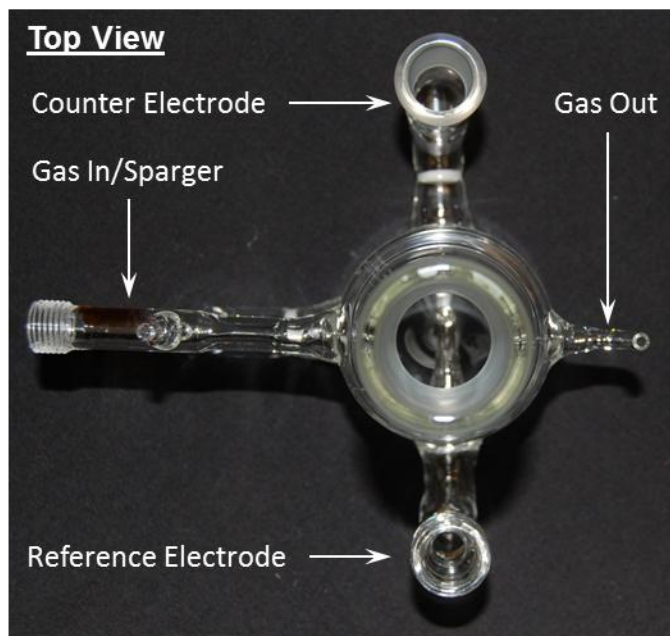


Figure 2.1: One compartment glass Electrochemical cell. A valve is used to direct gas flow for sparging solution or for maintaining atmosphere. The counter electrode is separated via medium glass frit and a Luggin-Haber capillary connects the main cell to the reference electrode.

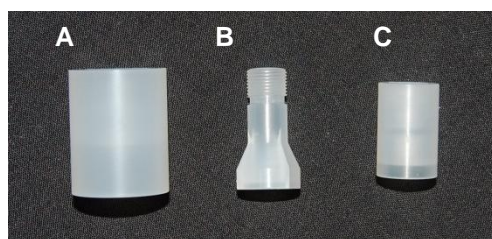


Figure 2.2: An illustration of the Kel-F collet assembly used for rotating experiments of loose single and polycrystalline working electrode disks. A) Barrel of the collet. B) Collet plunger. C) Rotating shaft adapter.

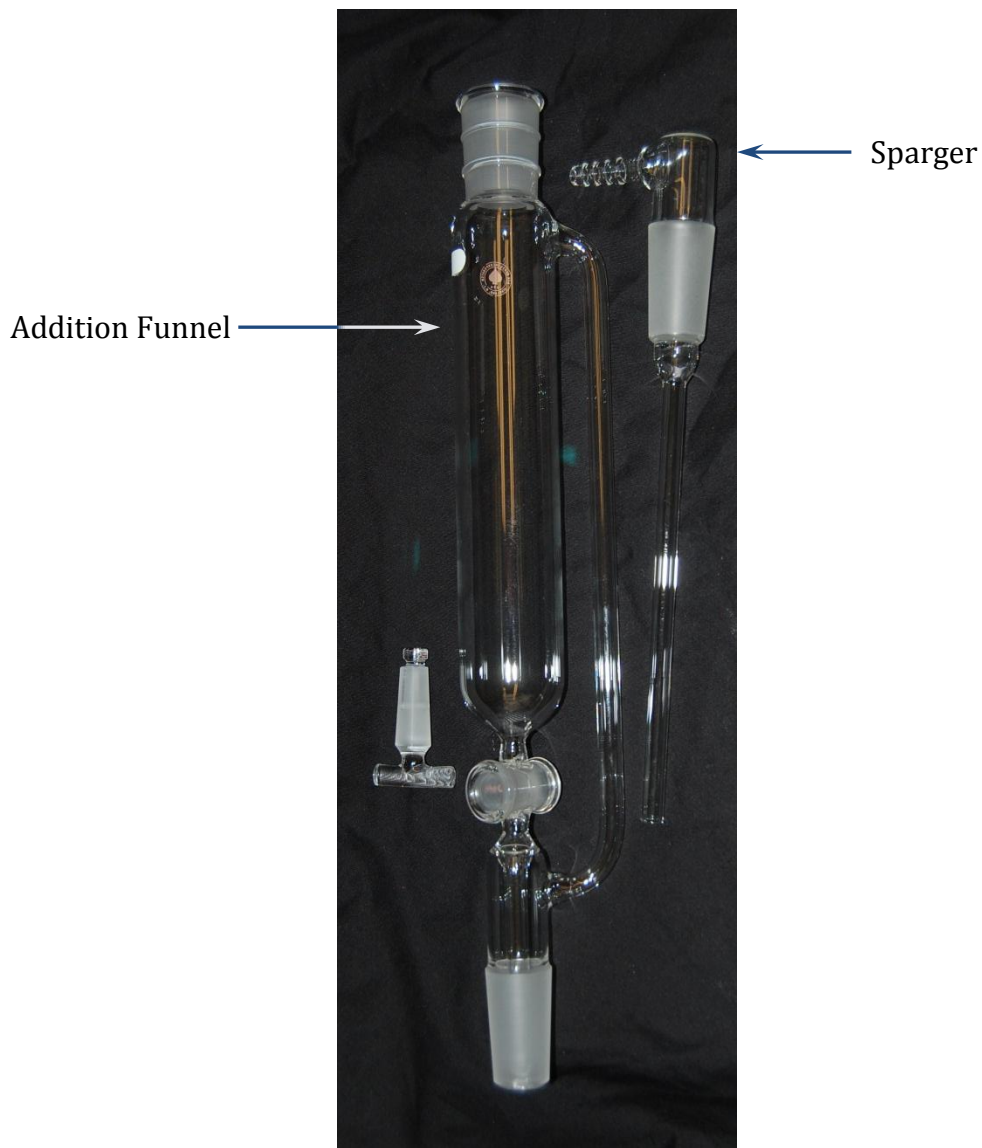


Figure 2.3: The addition funnel is added to the 24/40 joint of the electrochemical cell (see Figure 2.1) and filled with the solution to be purged. The sparger is then fitted to the top of the funnel. As gas bubbles through the solution, the same atmosphere is maintained in the electrochemical cell. This allows transfer of solution without exposure to unwanted atmospheric conditions.

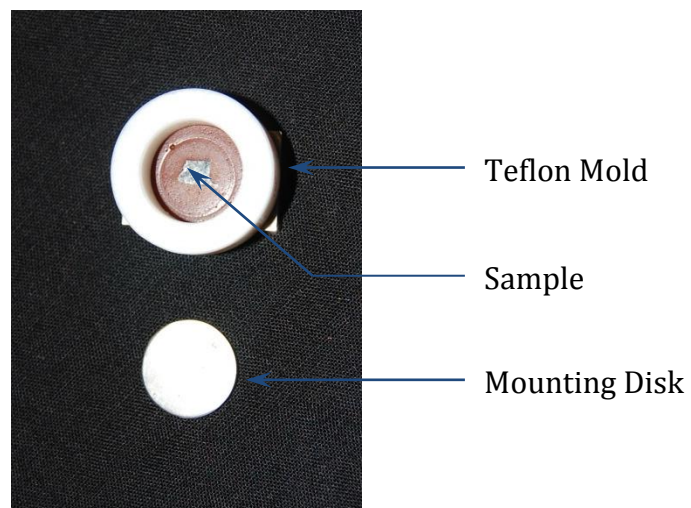


Figure 2.4: Teflon mold and mounting disk used for potting irregularly shaped or small samples for use in EC-STM or EC-AFM experiments.

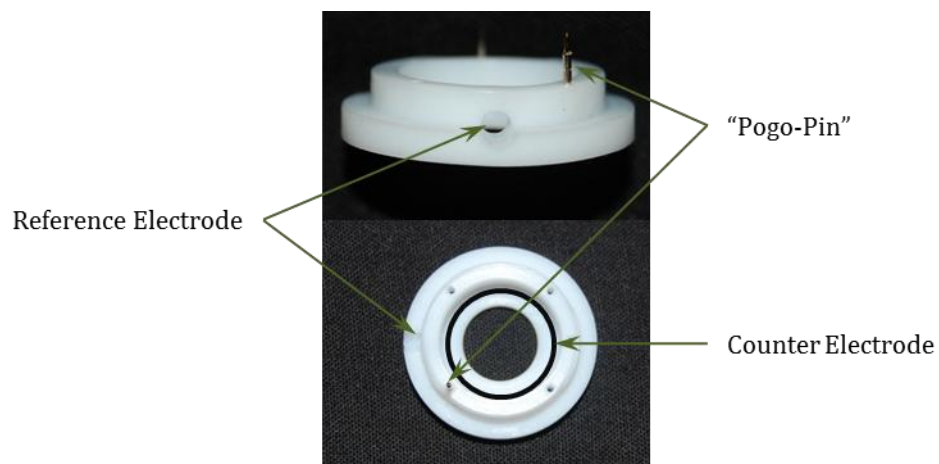


Figure 2.5: The “pogo-pin” is used to make electrical contact with samples that are only conductive on the surface. The reference electrode hole is designed to take the smallest diameter “no-leak” Ag/AgCl reference electrode from Cypress (2 mm diameter). The counter electrode wire wraps around the inside edge of the cell and is held in place by the reference electrode.

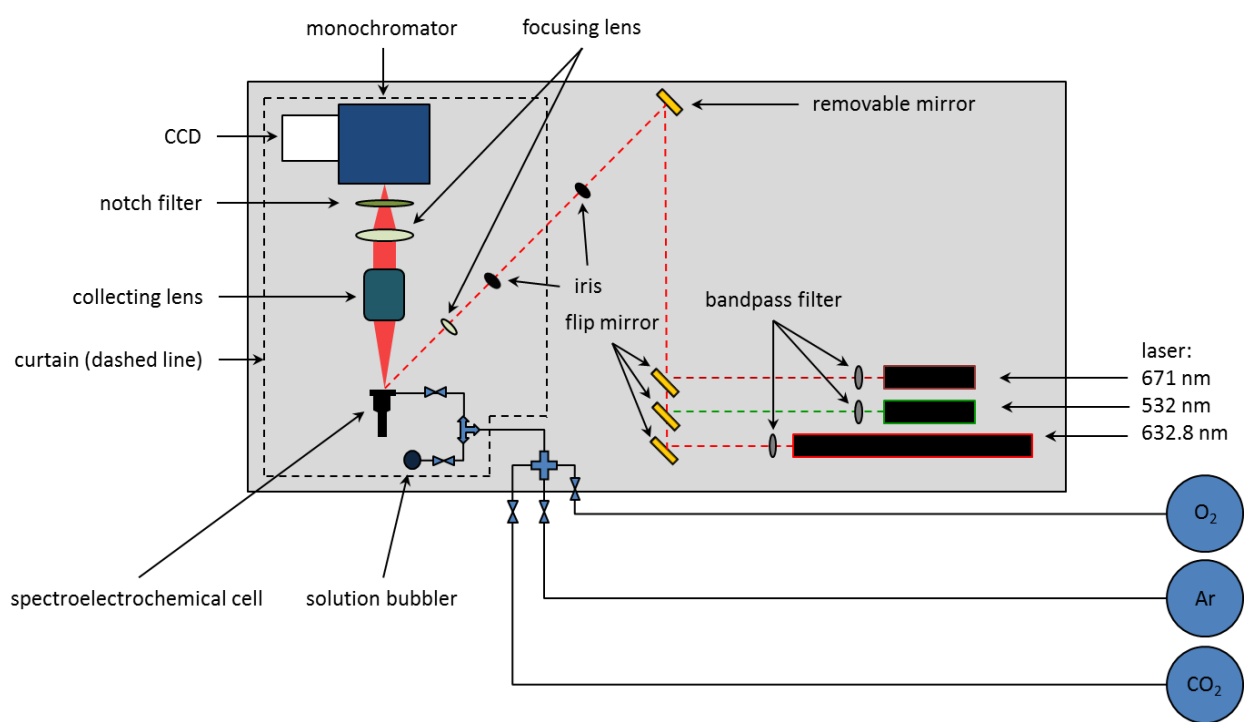


Figure 2.6: Design of the Raman/SERS instrument.

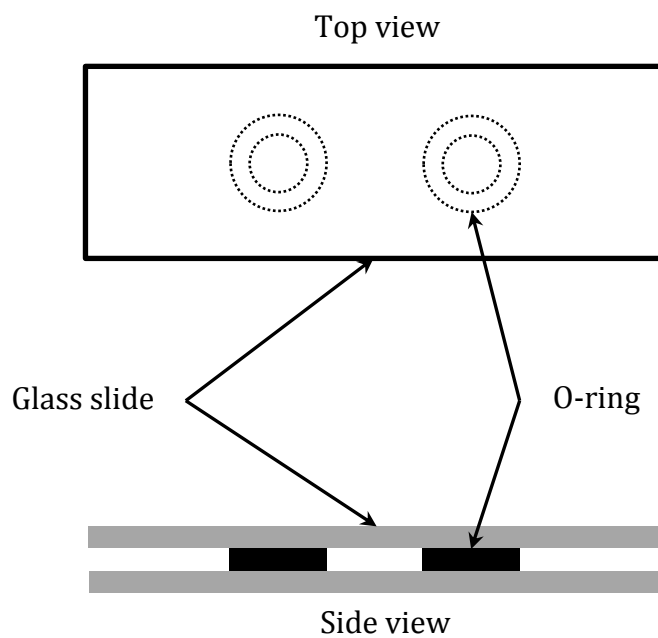


Figure 2.7: Diagram illustrating the Raman sample holder for powders and hazardous materials.

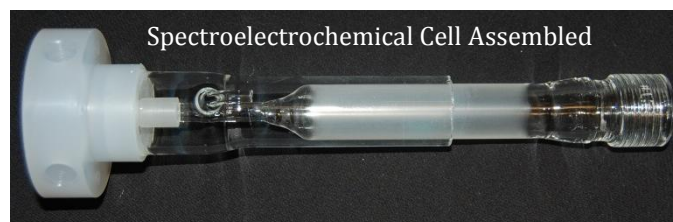
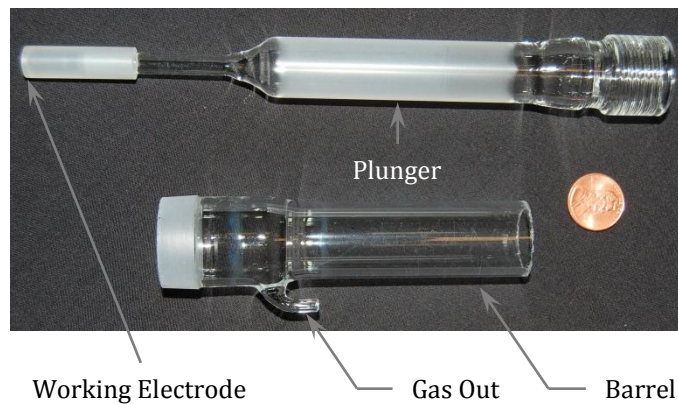
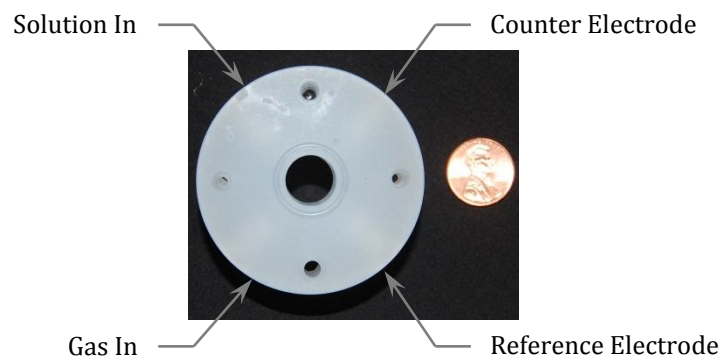


Figure 2.8: Spectroelectrochemical cell for SERS experiments. Contact is made to the working electrode via a wire/spring passing through the inside of the plunger to the back of the electrode. The working electrode is secured to the end of the plunger with Teflon tape.

2.8. References

1. T. Will, M. Dietterle and D. M. Kolb, in *Nanoscale Probes of the Solid/Liquid Interface*, eds. A. A. Gewirth and H. Siegenthaler, Kluwer Academic Publisher: Dordrecht, 1995,
2. Z.-Q. Tian, B. Ren and D.-Y. Wu, *The Journal of Physical Chemistry B*, **106**, (37), 9463-9483, (2002)
3. J. E. Pemberton, S. L. Joa, A. Shen and K. J. Woelfel, *Journal of the Chemical Society, Faraday Transactions*, **92**, (20), 3683-3691, (1996)
4. I. Horcas, R. Fernandez, J. M. Gomez-Rodrigues, J. Colchero, J. Gomez-Herrero and A. M. Baro, *Rev. Sci. Instrum.*, **78**, (1), 013705, (2007)
5. M. E. Biggin, *In Situ Vibrational Spectroscopic and Electrochemical Study of Electrodeposition Additives on Copper Surfaces*, University of Illinois at Urbana-Champaign: Urbana, (2001)
6. J. F. Li, Y. F. Huang, Y. Ding, Z. L. Yang, S. B. Li, X. S. Zhou, F. R. Fan, W. Zhang, Z. Y. Zhou, D.-Y. Wu, B. Ren, Z. L. Wang and Z.-Q. Tian, *Nature*, **464**, (7287), 392-395, (2010)
7. *Spartan '08*, ed, Wavefunction, Inc., Irvine, CA,
8. Y. Shao, L. F. Molnar, Y. Jung, J. Kussmann, C. Ochsenfeld, S. T. Brown, A. T. B. Gilbert, L. V. Slipchenko, S. V. Levchenko, D. P. O'Neill, R. A. DiStasio Jr, R. C. Lochan, T. Wang, G. J. O. Beran, N. A. Besley, J. M. Herbert, C. Yeh Lin, T. Van Voorhis, S. Hung Chien, A. Sodt, R. P. Steele, V. A. Rassolov, P. E. Maslen, P. P. Korambath, R. D. Adamson, B. Austin, J. Baker, E. F. C. Byrd, H. Dachsel, R. J. Doerksen, A. Dreuw, B. D. Dunietz, A. D. Dutoi, T. R. Furlani, S. R. Gwaltney, A. Heyden, S. Hirata, C.-P. Hsu, G. Kedziora, R. Z. Khalliulin, P. Klunzinger, A. M. Lee, M. S. Lee, W. Liang, I. Lotan, N. Nair, B. Peters, E. I. Proynov, P. A. Pieniazek, Y. Min Rhee, J. Ritchie, E. Rosta, C. David Sherrill, A. C. Simmonett, J. E. Subotnik, H. Lee Woodcock Iii, W. Zhang, A. T. Bell, A. K. Chakraborty, D. M. Chipman, F. J. Keil, A. Warshel, W. J. Hehre, H. F. Schaefer Iii, J. Kong, A. I. Krylov, P. M. W. Gill and M. Head-Gordon, *Physical Chemistry Chemical Physics*, **8**, (27), 3172-3191, (2006)

Chapter 3. Potential Dependent Chromate Adsorption on Gold

Reproduced with permission from the Journal of the Electrochemical Society, 156, (11), D497-D502, 2009. Copyright 2009, The Electrochemical Society. This work was funded by the National Science Foundation.

3.1. Introduction

The chromate anion is of interest due to its wide industrial applications as well as its negative environmental impact. Industrially, chromate is involved in the production of pigments, used to make adhesion layers, involved in the production of stainless steels and other metallurgy, and very important in many corrosion resistance processes.^{1,2}

The relatively high mobility of the chromate anion in the environment as well as its toxicity has made it an important target for remediation efforts.³⁻⁵ In fact, the negative impacts of chromium(VI) containing compounds have led to efforts for its replacement in industrial processes.^{2, 6-8} Recent efforts for chromate remediation involve nanoscale Fe⁰, used as a barrier to reduce hexavalent chromium compounds to insoluble chromium(III) compounds.⁵ Although the Fe⁰ nanoparticles have been shown to be effective in reduction of the chromium(VI) to chromium(III), concerns have been raised concerning the delivery and stability of the particles in the barrier.⁹

The importance of chromate remediation and industrial use has prompted many studies examining chromium association with metallic surfaces. McCreery and coworkers studied the formation of chromate conversion coatings on Cu and Al alloys.⁶⁻⁸ During the formation of a chromium conversion coating they suggested that the chromium(III) oxide

layer formed was one to two monolayers thick, and proposed a simple mechanism for Cr deposition. Compton *et al.* studied the mechanism of electrochemical reduction of chromate for the purpose of environmental remediation in acidic media.² Varga and coworkers followed the electrochemical deposition of chromate on Au and Pt using *in situ* radiotracer chemistry. Based on their observations they propose that the chromate is deposited in a single monolayer.^{10, 11} The oxidation and reduction of chromium(III)/chromium(VI) on gold electrodes in basic solution has been studied to better understand the importance of chromate as an additive in the chlorate process.¹² These authors found that Cr^{III} oxidation behavior was dependent on electrode pretreatment.

Chromate deposition has been widely studied on various substrates and under varying conditions: gold has been explored extensively in basic¹²⁻¹⁴ and acidic¹⁵⁻¹⁷ chromate solutions as well as silver,¹⁸⁻²¹ platinum,²²⁻²⁴ copper,⁷ aluminum alloys,^{8, 25-28} iron,²⁹⁻³¹ steel,³² and other modified surfaces^{2, 33-42}

Despite the plethora of work on the Cr deposition and reduction topic, several questions remain unclear. There is little understanding of the mechanism of reduction in the neutral electrochemical environment which is possibly more relevant to remediation in natural waters. The identification of intermediates and the morphological consequences of Cr^{VI} reduction, including the structure of the Cr^{III} oxide film remain unclear. In the current study, cyclic voltammetry (CV), surface enhanced Raman spectroscopy (SERS), and probe microscopy are used to elucidate previously unknown details of the chromium(VI) to chromium(III) reduction.

3.2. Results

3.2.1. Voltammetry

Figure 3.1 shows a cyclic voltammogram from an annealed Au on glass electrode obtained in a solution containing 200 μM Na_2CrO_4 + 0.1 M KCl at pH 3 adjusted by HCl. In the absence of Na_2CrO_4 , the voltammogram shows neither reductive nor oxidative peaks, as has been observed previously.⁴³

Upon addition of chromate, the voltammogram changes considerably and develops as a function of scan history between -0.6 and $+0.8$ V vs. Ag/AgCl. Figure 1A shows that on the first scan following the addition of chromate, the CV evinces a large cathodic peak (peak A) and a somewhat smaller wave (peak D) on the oxidative sweep. The cathodic peak is associated with the reduction of solution chromate to Cr^{III} , as has been observed previously in a slightly different electrolyte.² The anodic peak is likely associated with reoxidation of solution Cr^{III} .

After 2 cycles, the oxidative wave evolves and diminishes in extent. The diminished oxidative wave suggests that the electrode surface is coated with a film that minimizes electron transfer to the solution, thus diminishing the amount of solution chromate that can be reduced. Concomitant with the diminished degree of solution chromate reduction is the appearance of an additional oxidative wave in the voltammetry. This new wave, peak C, persists for two more cycles before the development of a stable voltammogram at cycle 5. In this voltammogram, oxidative features (peaks E and F) are observed at 350 and 430 mV vs. Ag/AgCl and a reductive feature (peak G) is seen at 330 mV vs. Ag/AgCl

Figure 1B shows the scan rate dependence of peak E. The graph shows that the peak current density is linearly dependent ($R^2 = 0.999$ for peak E) on the scan rate. This indicates that the reaction associated with this feature is surface-confined.⁴⁴ A similar analysis of peaks F and G reveals that their respective reactions are also surface-confined ($R^2 = 0.998$ for peak F and 0.985 for peak G).

The voltammetry we report at pH 3 has parallels with that obtained in basic solution on Au(111) by Skoluda.¹² This researcher also observed two oxidative peaks associated with Cr^{III} oxidation at the Au surface. However, he found differences in the voltammetry on the basis of surface preparation. McCreary and co-workers⁶⁻⁸ also observed several Cr^{III} and Cr^{IV} related species on Ag, Cu, and Al, although the potential was not cycled in that work.

3.2.2. SERS

To further examine compositional changes to the electrode surface we performed in situ SERS measurements. Figure 3.2 is a series of SERS spectra obtained from a roughened Au surface taken at potentials between -400 mV and 600 mV in a solution containing 200 μ M Na₂CrO₄ + 0.1 M KCl at pH 3. In Figure 3.2a there are four peaks (labeled 1, 2, 3, and 4). Peak 1 is associated with the symmetric stretch of CrO₄²⁻³⁴ while Peaks 2 and 3 are associated with the E_g and A_{1g} stretches of Cr₂O₃ respectively⁴⁵. Peak 4 is associated with the Au - Cl stretch⁴⁶, expected in this Cl⁻-containing solution at positive potentials.

The first potential cycle, Figure 3.2a (anodic scan) and 2b (cathodic scan), shows the adsorption of chromate on a Au surface immersed in the chromate-containing solution described previously. Initially, at -400 mV, only Peak 2 is present. As the potential is

increased, the intensity of Peak 2 diminishes. Peak 1 grows in starting at about 0 mV. Peak 3 is noticeable at 200 mV. During the cathodic scan peaks 1 and 3 decrease in intensity. Peak 4 starts to develop at 100 mV.

Figure 3.2c is a series of SERS spectra obtained immediately following those contained in Figure 2b and under the same conditions. Figure 2c is the anodic scan, conducted between -600 mV and 600 mV. Starting at -600 mV peaks 2 and 3 are present. As the scan progresses, peak 3 diminishes and then peak 2 also disappears; both are gone at 400 mV. Peak 4 is observed at 100 mV and becomes stronger as the potential is increased. In place of Peak 1 found at 848 cm^{-1} , another peak, Peak 1' is observed at 800 cm^{-1} . This energy for the Cr - O stretch following CrO_4^{2-} deposition has been observed previously on Ag and was linked with chemical association of the CrO_4^{2-} with the Ag electrode surface. In this case, the Cr - O stretch was also found at 800 cm^{-1} . The similarity in energy between the Ag and Au cases is not surprising. The binding energies for sulfate on silver and gold are 159 kcal/mol and 164 kcal/mol respectively.^{47, 48} The Raman shift for Cl^- on gold is 255 cm^{-1} while Cl^- on Ag is at 240 cm^{-1} .^{46, 49}

During the cathodic scan, the energy of peak 1' shifts again from ca. 800 cm^{-1} to a new energy of 858 cm^{-1} and leads us to designate this peak as Peak 1''. Once this peak is established, the energy of this peak is constant throughout this and all subsequent potential scans.

The behavior of Peaks 1, 1', and 1'' is shown in Figure 3.3 which is a plot of the potential dependence of their intensities. The increase of peak 1 during the first anodic scan is due to the adsorption of chromate to the surface and is followed by decreased

intensity likely due to the cathodic reduction of chromate to a chromium(III) species. The intensity profile of the third cycle mirrors that of the first cycle, though the overall intensity change of peak 1'' is considerably less. Contrarily, the intensity profile of peak 1' is substantially different from either of the peaks represented in Figure 3.3. The intensity of peak 1' reaches maximal intensity between 200 and 300 mV vs. Ag/AgCl.

Peak 5, at 946 cm^{-1} , grows-in at 200 mV. Michel *et al.*⁵⁰ and Stammreich *et al.*⁵¹ assigned peaks at 943 cm^{-1} and 946 cm^{-1} , respectively, to $\nu_{(\text{as})}(\text{CrO}_3)$ for the dichromate anion. However, the symmetric stretch, at 904 cm^{-1} reported by both these authors for the (CrO_3) moiety of $\text{Cr}_2\text{O}_7^{2-}$ is not present in any of our spectra. Peak 5 goes away during the same interval. Peak 4 decreases and is no longer present after 100 mV. Peak 2 is present between 300 mV and -100 mV . Peak 3 grows-in at 100 mV and becomes very broad, encompassing peak 2 as the potential becomes more negative.

Figure 2e is another series of SERS spectra obtained during the next potential cycle and immediately following the spectra shown previously. In Figure 2e, during the anodic scan, peaks 1'', 2, and 3 are initially present at 0 mV. Peak 4 grows-in at 100 mV. Peak 3 decreases in intensity as the scan moves positive. A new broad peak with weak intensity, peak 6, grows-in at 446 cm^{-1} as the peak 3 intensity decreases. Michel and co-workers described a similar peak, at 440 cm^{-1} , that they assigned to a chromium chloride symmetric stretch when HCl was added to a solution of dichromate.⁵⁰ Peak 1'' increases in intensity as the potential becomes positive. Figure 2f is the cathodic scan. Peak 1'' decreases in intensity as do peaks 2, 4, and 6. While peak 6 decreases peak 3 increases. Peak 3 again

overtakes peak 1 and 6, becoming very broad. Subsequent voltammetric scans did not reveal any evolution in the spectra beyond that shown in Figures 2e and 2f.

Assignments and energies for all the SERS peaks are reported in Table 3.1.

3.2.3. *In Situ EC-STM and EC-AFM*

Figure 3.4 is a series of AFM images showing the potential-dependent evolution of the Au surface following immersion into a solution containing 40 μM chromate and 0.1 M KCl. The first image obtained at -150 mV shows a terrace and steps. The step heights are 0.23 nm, which is close to that expected for a bare Au surface (0.24 nm). Lattice resolution images obtained at -150 mV vs. Ag/AgCl (Figure 3.5B) show a hexagonal structure and a spacing of 0.288 ± 0.012 nm, which is again close to that expected for a Au(111) surface. An island, marked with an arrow and also evincing the 0.23 nm step height, is observed isolated on the terrace.

The presence of Au islands on the terrace is not unprecedented, due to the lifting of the Au(111) reconstruction expected at these potentials. The reconstructed surface is 4.5 % more dense than the unreconstructed surface. When the reconstruction is lifted the extra gold atoms are expelled to the surface forming flat monolayer cluster islands. Islands below a critical size (~ 100 nm²) are unstable and in a process similar to Ostwald ripening contribute to the growth of those islands that are larger than the critical size.^{52, 53}

Increasing the potential leads to changes in the overall morphology of the surface. At -50 mV, the isolated feature atop the Au terrace becomes larger and the step height increases to 0.35 nm. At 200 mV the island height has decreased below the level of noise in the image. By 300 mV the island is no longer visible. This potential is associated with the onset of chromate association with the surface, as seen in the SERS and the CV.

At 500 mV, further changes in the surface structure are observed. Step heights average 0.23 nm at -150 mV, 0.23 nm at -50 mV, and 0.29 nm at 300 mV. At 500 mV the step heights for the three steps visible are 0.45 nm. Between -150 mV and 500 mV the number of steps decreases from 6 to 3.

As the cathodic scan commences, images show that the step edge has receded further and is no longer round. By 0 mV the step edge has become more serrated and pitting, indicated by the circle, has started to appear. As -200 mV is approached, pitting in the top terrace is very prevalent. The final frame in the sequence takes place at -200 mV after being held at that potential for several minutes. The stabilization of the surface is evident by the decrease in observed pits; in addition the appearance of an island similar to the one in the first image begins to appear as indicated by the arrow.

Figure 3.5 shows AFM images of the Au surface before and after chromate adsorption. Figure 3.5A shows a lattice resolved AFM image of the Au surface obtained at -150 mV in a solution containing 0.1 M KCl (adjusted to pH 3). The image exhibits atomic scale features with a 0.29 nm hexagonal structure which is the structure expected for a Au(111) surface. While halide structures for I^- and Br^- on Au(111) exhibit adlattices different from the underlying Au, there have been no reports of Cl^- adlattice visualization on Au(111) by AFM.⁵⁴ Figure 3.5B was obtained at -150 mV in a solution containing 40 μ M Na_2CrO_4 + 0.1 M KCl adjusted to pH = 3 following three potential scans between -200 mV and +500 mV as described above. The surface still evinces a hexagonal structure seen in Figure 3.5A, but the feature spacing is now 0.49 ± 0.02 nm. The adlattice is also rotated 25 ± 5 degrees relative to the initial Au surface. This spacing and structure suggests the formation of a $(\sqrt{3} \times \sqrt{3})R30^\circ$ adlattice following chromate adsorption.

Because SERS data suggest that the dominant species on the surface at these negative potentials is a Cr^{III} species, we inspected possible Cr^{III} bulk structures for Cr – Cr spacings that might appropriately mimic those seen in Figure 3.5B. These possibilities are listed in Table 3.2. The best fit to the ($\sqrt{3}\times\sqrt{3}$)R30° adlattice was provided by α -Cr₂O₃ which exhibits bulk Cr – Cr spacings of 0.49 nm.⁵⁵ Figure 3.6 shows how a ($\sqrt{3}\times\sqrt{3}$)R30° adlattice of (0001) α -Cr₂O₃ might register with the underlying Au(111) surface. Zhang *et al.* also observed formation of a ($\sqrt{3}\times\sqrt{3}$)R30° (0001) α -Cr₂O₃ adlattice on Pt(111) after annealing a chromium oxide film formed through chemical vapor deposition.²³

Figure 3.7 contains *in situ* EC-STM images of Au-on-glass obtained at various potentials in a solution containing 40 μ M Na₂CrO₄ + 0.1 M KCl and adjusted to pH ~ 3. At -200 mV, the image evinces steps with a height of 0.25 nm, close to that expected for Au(111). Figure 3.7A, obtained at -200 mV vs. Ag/AgCl, shows a large atomically flat terrace and relatively smooth step edges typical of a Au(111) surface. As the potential is increased to -100 mV, Figure 3.7B, the step edges start to become rough. At 0 mV vs. Ag/AgCl, Figure 7C, the step edges exhibit extreme serration and the start of island formation is observed. When the potential is held at 0 mV, further disruption of the edges is seen as well as lateral growth of the islands, shown in Figure 3.7D.

The cross-sectional profile presented in Figure 3.7E shows that the islands maintain an atomically flat profile which suggests that they grow laterally, rather than vertically on the Au surface. The histogram (Figure 3.7F) shows that the average island height measured is about 3 Å. The height of the islands is larger than that expected for a Au(111) monatomic step (0.24 nm) and suggests that they are associated with chromate adsorption.

Figure 3.8 shows a series of *in situ* EC-STM images obtained in a solution containing 40 μM Na_2CrO_4 + 0.1 M KCl adjusted to a pH 3 while the potential was maintained at 0 mV following potential excursion to +500 mV; the chromate layer at this potential is being stripped from the Au(111) surface. The circled areas in the images show pitting that is occurring in the surface. As time progresses, the frequency of pitting increases; however, the chromate layer is not completely removed from the surface. The arrows show the retreat of the step edge. The islands near the step edges do not change in height or profile during the time in which the potential is held, about 10 minutes. Further the islands observed during the cathodic sweep are the same height as the islands in Figure 3.7. Also, the nearly all of the islands are on the top of the step edges.

3.3. Discussion

At cathodic potentials CrO_4^{2-} spontaneously adsorbs on surfaces to yield a series of reduced Cr species, the exact nature of which depends on applied potential, solution conditions, and the amount of time the substrate contacts the Cr-containing solution.^{7,56} In our measurements CrO_4^{2-} is deposited onto a Au substrate, and different species are observed at different potentials. The nature of the Cr-containing overlayer also changes as a function of number of cycles.

The voltammetry shows that an oxidized species is reduced at negative potentials, as expected. However, the voltammetry also reveals the presence of anodic waves which show that the reduced species can be reoxidized at positive potentials. The potential of both the anodic and cathodic peaks changes as a function of cycle number, which shows that the Cr-covered surface evolves as a function of cycle. On the first sweep, the reduced

species is more easily oxidized than is found on later cycles. All of the species are found to be surface-confined.

SERS provides insight into the different species on the surface. Chromium(III) oxide and chromate make up the first species on the surface where oxidation and reduction occurs in the first scan in the electrochemistry. Peak 1 grows in at the same potential as that of the onset of the first oxidation wave seen in the first scan of the CV. Similarly, in both the STM and AFM images, deposition also coincides with the occurrence of peak 1 in the SERS spectra indicating that the material being deposited is chromate. The cathodic scan of both the SERS and CV show the reduction of chromate at the surface to a chromium(III) species. Following the first potential cycle, the SERS spectra demonstrate the presence of an intermediate species, chromate chemically bound to the surface. The onset of peak 1' agrees well with wave C of the electrochemistry. The presence of the 946 cm^{-1} anti-symmetric dichromate stretch might suggest that new chromate coming to the surface is binding to the $\text{Cr}^{\text{VI}}\text{O}_4 - \text{Au}_{(\text{surface})}$ species at the interface. This intermediate species continues its transformation during the reduction sweep of the second SERS cycle as it is reduced to Cr_2O_3 at 300 mV which is in agreement with the third CV in Figure 3.1. The final cycle of SERS spectra give us insight into the chemical make-up of the stable species present on the surface during the fifth CV of Figure 3.1. Although it is made up of a mixed $\text{Cr}^{\text{III}}/\text{Cr}^{\text{VI}}$ oxide, it fluctuates between predominately Cr^{III} during the cathodic sweep and Cr^{VI} during the anodic sweep as can be seen in the spectra in Figure 2e and 2f. The oxidation of the Cr^{III} species to Cr^{VI} can be seen with the intensification of peak 1'' while the chromium(III) oxide peaks diminish near the onset of wave E in the voltammetry; further, the reverse occurs in accordance with the onset of wave G in the voltammetry. Integration

of wave G in the voltammetry suggests that between 2 and 2.5 e⁻ are utilized per Cr center (calculated assuming a 1/3 coverage Cr adlattice forms on the Au(111) as indicated by the AFM) which is consistent with the partial oxidation of the surface to the mixed oxide species. Neither the SERS nor the voltammetry provide any evidence that species more reduced than Cr^{III} are present on the surface, as expected since the formal potential for Cr⁰ formation from Cr^{III} occurs at -547 mV vs. Ag/AgCl.

AFM shows that the initially clean surface is covered by what must be a thick Cr-containing overlayer which covers the steps edges of the initially pristine Au surface and yields a new surface morphology. The changes observed in AFM suggest that multilayers of Cr^{III} grow on steps and that the Cr overlayer does not grow conformally on the Au surface. Interestingly, Zhang and co-workers observed that on Pt(111) Cr₂O₃ also grew preferentially on the step edges during chemical vapor deposition.²³ This observation may be a reflection of the affinity of Cr^{III} oxide for itself relative to the underlying Au. The behavior of the pillbox feature in the AFM images suggests that strong lateral and normal growth on initially deposited Cr occurs. The pileup of material at terraces above step edges, seen in the STM, also strongly emphasizes the affinity of the Cr oxide for itself, relative to the Au surface.

Lattice resolved AFM images suggest that the stable species is a Cr^{III} oxide, which does grow in registry with the underlying Au surface, at least at negative potentials. We were unable to resolve the lattice formed at more anodic potentials. As mentioned above, Zhang *et al.* observed the formation of a ($\sqrt{3} \times \sqrt{3}$)R30° adlattice on Pt(111). They report that the lattice mismatch for the Pt(111) surface and the α -Cr₂O₃ (0001) surface which

constricted the adlattice by about 3%. The larger atom spacing for Au(111), 2.88 Å, compared to Pt(111), 2.77 Å, should provide a better match with the α -Cr₂O₃ (0001) surface.²³

The above observations suggest that the mechanisms displayed in Figure 3.9 are operative during cathodic and anodic cycling of the surface during the formation of the overlayer. This proposed mechanism takes into account the species observed in the SERS as well as the voltammetry. *N* values obtained from the chromate reduction wave in the first voltammetric scan in Figure 3.1 are 6 electrons, which matches well with the first cycle of the mechanism. Integration of the same peak in the third and fifth voltammetric scans provides a value of 2.5 electrons, which also supports the proposed mechanism.

In conclusion, physical methods show that CrO₄²⁻ adsorbed on a Au surface cycles between a relatively thick, multilayer consisting predominantly of Cr^{VI} at anodic potentials and a thinner, predominantly Cr₂O₃ adlattice at more cathodic potentials. The ease of conversion between the two forms may provide a way to facilitate Cr^{VI} remediation in natural waters.

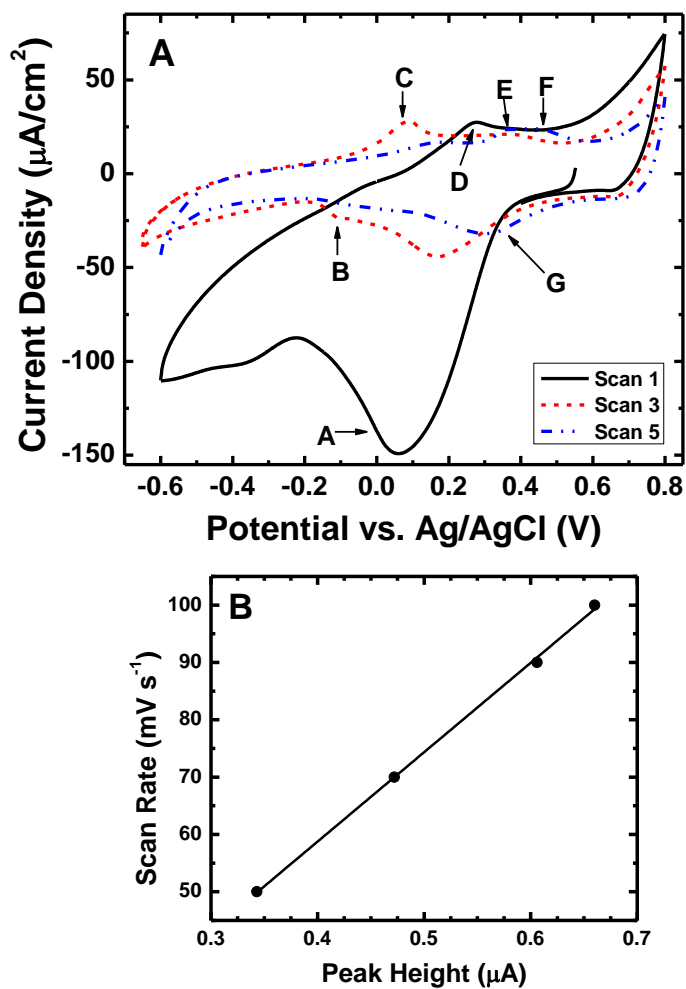


Figure 3.1: Cyclic voltammetry and scan rate dependence vs. peak height of a Au on glass electrode in a solution containing $200 \mu\text{M Na}_2\text{CrO}_4 + 0.1 \text{ M KCl}$ at pH of 3. Graph A shows the evolution of the cyclic voltammogram with each scan. A plot of wave E, graph B, was derived from scan rate dependence studies of the stable species following the fifth scan. Graph B demonstrates a linear correlation between the scan rate and peak height indicating that this peak represents a surface-confined species.

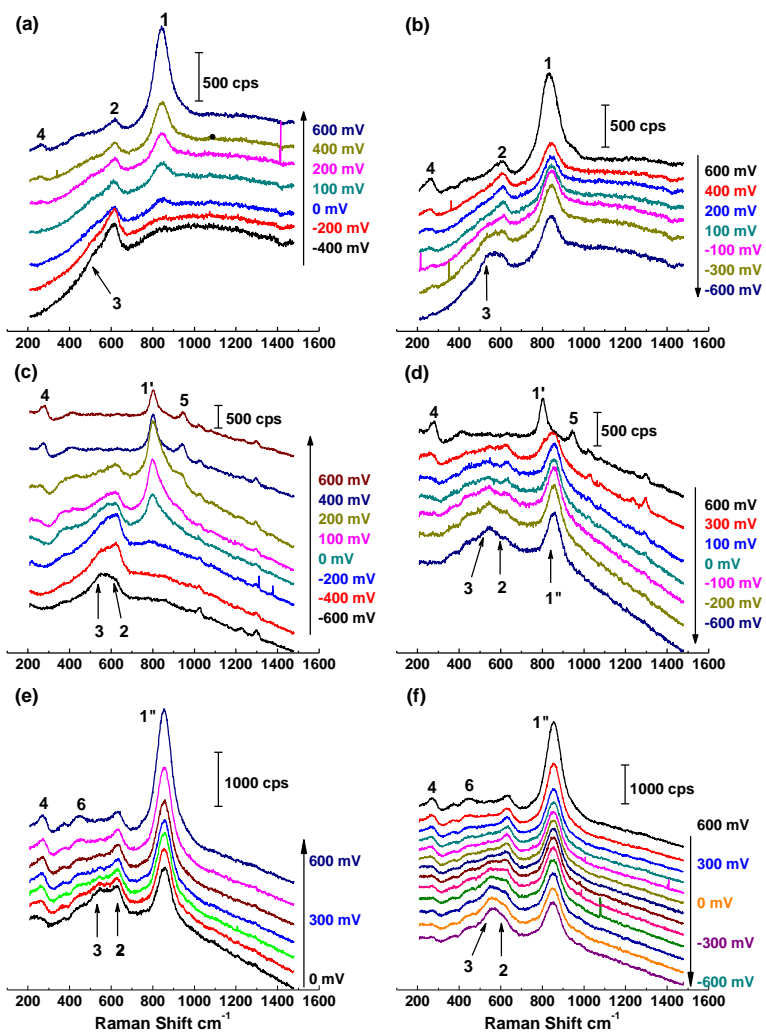


Figure 3.2: In situ SERS spectra of a roughened gold surface. Solution contains 200 μM Na_2CrO_4 + 0.1 M KCl adjusted to pH 3 with HCl. (a) anodic scan first sweep. (b) cathodic first sweep. (c) anodic scan of second sweep. (d) cathodic scan of second sweep. (e) anodic scan of third sweep. (f) cathodic scan of third sweep.

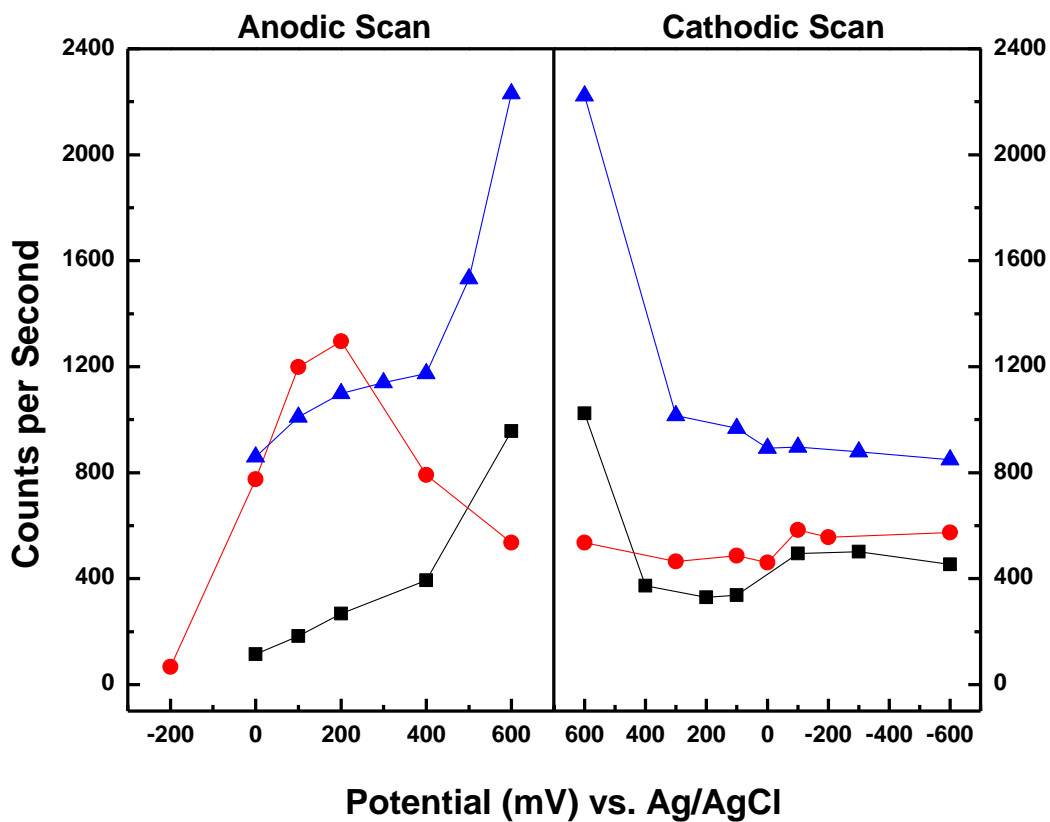


Figure 3.3: Potential vs. intensity plots for peaks 1, 1', and 1''. The squares represent peak 1 in the first scan. The circles are peak 1' in the second scan. The triangles are peak 1'' in the third scan.

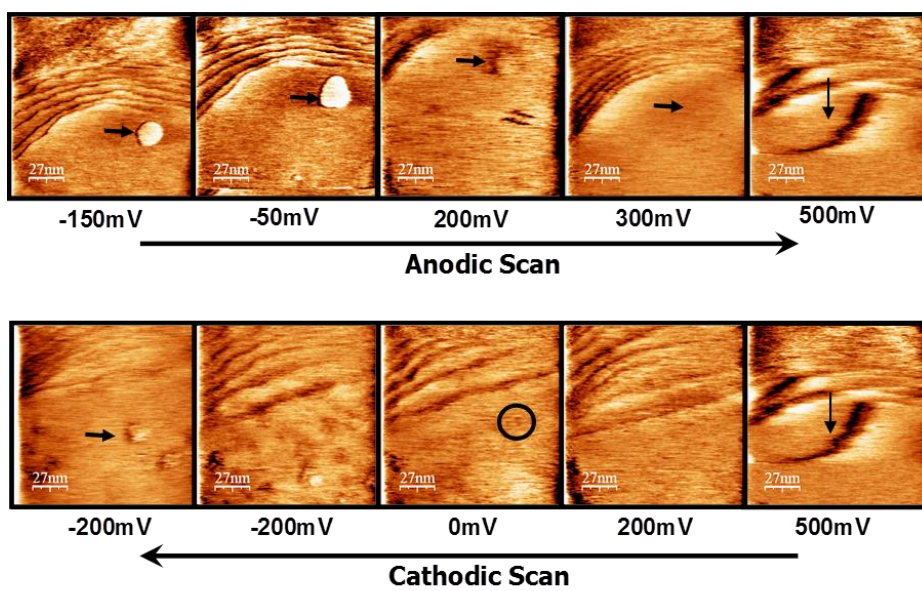


Figure 3.4: *In situ* EC-AFM images of Au(111) on glass under potential control in a 40 μM Na_2CrO_4 + 0.1 M KCl solution at pH 3.

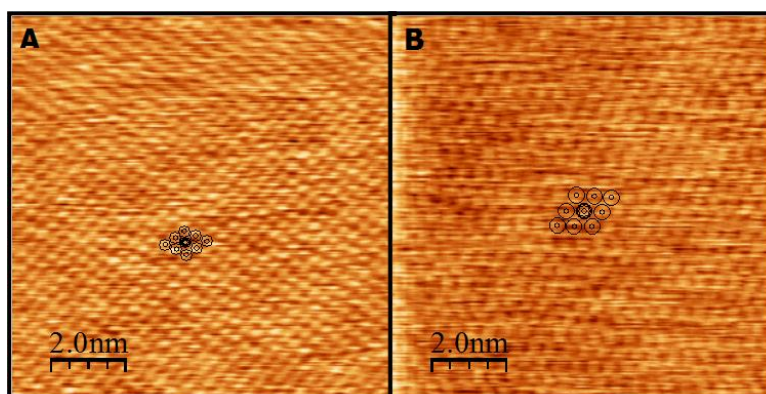


Figure 3.5: A) AFM image of lattice resolved Au(111) in a solution containing 0.1M KCl adjusted to pH 3 with HCl. B) AFM image of $(\sqrt{3} \times \sqrt{3})R30^\circ$ adlayer formed on the gold on glass substrate, the solution contained $40 \mu\text{M Na}_2\text{CrO}_4 + 0.1 \text{ M KCl}$ adjusted to pH 3 with HCl.

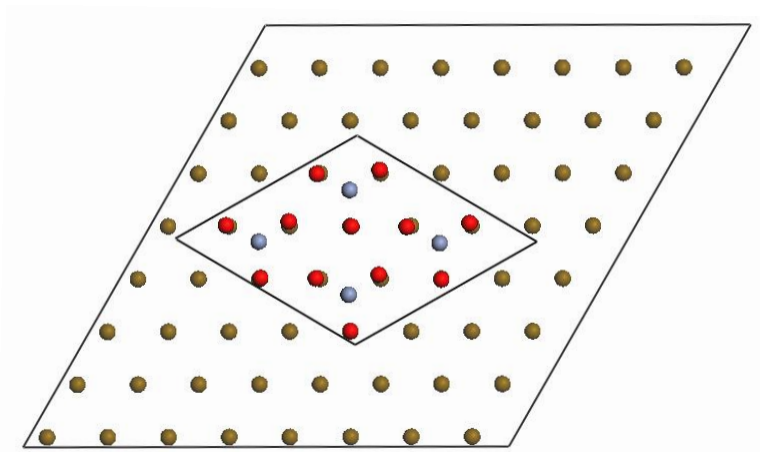


Figure 3.6: A representation of the $(\sqrt{3} \times \sqrt{3})R30^\circ$ adlattice, composed of the (0001) surface of α - Cr_2O_3 , that is observed following deposition of chromate.

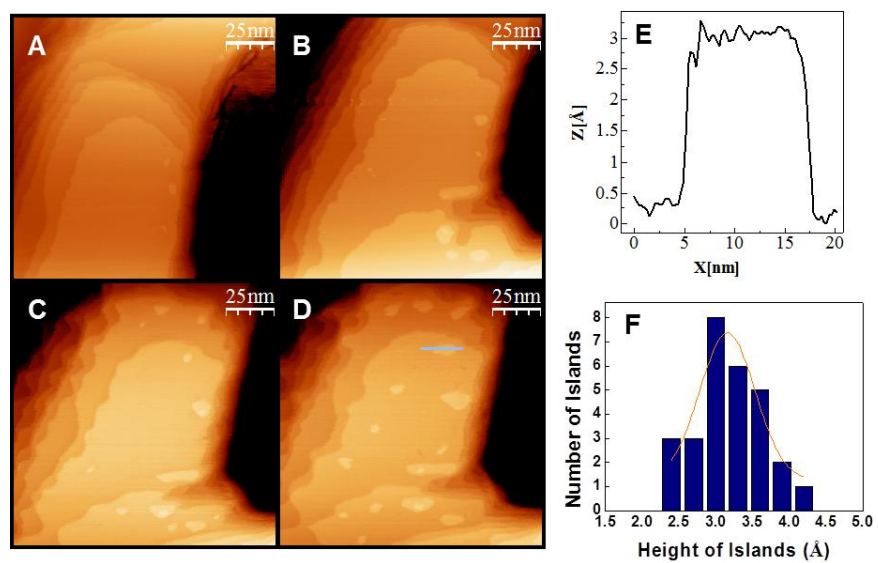


Figure 3.7: *In situ* EC-STM of Au(111) on glass under potential control in a 40 μM Na₂CrO₄ + 0.1 M KCl solution at pH 3. A) shows a clean Au surface at -200 mV. B) shows a slight change in the step edge at -100 mV. C) shows more serration of the step edge and the beginnings of deposition at 0 mV. D) shows the formation of islands on the surface and the continued change in the step edge still at 0 mV. E) and F) show that the islands are flat with an average height around 3 Å.

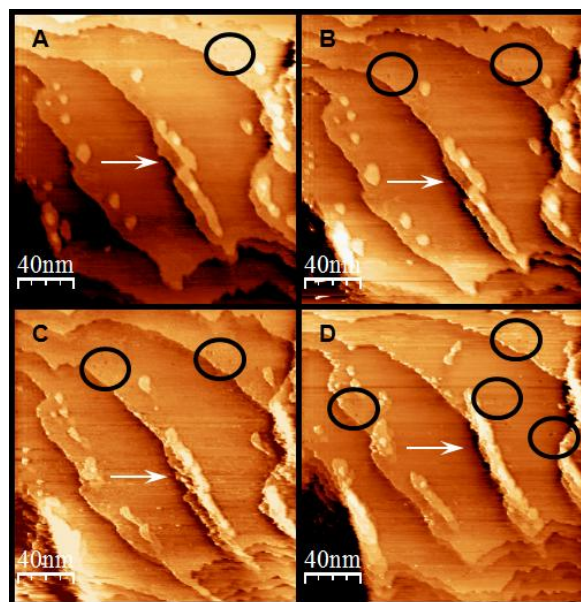
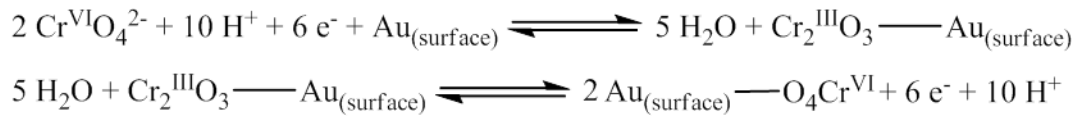
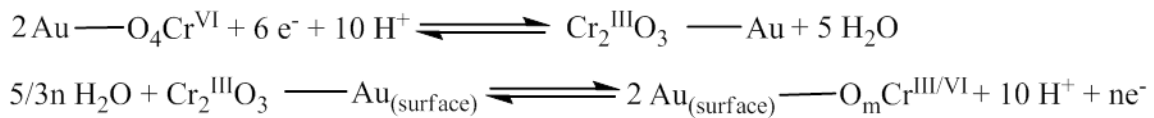


Figure 3.8: *In situ* EC-STM of Au(111) on glass held at a potential of -100 mV vs. Ag/AgCl in a $40 \mu\text{M}$ Na_2CrO_4 + 0.1 M KCl solution at pH 3. As time progresses pitting is observed in the surface seen indicated by the circles. Also seen is the retreat of the step edge identified by the arrows.

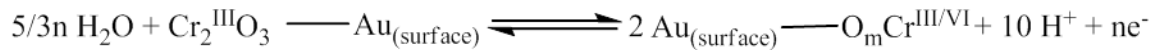
Cycle 1



Cycle 2



Cycle 3



The surface cycles between $\text{Au}_{(\text{surface})} \text{---} \text{O}_m\text{Cr}^{\text{III/VI}}$ and $\text{Cr}_2^{\text{III}}\text{O}_3 \text{---} \text{Au}$

Where m = 3 or 4 and n = 0 or 3

Figure 3.9: Proposed mechanism for $\text{Cr}^{\text{III/VI}}$ mixed oxide film formation. Cycle 1 initiates the formation of the film by the adsorption of chromate to the surface followed by reduction to a Cr^{III} surface-confined species. Cycle 2 represents the intermediate film, involving the oxidation of the surface-confined Cr^{III} to a surface-confined Cr^{VI} species and the addition of more chromate to the surface. Cycle 3 shows the incomplete oxidation/reduction of the stable surface film.

Table 3.1: SERS peak assignments

Peak	Wavenumber (cm ⁻¹)	Description	Reference
1	848	ν_s (CrO)	34
1'	800	ν_s (CrO) bound to Au	57
1''	858	ν_s (CrO) Cr ^{III} /Cr ^{VI} mixed oxide	25
2	625	Cr ₂ O ₃ A _{1g}	45
3	550	Cr ₂ O ₃ E _g	45
4	265	ν (Au – Cl)	46
5	946	$\nu_{(as)}$ (CrO ₃) Dichromate	50, 51
6	446	ν (CrCl)	50

Table 3.2: Possible species, and their spacing, considered for the adlattice observed on the surface

Compound	Chromium – Chromium Spacing (nm)	Reference	Crystal System
Cr ³⁺ O(OH)	0.2974	58	Orthorhombic
HCrO ₂	0.2968	59	Rhombohedral
CrO(OH)	0.2979	60	Hexagonal
CrOCl	0.3182	61	Orthorhombic
CrO(OH)	0.2995	62	Orthorhombic
CrO ₂	0.2917	63	Tetragonal
α - Cr ₂ O ₃	0.4962	55	Rhombohedral
Cr ₃ O ₈	0.3280	64	Orthorhombic
HCrO ₂	0.2982	65	Rhombohedral
NaCrO ₂	0.2975	66	Rhombohedral

3.4. References

1. D. Golub and Y. Oren, *Journal of Applied Electrochemistry*, **19**, (3), 311-316, (1989)
2. C. M. Welch, O. Nekrassova and R. G. Compton, *Talanta*, **65**, (1), 74-80, (2005)
3. C. Gong and R. J. Donahoe, *Applied Geochemistry*, **12**, (3), 243-254, (1997)
4. N. Melitas and J. Farrell, *Environmental Science & Technology*, **36**, (24), 5476-5482, (2002)
5. B. A. Manning, J. R. Kiser, H. Kwon and S. R. Kanel, *Environmental Science & Technology*, **41**, (2), 586-592, (2007)
6. W. J. Clark, J. D. Ramsey, R. L. McCreery and G. S. Frankel, *Journal of the Electrochemical Society*, **149**, (5), B179-B185, (2002)
7. B. L. Hurley and R. L. McCreery, *Journal of the Electrochemical Society*, **150**, (8), B367-B373, (2003)
8. J. D. Ramsey and R. L. McCreery, *Journal of the Electrochemical Society*, **146**, (11), 4076-4081, (1999)
9. J. T. Nurmi, P. G. Tratnyek, V. Sarathy, D. R. Baer, J. E. Amonette, K. Pecher, C. Wang, J. C. Linehan, D. W. Matson, R. L. Penn and M. D. Driessen, *Environmental Science & Technology*, **39**, (5), 1221-1230, (2005)
10. K. Varga, I. Szaloki, L. Gancs and R. Marczona, *Journal of Electroanalytical Chemistry*, **524-525**, 168-175, (2002)
11. R. Bujak and K. Varga, *Electrochimica Acta*, **52**, (1), 332-341, (2006)
12. P. Skoluda, *Electrochemistry Communications*, **9**, (3), 405-408, (2007)
13. C. M. Welch, M. E. Hyde, O. Nekrassova and R. G. Compton, *Physical Chemistry Chemical Physics*, **6**, (12), 3153-3159, (2004)
14. A. A. Tidblad and J. Martensson, *Electrochimica Acta*, **42**, (3), 389-398, (1997)
15. S. B. Faldini, S. M. L. Agostinho and H. C. Chagas, *Journal of Electroanalytical Chemistry*, **284**, (1), 173-183, (1990)
16. F. I. Danilov and V. S. Protsenko, *Russian Journal of Electrochemistry*, **34**, (3), 276-281, (1998)

17. G. Horanyi, *Journal of Solid State Electrochemistry*, **4**, (3), 153-158, (2000)
18. S. Farquharson, W. Smith and Y. Lee, *Journal of Process Analytical Chemistry*, **7**, (3), 85-91, (2002)
19. V. Brunetti, H. M. Villullas and M. Lopez Teijelo, *Electrochimica Acta*, **44**, (17), 2843-2851, (1999)
20. H. Feilchenfeld and O. Siiman, *Journal of Physical Chemistry*, **90**, (10), 2163-2168, (1986)
21. P. B. Dorain and J. L. Bates, *Langmuir*, **4**, (6), 1269-1273, (1988)
22. D. Sazou and G. Kokkinidis, *Journal of Electroanalytical Chemistry*, **271**, (1-2), 221-231, (1989)
23. L. Zhang, M. Kuhn and U. Diebold, *Surface Science*, **375**, (1), 1-12, (1997)
24. G. Lindbergh and D. Simonsson, *Electrochimica Acta*, **36**, (13), 1985-1994, (1991)
25. L. Xia and R. L. McCreery, *Journal of the Electrochemical Society*, **145**, (9), 3083-3089, (1998)
26. G. M. Brown, K. Shimizu, K. Kobayashi, G. E. Thompson and G. C. Wood, *Corrosion Science*, **33**, (9), 1371-1385, (1992)
27. D. Chidambaram, C. R. Clayton and G. P. Halada, *Journal of the Electrochemical Society*, **150**, (5), B224-B237, (2003)
28. W. R. McGovern, P. Schmutz, R. G. Buchheit and R. L. McCreery, *Journal of the Electrochemical Society*, **147**, (12), 4494-4501, (2000)
29. Szklarsk.Z and R. W. Staehle, *Journal of the Electrochemical Society*, **121**, (9), 1146-1152, (1974)
30. S. W. Jeon, J. L. Jambor, D. W. Blowes and R. W. Gillham, *Environ. Sci. Technol.*, **41**, (6), 1989-1994, (2007)
31. A. Cornell, G. Lindbergh and D. Simonsson, *Electrochimica Acta*, **37**, (10), 1873-1881, (1992)
32. J. He, V. J. Gelling, D. E. Tallman and G. P. Bierwagen, *Journal of the Electrochemical Society*, **147**, (10), 3661-3666, (2000)
33. M.-C. Tsai and P.-Y. Chen, *Talanta*, **76**, (3), 533-539, (2008)

34. P. A. Mosier-Boss and S. H. Lieberman, *Langmuir*, **19**, (17), 6826-6836, (2003)
35. D. Devilliers, M. T. Dinh Thi, E. Mahe and Q. Le Xuan, *Electrochimica Acta*, **48**, (28), 4301-4309, (2003)
36. S. Mustafa, A. Jamal, A. Naeem and N. Rehana, *Adsorption Science & Technology*, **19**, (9), 701-710, (2001)
37. F. Rodriguez-Valadez, C. Ortiz-Exiga, J. G. Ibanez, A. Alatorre-Ordaz and S. Gutierrez-Granados, *Environ. Sci. Technol.*, **39**, (6), 1875-1879, (2005)
38. C. M. Eggleston and W. Stumm, *Geochimica Et Cosmochimica Acta*, **57**, (19), 4843-4850, (1993)
39. V. Maurice, S. Cadot and P. Marcus, *Surface Science*, **471**, (1-3), 43-58, (2001)
40. J. E. Maslar, W. S. Hurst, W. J. Bowers, J. H. Hendricks, M. I. Aquino and I. Levin, *Applied Surface Science*, **180**, (1-2), 102-118, (2001)
41. A. L. Mifflin, K. A. Gerth and F. M. Geiger, *J. Phys. Chem. A*, **107**, (45), 9620-9627, (2003)
42. Y. Wang and K. Rajeshwar, *Journal of Electroanalytical Chemistry*, **425**, (1-2), 183-189, (1997)
43. V. A. Vicente and S. Bruckenstein, *Analytical Chemistry*, **45**, (12), 2036-2043, (1973)
44. A. J. Bard and L. R. Faulkner, *Electrochemical Methods Fundamentals and Applications*, Second ed, John Wiley and Sons, Inc.: Hoboken, (2001)
45. J. Birnie, C. Craggs, D. J. Gardiner and P. R. Graves, *Corrosion Science*, **33**, (1), 1-12, (1992)
46. P. Gao and M. J. Weaver, *J. Phys. Chem.*, **90**, (17), 4057-4063, (1986)
47. S. Venkatachalam and T. Jacob, *Zeitschrift Fur Physikalische Chemie-International Journal of Research in Physical Chemistry & Chemical Physics*, **221**, (9-10), 1393-1406, (2007)
48. P. Paredes Olivera, E. M. Patrito and H. Sellers, *Surface Science*, **418**, (2), 376-394, (1998)
49. M. J. Weaver, J. T. Hupp, F. Barz, J. G. Gordon II and M. R. Philpott, *Journal of Electroanalytical Chemistry*, **160**, (1-2), 321-333, (1984)
50. R. M. G. Michel, *Journal of Raman Spectroscopy*, **14**, (1), 22-27, (1983)

51. H. Stammreich, D. Bassi, O. Sala and H. Siebert, *Spectrochimica Acta*, **13**, (3), 192-196, (1958)
52. Y. He and E. Borguet, *The Journal of Physical Chemistry B*, **105**, (18), 3981-3986, (2001)
53. N. J. Tao and S. M. Lindsay, *Surface Science*, **274**, (2), L546-L553, (1992)
54. S. Ye, C. Ishibashi and K. Uosaki, *Langmuir*, **15**, (3), 807-812, (1999)
55. M. Baster, F. Bourée, A. Kowalska and Z. Latacz, *Journal of Alloys and Compounds*, **296**, (1-2), 1-5, (2000)
56. S. Vashchenko, L. Solodkova and Z. Solov'eva, *Russian Journal of Electrochemistry*, **36**, (9), 947-951, (2000)
57. H. Feilchenfeld and O. Siiman, *Journal of Physical Chemistry*, **90**, (19), 4590-4599, (1986)
58. C. Milton, D. E. Appleman, M. H. Appleman, E. C. Chao, F. Cuttitta, J. I. Dinnin, E. J. Dwornik, B. L. Ingram and H. J. Rose, Jr., *U.S. Geological Survey Professional Paper*, 887, (1976)
59. M. Ichikawa, T. Gustafsson, I. Olovsson and T. Tsuchida, *Journal of Physics and Chemistry of Solids*, **60**, (11), 1875-1880, (1999)
60. A. N. Christensen, P. Hansen and M. S. Lehmann, *Journal of Solid State Chemistry*, **21**, (4), 325-329, (1977)
61. A. Norlund Christensen, T. Johansson and S. Quezel, *Acta Chemica Scandinavica, Series A*, **28**, 1171-1174, (1975)
62. A. N. Christensen, P. Hansen and M. S. Lehmann, *Journal of Solid State Chemistry*, **19**, (3), 299-304, (1976)
63. W. H. Cloud, D. S. Schreiber and K. R. Babcock, *Journal of Applied Physics*, **33**, (3), 1193-1194, (1962)
64. R. Vidya, P. Ravindran, A. Kjekshus and H. Fjellvag, *Physical Review B (Condensed Matter and Materials Physics)*, **73**, (23), 235113-13, (2006)
65. R. M. Douglass, *Acta Crystallographica*, **10**, 423 - 427, (1957)
66. W. Scheld and R. Hoppe, *Zeitschrift fuer Anorganische und Allgemeine Chemie*, **568**, 151 -156, (1989)

Chapter 4. Influence of Aromatic Functionality on Quaternary Ammonium Levelers for Cu Plating

Reproduced with permission from Journal of the Electrochemical Society, 158, (6), D323-D329, 2011. Copyright 2011, The Electrochemical Society. This work was funded by the National Science Foundation. Partial support was also received from Novellus Systems Inc.

4.1. Introduction

The use of Cu as an interconnect materials for microelectronic circuitry is now firmly established.¹ The advantages of the Cu interconnect include low resistance, low electromigration, and amenability to dual damascene processing, relative to the traditional vacuum-deposited Al material.^{2, 3} The Cu is typically deposited electrochemically and this process has stimulated considerable interest in Cu electrodeposition generally, as well as applied to dual damascene processing. Cu is also used to make other interconnects in microelectronic circuitry, particularly through silicon vias (TSV) which connect the front side device to the back side. TSVs are proposed as a means to accomplish 3D packaging of microelectronic devices and offer higher connectivity and lower parasitic waste between chips.⁴⁴

Both dual damascene and TSV processing share similarities in that they both utilize Cu electrodeposition. In order to control the morphology of the deposit, organic and inorganic molecules are added into the plating baths. Indeed, the study of organic additives used in copper electrodeposition increased significantly over the last decade due to the increasing demands of the microelectronics industry.^{3, 5-7} These molecules have different functions and typically, these organic additives fall into one of three categories: Suppressors, Brighteners, and Levelers.⁸

Suppressors (also called carriers) are usually high molecular weight polyalkylene glycol type polymers which are added to reduce variations in the thickness of the Cu deposits.^{9, 10} Brighteners (sometimes referred to as accelerators) are usually molecules containing thiol, disulfide or sulfonic acid groups, and they are added to refine the grain structure of the Cu deposit.^{9, 10} Levelers are used to control overflow bumps during the copper deposition process.¹¹⁻¹³

One class of leveler compounds that has been used extensively in industry are quaternary ammonium salts. Initial studies of one such leveler, Janus Green B, showed its ability to suppress overflow on large feature arrays while allowing for proper fill within the interconnects.^{8, 14, 15} Amphiphilic quaternary ammonium surfactants such as dodecyltrimethyl ammonium chloride¹¹, cetyltrimethyl ammonium bromide¹⁶, and triethyl benzyl ammonium chloride¹⁷ can suppress the acceleration of copper deposition and are good candidates for leveling compounds.

Both dual damascene and TSV plating utilize some of the bath additives described above. However, the different Cu morphologies and differing amounts of material used in filling features dictates very different bath chemistries. In the case of dual damascene, bath additives including a halide, a suppressor, and an accelerator lead to the so-called “superfilling” or “superconformal” filling of features. In the case of TSV, however, bath additives typically include suppressors, brighteners, levelers, and a halide. Technology challenges for TSVs include handling of thinned wafers^{18, 18}, filling of larger features than damascene structures (typical diameter is 40 to 100 times larger than damascene structures)¹⁹, long deposition times²⁰, poor wetting of the via²¹, refreshing the solution in the via during Cu deposition.^{21, 22} New technology is needed as the microelectronics industry continues to shrink the size of interconnects and maintains high standards of defect free copper fill.

One of the most important bath constituents for TSV deposition is the leveler which helps to control overflow bumps above the feature. In order to develop new levelers for microelectronic applications which address technology limitations described above, a detailed understanding correlating molecular structure with function is required.

Because of this importance, levelers have been well-studied. Dow and Liu demonstrated convection-dependent adsorption of additives in the filling of high aspect ratio vias.^{22, 23} Lühn *et al.* determined that concentration gradient of leveler along the via profile is important for achieving complete fill.^{24, 24} Kim and coworkers showed that chain length of the leveler aliphatic tail and counter ion can influence the effectiveness of the suppression layer formed by the leveler.¹¹ Several studies examine methods to minimize defects in the Cu electrodeposit by varying electrodeposition pulse time, current density and additive concentrations.^{20, 25-29}

Although a large amount of work has been performed on studying the electrochemical and fill characteristics of the above levelers, relatively little has been done to understand the surface interaction needed to achieve the beneficial electrochemical characteristics. Bozzini *et al.* utilized SERS and voltammetry to study the behavior of Janus Green B in Cu electroplating baths and determined that orientation of Janus Green B on the surface was potential dependent.^{8,}
¹⁰ Using liquid chromatographic mass spectrometry, ¹H-NMR, impedance spectroscopy and molecular modeling, Li and coworkers concluded that Janus Green B undergoes reduction on the electrode surface, and the reduced species is actually responsible for the leveling properties observed.³⁰ Favry *et al.* used voltammetric techniques and secondary ion mass spectrometry to show the incorporation of organic impurities increased with plating time.³¹

While quaternary ammonium-containing surfactant molecules are very useful as levelers for Cu electrodeposition, different molecules behave differently. In order to elucidate and

correlate different molecular structures with leveler efficacy, we here study the electrochemistry and Surface Raman Scattering from different quaternary ammonium cation containing surfactants. These molecules, shown in Figure 4.1, are dodecyltrimethyl ammonium bromide (DTAB), benzyldimethylhexadecyl ammonium chloride (BDAC), and thonzonium bromide (ThonB).

4.2. Results

4.2.1. RDE Electroplating Measurements

Figure 4.2 shows slow scan rate voltammetry obtained from a Cu(poly) crystal immersed in a solution containing 10 g/L H_2SO_4 (0.1 M) + 40 g/L CuSO_4 (0.16 M) (pH 1 solution) and either 0, 10, 25 or 50 ppm of the three levelers considered here. The pH 1 experiments were performed at a scan rate of 10 mV/s. The crystal was rotated at 120 rpm.

Figure 4.2A shows voltammetry from (DTAB)-containing solutions at pH 1. Absent leveler, the voltammetry shows a strong cathodic feature commencing at 50 mV associated with the onset of bulk Cu deposition. Upon addition of 10 ppm DTAB, Cu deposition is inhibited until a potential of -150 mV is reached, at which point the rapidly increasing cathodic current shows that Cu deposition has commenced. As the scan progresses, a sudden change in the amount of current flowing is observed at -250 mV. The reverse scan exhibits substantial hysteresis and the cathodic current remains until a potential of 40 mV is reached. Hysteresis in deposition current is usually associated with inhibitor breakdown at negative potentials with reformation of the inhibitor layer only at diminished overpotentials.³²

Increasing the concentration of DTAB from 10 ppm to 50 ppm results in an increase in the onset potential to -180 mV. Additionally, increasing the DTAB concentration also results in

a decrease in the hysteresis observed between the cathodic and anodic potential sweeps so that at 50 ppm DTAB, relatively little hysteresis remains.

At positive potentials, voltammetry obtained absent DTAB shows substantial current associated with oxidation of the Cu surface. However, addition of DTAB substantially suppresses this oxidation, indicating that DTAB is adsorbed on the surface at these potentials.

Figure 4.2B shows the voltammetry from Cu(poly) in a BDAC-containing solution at pH = 1. In the presence of 10 ppm BDAC the onset of bulk Cu deposition undergoes a cathodic shift to -210 mV from $+50$ mV. In the anodic region of the voltammogram, the current density is suppressed compared to the same region in the blank voltammogram, as was the case with DTAB. During the cathodic scan, there is a large hysteresis.

At a concentration of 25 ppm BDAC, bulk Cu deposition is suppressed until -260 mV. There is a slight cathodic current which starts at -210 mV prior to the onset of the bulk deposition process. As the concentration of BDAC is increased to 50 ppm there is again a cathodic shift in the onset of bulk deposition to -280 mV. Again there is slight cathodic current which starts at -210 mV similar to the 25 ppm situation. The voltammograms show a decrease in the amount of hysteresis in the cathodic region with increasing leveler concentration. The origin of this decrease must be more facile formation of a barrier layer at higher additive concentrations after breakdown during bulk Cu deposition.³²

Figure 4.2C displays the voltammetry of a Cu(poly) disk in a solution containing TB at pH = 1. In the TB case, the onset of bulk Cu plating occurs at more cathodic potentials than is observed with either DTAB or BDAC, between -380 mV and -400 mV.

Interestingly, the onset potential for Cu deposition is independent of [ThonB] for the concentrations used here. However, the degree of hysteresis is [ThonB] dependent with higher

concentrations showing less hysteretic behavior. In particular, the cathodic current of the return scan reaches zero at 70 mV, -30 mV, and -100 mV for the 10 ppm, 25 ppm and 50 ppm systems respectively. The change in the hysteresis behavior with concentration is associated with the rate of reformation of the suppression layer formed initially by the Thon⁺ material on the Cu surface.^{32, 33} Higher concentrations of ThonB enable faster reformation of the suppression layer as the potential sweep direction is reversed.

Increasing the concentration of ThonB in solution does not significantly change the onset of bulk Cu deposition indicating that saturated inhibition has been reached. However, the reformation of the suppressive layer varies according to the concentration of ThonB as indicated by the shift in the hysteresis of the voltammograms.

4.2.2. SERS Measurements

SERS data were obtained for each of the additive components studied above. Peaks observed in the SERS spectra are listed in Tables 1, 2, and 3 for each of the three additives. Assignments were made based on calculations performed by using Spartan 08. We have previously shown good correspondence between calculated and experimental vibrational modes for organic molecules using this program.^{34, 35}

Figure 4.3 shows the SERS obtained from a roughened Cu(poly) disk immersed in a 0.1 M H₂SO₄ solution containing 10 ppm of each of the three levelers. Each set of spectra display the evolution of peak intensities as the potential is scanned cathodically.

4.2.2.1. DTAB

Figure 4.3A shows SERS spectra of a Cu(poly) disk immersed in a solution of 10 ppm DTAB at pH 1 obtained at different potentials. Throughout the course of the cathodic sweep there are four main peaks A, B, C, and D observed in the spectrum. Peak A, at 760 cm⁻¹, is

likely associated with methylene hydrogen atom rotation on the aliphatic chain. Peak B, at 980 cm^{-1} , is assigned to the sulfate (supporting electrolyte) symmetric stretch.^{36, 37} DTA^+ does exhibit a band at 997 cm^{-1} , assigned a combined asymmetric stretching mode of the quaternary nitrogen and a rotation/torsion mode of the methylene chain; however the energy of this mode is too far away from Peak B to be assigned as such. Peak C, at 1048 cm^{-1} , is associated with the C–C asymmetric stretch of the methylene chain. We note that this peak is close to the 1052 cm^{-1} mode of HSO_4^- and another mode associated with DTA^+ also observed at 1052 cm^{-1} in the normal Raman obtained from neat DTAB powder. In the SERS, Peak C may be a combination of all of these. Peak D, at 1440 cm^{-1} , is associated with the asymmetric stretch mode of the quaternary nitrogen. Interestingly, the features found in the SERS spectrum appear to be potential independent. No shifts in the energies of the peaks are found between 0 and -800 mV . Additionally, peak intensities change by at most 30 % over the potential range interrogated. The lack of change between spectra suggests that both the DTA^+ orientation and surface concentration are potential independent.

4.2.2.2. BDAC

Figure 4.3B shows a series of SERS spectra obtained from a Cu(poly) disk immersed in a pH 1 solution containing 10 ppm BDAC at different potentials. The spectra were obtained during the cathodic sweep. A large number of peaks are observed, as shown in Table 2, and both the identity and intensity of these peaks is potential dependent.

Initially, at 0 mV, the SERS is relatively sparse. Peaks B, C, O, and P are associated with modes involving the benzyl ring and quaternary nitrogen. Peak Q, at 986 cm^{-1} , is likely the sulfate symmetric stretch as noted before, though slightly shifted to higher energy. This may be due to ion pairing of the BDA^+ cation and the sulfate anion; similar behavior was observed by

Hope *et al.* while studying adsorption of thiourea on a Cu(poly) surface.³⁸ Peak J is a combination mode consisting of asymmetric stretching and hydrogen rotation/torsion on the alkane chain. Peak K is associated with an asymmetric C – C stretching of the chain with some contribution from rotation of the benzyl methylene spacer. The pzc of Cu(poly) is more negative than –100 mV vs. Ag/AgCl³⁹ implying that spectra obtained at 0 mV are obtained at potentials positive of the pzc. Nonetheless, the spectra suggest that the cationic BDA⁺ molecule is still surface associated. The presence of a cation at the surface at potentials positive of the pzc is not unprecedented and has been explained as a consequence of ion pairing.³⁹⁻⁴¹

As the potential of the surface is scanned cathodically new peaks emerge, and all of the peaks grow in intensity, as expected. Most noticeably, a peak at 542 cm⁻¹ (peak A) grows in at –200 mV. Peak A is combined ring deformation mode of the benzyl ring and scissoring of the quaternary nitrogen substituents. Additionally, a large shoulder grows in at energies just lower than that of peak J and is a combination of peaks Q, H, and I. Peak L becomes the shoulder of peak K.

At –400 mV SERS peaks reach highest intensity indicating the maximal association of BDA⁺ with the Cu surface. Also, at this potential, peak N – an in plane scissoring of the benzyl hydrogen atoms coupled with methylene chain rotation and asymmetric stretching of the quaternary nitrogen bonds – begins to emerge at 1443 cm⁻¹.

At –600 mV all of the peaks have diminished in intensity except for peaks H and N. The presence of these peaks and lack intensity of the others indicates a possible change in orientation of BDA⁺ at the surface, with the alkane chain interacting with the surface more than the positively charged head group.

At -800 mV peak N reaches its maximal intensity and peak H has begun to diminish. At this potential it is clear that BDA^+ is weakly associated with the surface because of the lack of substantial peak intensity associated with vibrational modes of the molecule.

Overall, the data indicates that as the potential is scanned in the cathodic direction, BDA^+ becomes more strongly associated with the surface achieving its strongest interaction at circa -400 mV; as the potential continues cathodically, the leveler becomes more weakly tied to the surface.

4.2.2.3. ThonB

Figure 4.3C shows the SERS spectra of Cu(poly) disk immersed in a 10 ppm ThonB containing solution at $\text{pH} = 1$. The spectra were obtained while the potential was swept cathodically. Several changes in the spectra occur over the course of the potential sweep.

At 0 mV, peaks O, S, T, and D are associated with quaternary nitrogen and amino nitrogen normal modes as shown in Table 3. As the potential is swept cathodically, these peaks increase in intensity indicating close proximity to the surface. The maximal intensity of these peaks occurs at -400 mV and the intensity rapidly diminishes between -400 mV and -500 mV. Interestingly, this potential coincides with the onset of bulk Cu deposition observed in the slow scan voltammetry. Likewise, peak Q, at 1355 cm^{-1} , which is assigned to the methoxy group, behaves similarly.

Peak B is a combination of two overlapping peaks which has an apparent shift in position from 633 cm^{-1} to 627 cm^{-1} . The assignment of peak B is a combination of the vibrational modes associated with the two individual peaks (627 cm^{-1} and 633 cm^{-1}), and is assigned to scissoring of the amino nitrogen and in plane pyrimidyl ring stretching mode, respectively. As the potential is made more negative, the 627 cm^{-1} transition dominates, possibly indicating that the

pyrimidyl ring is approaching the surface. Peak N – associated with the asymmetric stretch of the quaternary nitrogen, scissoring of the benzyl ring hydrogen atoms and chain rotation/torsion – also grows in as the potential is swept to more negative values, becoming observable at a potential of -600 mV. The growth of peak N correlates with the shift of peak B, suggesting that the amino nitrogen – close to the pyrimidyl ring – is more closely associated with the surface at negative potentials.

Several peaks are associated with methylene chain vibrations. Some of these – such as peaks M, P, and R – are not influenced by changing the potential. Others, such as peaks K, F, and I, are potential dependent, and disappear at potentials negative of -400 mV. One methylene chain associated vibration, Peak H, at 978 cm^{-1} , is assigned to the C – C symmetric stretch of the terminal carbon atoms on the methylene chain. This peak grows in at -400 mV as a shoulder on peak G. The appearance of peak H and the disappearance of the potential dependent chain peaks (peaks K, F, and I) indicates a probable shift in the orientation of Thon^+ on the surface.

4.3. Discussion

In order to understand the behavior of these cationic surfactants and their interaction with the Cu surface, it is important to know the potential of zero charge (pzc) for Cu. It is anticipated that anionic species will dominate behavior at potentials positive of the pzc, while cations will dominate at negative potentials.

The pzc is usually identified with the minimum in the double-layer capacitance. Using this method, Lukomska and Sobkowski measured the pzc of Cu in ClO_4^- and showed that the pzc shifted from -930 mV vs. Ag/AgCl at pH = 5.7 to -750 mV vs. Ag/AgCl at pH = 3.2.⁴² Extrapolation of this data leads to an estimated pzc of ca. $+100$ mV vs. Ag/AgCl at pH = 1. Ma *et al.* studied the corrosion inhibition properties of cetyltrimethyl ammonium bromide (CTAB)

on Cu in H₂SO₄ solutions. They observed that the pzc of copper in 0.5 M H₂SO₄ was ca. -100 mV vs. Ag/AgCl.³⁹ We note that the pzc can be strongly influenced by the presence of surface oxides and the specific adsorption of ionic species.^{43,44} For example, specific adsorption of anions has the effect of shifting the pzc to more cathodic potentials.^{44,45} In addition to the nature of the specifically adsorbing species, the concentration of the ionic species in solution also causes the pzc to shift (Esin-Markov effect).⁴⁶

In order to address the pzc question directly, we performed differential capacity measurements for each of the additive systems studied here. The differential capacity (Appendix D) showed a broad plateau where the capacity is low and flat. This behavior is similar to that described for the adsorption of other surfactants to electrode surfaces.⁴⁷ Our measurements indicate that the pzc of Cu is in the range of -100 mV to -300 mV vs. Ag/AgCl, -130 mV to -160 mV vs. Ag/AgCl, and -100 mV to -350 mV vs. Ag/AgCl for each of the leveler systems, DTAB, BDAC, and ThonB respectively. These data, and those referenced above suggest that the pzc is for Cu with these surfactants substantially more positive than the -450 mV and -800 mV vs. Ag/AgCl estimated by Trassati.^{48,48}

4.3.1. DTAB

Electrochemical measurements show that the different additives have different hysteresis, breakdown, and concentration dependence properties. In the case of DTAB, plating curves show that at high concentrations little hysteresis is seen. The gradual onset of bulk Cu deposition indicates that the suppression barrier formed by DTA⁺ does not quickly leave the surface compared to either BDA⁺ or Thon⁺. At lower concentrations, some hysteresis is observed, suggesting that full coverage of the Cu surface is not obtained. The relatively positive onset potentials (ca. -0.3 V) for DTAB suggest that this additive does a poor job inhibiting bulk Cu

deposition. The lack of hysteresis suggests that the molecule continues to be present after bulk deposition has started.

Correspondingly, DTA^+ exhibits no potential-dependent behavior in the SERS. Band intensities and positions are relatively constant throughout the potential region interrogated in this study, again suggesting that DTA^+ association with the Cu surface is relatively potential independent. This behavior is not anticipated, since the cationic DTA^+ should more strongly associate with the Cu surface at potentials negative of the pzc.

There are several possible reasons that DTA^+ association with Cu could be relatively potential independent. First, it is known that uncharged organic molecules to lower the surface tension at the electrode-solution interface and thus persist at this interface over a wide range of potentials.⁴⁷ DTA^+ may behave similarly. Second, the halide may affect DTA^+ behavior. Br^- adsorbs to Cu surfaces more strongly than Cl^- .^{49, 50} The persistence of the halide anion in this case at negative potentials may affect the ability of DTA^+ to interact with the surface. Third, ion pairing of the DTA^+ with sulfate or bisulfate could produce a more stable film.^{38, 51, 52}

Finally, we suggest that the DTA^+ may form a hemimicellar or premicellar structure on the Cu electrode surface, as has been seen for other cationic surfactants on Au.⁵³ The critical micellar concentration (cmc) for DTA^+ is ~12 mM which is two orders of magnitude larger than the 100 μM concentration used here. However, the formation of surface aggregates occurs at concentrations – the critical surface aggregate concentration (cac) – well below the cmc. Theory predicts that the cac is some three orders of magnitude lower than the cmc.⁵⁴ Experimentally, ordered adlayers of *N*-decyl-*N,N,N*-trimethylammonium triflate (DeTATf) were observed on a Au (111) surface at $[\text{DeTA}^+] = 280 \mu\text{M}$; the cmc for this cation is between 0.40 mM and 80 mM

dependent on solution conditions.^{55, 56} Studies show that the degree of stabilization of cationic surfactants depends on many factors, including the temperature, the anion, and the surface.^{53-55, 57}

Based on this precedent, we suggest that ordered adlayer formation may stabilize the DTA^+ cation on the Cu electrode surface, accounting for the lack of potential dependence in either the SERS or, apparently, the plating data, over the potential range examined.

4.3.2. BDAC

In contrast to the DTAB case, the plating voltammetry for BDAC exhibits substantial [BDAC] dependence. Higher concentrations of this molecule yield higher Cu plating onset potential. Hysteresis in the plating voltammetry shows that once plating is initiated, the suppression barrier quickly leaves the surface and does not reform until positive potentials are restored.

SERS data support this behavior. The maximum in SERS signals for both cationic modes and alkane chain modes of BDA^+ are achieved at ca. -400 mV on the cathodic sweep and then the signal decreases substantially. Changes in band intensities and the growth of peak N could be associated with the alkane chain of the molecule becoming closer to the surface (and more enhanced), prior to decrease in signal showing that molecule is leaving the surface.

The observed differences in behavior between BDA^+ and DTA^+ are at first blush unexpected. On the one hand, the longer chain of BDA^+ is expected to make the molecule adsorb more strongly to the surface^{58, 59} which would suggest that the BDA^+ molecule should persist at more negative potentials, in contrast to what is observed. On the other hand, the phenyl ring moiety of the BDA^+ molecule might hinder the approach of the quaternary nitrogen to the surface, thus weakening its surface association. The phenyl ring moiety could also inhibit the formation of micellar structures on the Cu surface. Interestingly, the cmc for BDAC is

660 mM⁶⁰, which is substantially higher than that for DTAB. The higher cmc suggests that stabilization of BDAC on the Cu surface through the agency of pre/hemimicelle formation is inhibited relative to DTAB. Additionally, Cl⁻ binds less strongly to the surface than Br⁻. The coadsorption of Br⁻ with DTA⁺ should provide a more stable film than would be expected for the coadsorption of Cl⁻ with DTA⁺.^{49, 52, 61} At the same time, we note that the behavior of BDAC has much more in common with ThonB, described below, than with DTAB, suggesting that the anion is not the only factor controlling the strength of the cation adsorption to the Cu surface.

Interestingly, the onset of Cu deposition for DTAB occurs at more positive potentials than for BDAC which would indicate that the suppression barrier formed by DTA⁺ is not as stable as the one for BDA⁺. DTA⁺ continues to inhibit plating after bulk deposition of Cu has begun; in contrast, BDA⁺ leaves the surface abruptly when bulk Cu deposition starts.

4.3.3. *ThonB*

A third behavior is observed with ThonB. The onset potential of bulk Cu deposition exhibits essentially no [ThonB] dependence. This result suggests that the surface is saturated at the [ThonB] used here. However, we note that plating voltammetry for the 50 ppm ThonB case exhibits less positive suppression than lower ThonB concentrations. Also, potentials for breakdown are much more negative, relative to BDA⁺ (ca. 100 mV). SERS shows that Thon⁺ is present on the surface during the start of the cathodic sweep. However, SERS is potential dependent showing changes in molecular structure or association with surface as the potential is made more negative. It seems likely that the onset of plating occurs when the quaternary and amino nitrogen groups leave the surface. This inference is supported by the sudden decrease in peak intensity of those substituents, between -400 mV and -500 mV, and the onset of bulk Cu deposition observed in the slow scan voltammetry.

We suggest that the ThonB molecule adsorbs strongly to the Cu surface due to the presence of both the cationic quaternary and amine nitrogen groups in the molecule. As the potential becomes more negative, the molecule likely reorients and pyrimidyl nitrogen group is now seen in SERS. The cmc of ThonB is has not been reported, however, it is expected that the cmc is higher than the other two levelers due to the increased dimensions of the hydrophilic head group.⁶² The likely increased cmc of ThonB again suggests that stabilization of this molecule via hemi or pre-micellization on the Cu surface is unlikely.

In conclusion, three different behaviors are observed with three different cations used as levelers in Cu electroplating. For all three, association of the cationic surfactant with the Cu surface inhibits the onset of bulk Cu deposition. The inhibitive effect of the leveler depends on the degree of cation association with the Cu surface. In the simplest case, the cationic surfactant is always adsorbed. In more complicated cases, other parts of the molecule and counter ions moderate the cationic interaction with the surface, allowing the molecule either to desorb or to change its orientation, diminishing the ability of the molecule to screen the surface from Cu plating.

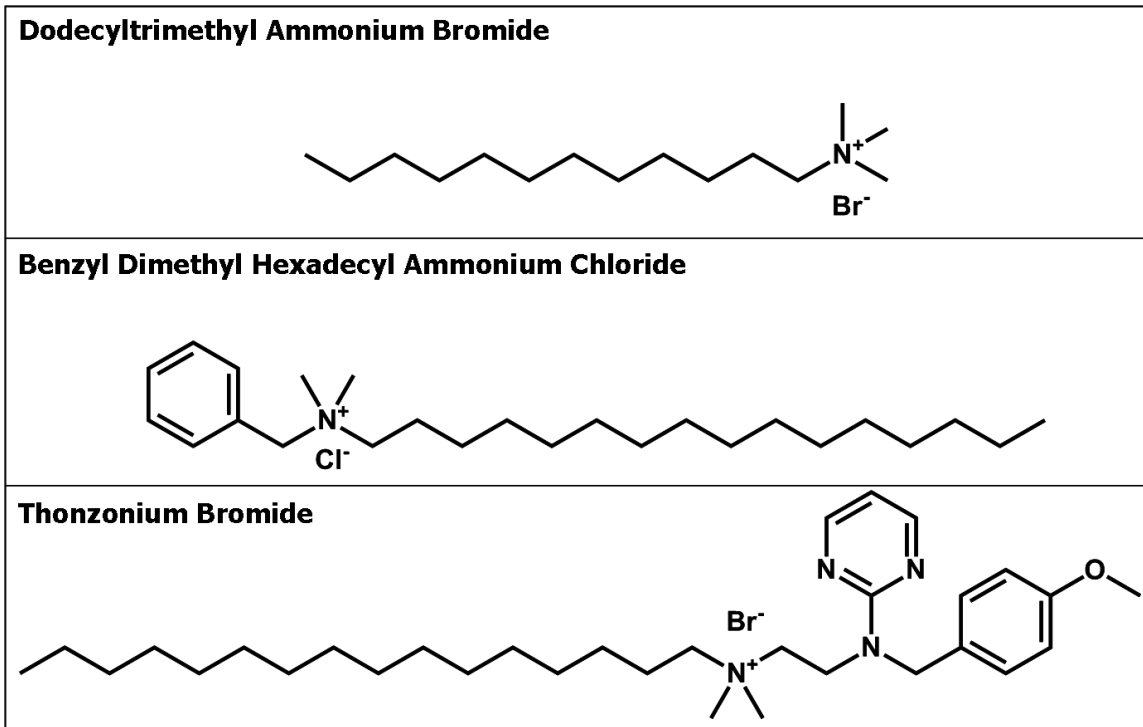


Figure 4.1: Molecular structures of each of the amphiphilic surfactants used in this study.

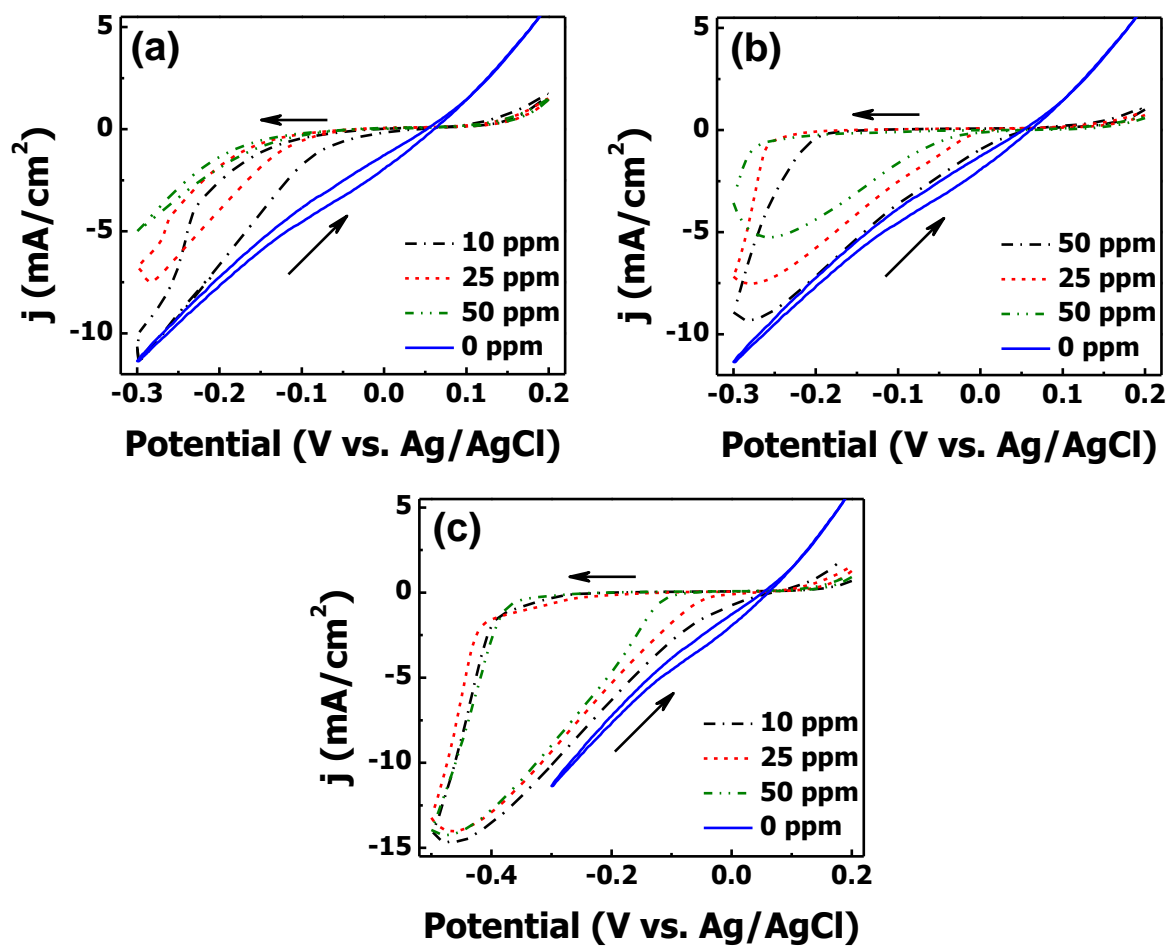


Figure 4.2: The effect of variation of leveler concentration on the onset of Cu deposition on a Cu(poly) electrode rotated at 120 rpm and a potential scan rate of 10 mV/s. The electrolyte was composed of 10 g/L H₂SO₄ (0.1 M) + 40 g/L CuSO₄ (0.16 M) and 0, 10, 25 or 50 ppm of (a) DTAB, (b) BDAC, or (c) ThonB.

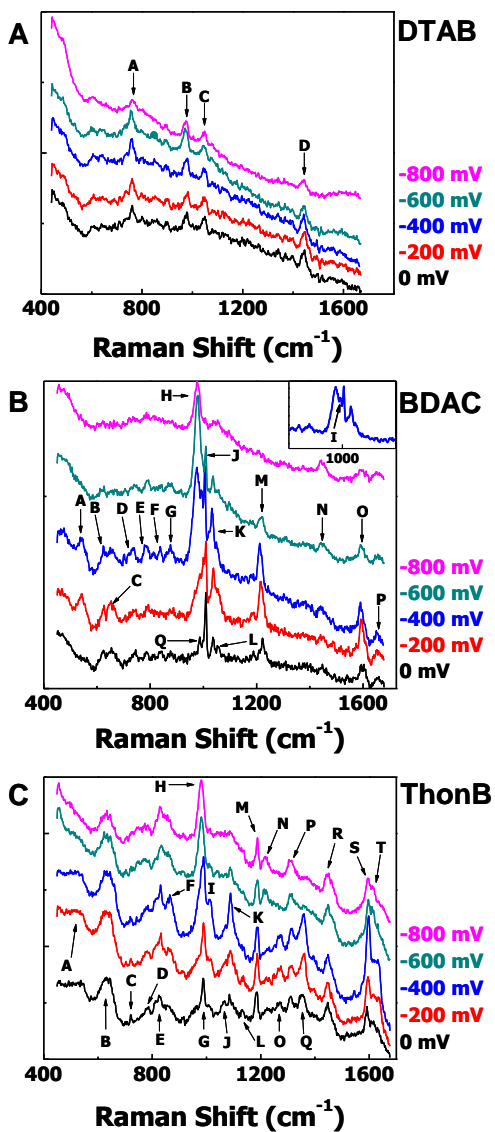


Figure 4.3: SERS data obtained during the cathodic scan of a roughened Cu(poly) disk immersed in a 0.1 M H₂SO₄ solution containing 10 ppm of (a) DTAB, (b) BDAC, or (c) ThonB.

Table 4.1: SERS peak assignments for DTAB

Peak	Calculation (cm⁻¹)	Observed (cm⁻¹)	Assignment
A	789	762	Methylene chain rotation
B	N/A	980	Sulfate symmetric stretch ^{42,43}
C	1052	1048	Combined C – C asymmetric stretch and HSO ₄ ⁻ asymmetric stretch ⁴²
D	1444	1443	Combined N – (CH _x) asymmetric stretch and chain C – H wagging

Table 4.2: SERS peak assignments for BDAC

Peak	Calculation (cm ⁻¹)	Observed (cm ⁻¹)	Assignment
A	545	542	Benzyl ring deformation
B	604	620	Benzyl ring out of plane bend
C	689	652	Benzyl ring in plane bend
D	710	745	Benzyl ring in plane bend
E	781	785	Combined benzyl ring deformation + N – (CH _x) breathing mode
F	835	840	Combined benzyl ring deformation + N – (CH _x) breathing mode
G	881	880	Combined benzyl ring out of plane bend + N – (CH _x) asymmetric stretch
H	979	979	Chain (C – C) asymmetric stretch
I	991	996	Combined Chain (C – C) asymmetric stretch + chain (C – H) rotation/torsion
J	1013	1009	Combined Chain (C – C) asymmetric stretch + chain (C – H) rotation/torsion
K	1035	1036	Chain (C – C) asymmetric stretch
L	1055	1054	Methylene spacer (C – H) rotation
M	1221	1220	Combined benzyl in plane bend + N (C – H) rotation + chain (C – H) torsion
N	1440	1443	Combined benzyl – H in plane scissoring + N – (CH _x) asymmetric stretch + chain (C – H) rotation/torsion
O	1591	1590	Combined methylene spacer (C – H) wagging + (H – C – H) scissoring on N
P	1656	1651	N – (CH _x) scissoring

Table 4.3: SERS peak assignments for ThonB

Peak	Calculation (cm ⁻¹)	Observed (cm ⁻¹)	Assignment
A	518	526	Benzyl ring deformation
B	614 and 635	627 and 633	N _{amino} – (CH ₂) scissoring/pyrimidyl ring in plane stretch
C	725	721	Combined pyrimidyl ring/benzyl ring in plane deformation
D	785	782	N _{quat} – (CH _x) symmetric stretch
E	798	825	Benzyl ring in plane stretch
F	854	852	Chain (C – H) wagging
G	981	988 to 986	Sulfate symmetric stretch
H	979	978	Chain terminal (C – C – C) symmetric stretch
I	1006	1007	Chain (C – H) rotation/torsion
J	1060	1065	Combined pyrimidyl ring deformation + benzyl methylene (C – H) rotation
K	1073	1084	Chain (C – C) asymmetric stretch
L	1130	1131	Chain (C – C) asymmetric stretch
M	1180	1183	Chain (C – H) wagging
N	1215	1215	Pyrimidyl ring out of plane deformation
O	1273	1270	N – (CH ₃) rocking
P	1309	1310	(C _{chain} – H) wagging nearest N _{quat}
Q	1347	1355	Methoxy (CH ₃) rocking
R	1440	1447 to 1442	Chain (C – H) wagging
S	1588	1591	N _{amino} – (CH ₂) symmetric stretch
T	1620	1620	N _{quat} methyl (C – H) scissoring

4.4. References

1. T. Ritzdorf, *ECS Transactions*, **6**, (8), 1-11, (2007)
2. P. C. Andricacos, *Electrochemical Society Interface*, **8**, (1), 32, (1999)
3. P. C. Andricacos, C. Uzoh, J. O. Dukovic, J. Horkans and H. Deligianni, *Ibm Journal of Research and Development*, **42**, (5), 567-574, (1998)
4. M. Facchini, T. Carlson, A. Vignon, M. Palkovic, F. Catthoor, W. Dehaene, L. Benini and P. Marchal, Design, Automation & Test in Europe Conference & Exhibition. 923-928. 2009
5. M. J. Willey and A. C. West, *Journal of The Electrochemical Society*, **154**, (3), D156-D162, (2007)
6. J. J. Kim, S.-K. Kim and Y. S. Kim, *Journal of Electroanalytical Chemistry*, **542**, 61-66, (2003)
7. D. Stoychev and C. Tsvetanov, *Journal of Applied Electrochemistry*, **26**, (7), 741-749, (1996)
8. B. Bozzini, C. Mele, L. D'Urzo and V. Romanello, *Journal of Applied Electrochemistry*, **36**, (9), 973-981, (2006)
9. J. W. Dini, *Modern Electroplating*, Fourth Edition ed, John Wiley & Sons, Inc.: (2000)
10. B. Bozzini, C. Mele, L. D'Urzo, V. Romanello and G. Giovannelli, *Transactions of the Institute of Metal Finishing*, **84**, (4), 177-187, (2006)
11. S.-K. Kim, D. Josell and T. P. Moffat, *Journal of The Electrochemical Society*, **153**, (12), C826-C833, (2006)
12. T. P. Moffat, D. Wheeler, S. K. Kim and D. Josell, *Journal of The Electrochemical Society*, **153**, (2), C127-C132, (2006)
13. M. Hasegawa, Y. Negishi, T. Nakanishi and T. Osaka, *Journal of The Electrochemical Society*, **152**, (4), C221-C228, (2005)
14. J. J. Kelly and A. C. West, *Electrochemical and Solid-State Letters*, **2**, (11), 561-563, (1999)
15. J. J. Kelly, C. Tian and A. C. West, *Journal of The Electrochemical Society*, **146**, (7), 2540-2545, (1999)

16. E. D. Eliadis and R. C. Alkire, *Journal of The Electrochemical Society*, **145**, (4), 1218-1226, (1998)
17. S. Varvara, L. Muresan, I. C. Popescu and G. Maurin, *Journal of Applied Electrochemistry*, **35**, (1), 69-76, (2005)
18. S. Q. Gu, U. Ray, Y. Li, A. Chandrasekaran, B. Henderson and M. Nowak, Interconnect Technology Conference (IITC), 2010 International. 1-3. 2010
19. O. Lühn, C. Van Hoof, W. Ruythooren and J. P. Celis, *Electrochimica Acta*, **54**, (9), 2504-2508, (2009)
20. K. Kondo, T. Yonezawa, D. Mikami, T. Okubo, Y. Taguchi, K. Takahashi and D. P. Barkey, *Journal of The Electrochemical Society*, **152**, (11), H173-H177, (2005)
21. P. Dixit, X. Chen, J. Miao, S. Divakaran and R. Preisser, *Applied Surface Science*, **253**, (21), 8637-8646, (2007)
22. W.-P. Dow and C.-W. Liu, *Journal of The Electrochemical Society*, **153**, (3), C190-C194, (2006)
23. W.-P. Dow, M.-Y. Yen, S.-Z. Liao, Y.-D. Chiu and H.-C. Huang, *Electrochimica Acta*, **53**, (28), 8228-8237, (2008)
24. O. Lühn, J. P. Celis, C. Van Hoof, K. Baert and W. Ruythooren, ECS Transactions. 123-133. 2007
25. P. Dixit and J. Miao, *Journal of The Electrochemical Society*, **153**, (6), G552-G559, (2006)
26. T. Haba, H. Suzuki, H. Yoshida, H. Akahoshi and A. Chinda, *Electrochemical and Solid-State Letters*, **13**, (5), D23-D25, (2010)
27. W.-P. Dow, C.-C. Li, M.-W. Lin, G.-W. Su and C.-C. Huang, *Journal of The Electrochemical Society*, **156**, (8), D314-D320, (2009)
28. M. Hayase and M. Nagao, *Journal of The Electrochemical Society*, **156**, (6), D198-D203, (2009)
29. S. C. Chang, J. M. Shieh, B. T. Dai and M. S. Feng, *Journal of Vacuum Science & Technology B*, **20**, (6), 2295-2298, (2002)
30. Y.-B. Li, W. Wang and Y.-L. Li, *Journal of The Electrochemical Society*, **156**, (4), D119-D124, (2009)

31. É. Favry, N. Frederich, A. Meunier, L. Omnès, F. Jomard and A. Etcheberry, *Electrochimica Acta*, **53**, (23), 7004-7011, (2008)
32. M. E. H. Garrido and M. D. Pritzker, *Journal of The Electrochemical Society*, **156**, (5), D175-D183, (2009)
33. B. H. Wu, C. C. Wan and Y. Y. Wang, *Journal of Applied Electrochemistry*, **33**, (9), 823-830, (2003)
34. Z. V. Feng, X. Li and A. A. Gewirth, *The Journal of Physical Chemistry B*, **107**, (35), 9415-9423, (2003)
35. T. Y. Zakharian and S. R. Coon, *Computers & Chemistry*, **25**, (2), 135-144, (2001)
36. G. Niaura and A. Malinauskas, *Journal of the Chemical Society, Faraday Transactions*, **94**, (15), 2205-2211, (1998)
37. G. A. Hope and R. Woods, *Journal of The Electrochemical Society*, **151**, (9), C550-C553, (2004)
38. G. M. Brown and G. A. Hope, *Journal of Electroanalytical Chemistry*, **413**, (1-2), 153-160, (1996)
39. H. Ma, S. Chen, B. Yin, S. Zhao and X. Liu, *Corrosion Science*, **45**, (5), 867-882, (2003)
40. J. O. M. Bockris and A. K. N. Reddy, *Modern Electrochemistry*, 'Vol.' 2, p 708 Plenum Publishing Corporation: New York, (1970)
41. G. J. Edens, X. Gao and M. J. Weaver, *Journal of Electroanalytical Chemistry*, **375**, (1-2), 357-366, (1994)
42. A. Lukomska and J. Sobkowski, *Journal of Electroanalytical Chemistry*, **567**, (1), 95-102, (2004)
43. G. J. Clark, T. N. Andersen, R. S. Valentine and H. Eyring, *Journal of The Electrochemical Society*, **121**, (5), 618-622, (1974)
44. G. Niaura, A. K. Gaigalas and V. L. Vilker, *The Journal of Physical Chemistry B*, **101**, (45), 9250-9262, (1997)
45. A. J. Bard and L. R. Faulkner, *Electrochemical Methods Fundamentals and Applications*, Second ed, John Wiley and Sons, Inc.: Hoboken, (2001)
46. D. C. Grahame, *Chemical Reviews*, **41**, (3), 441-501, (1947)
47. C. Buess-Herman, *Progress in Surface Science*, **46**, (4), 335-375, (1994)

48. S. Trasatti, *Electrified Interfaces in Physics, Chemistry and Biology*, p 245, , Kluwer Academic Publishers: Dordrecht, (1992)
49. V. Marichev, *Protection of Metals and Physical Chemistry of Surfaces*, **45**, (3), 241-276, (2009)
50. L.-J. Wan and K. Itaya, *Journal of Electroanalytical Chemistry*, **473**, (1-2), 10-18, (1999)
51. C. Buess-Herman, *Journal of Electroanalytical Chemistry*, **349**, (1-2), 93-111, (1993)
52. M. Skompska and K. Jaszczynski, *Journal of Electroanalytical Chemistry*, **291**, (1-2), 217-225, (1990)
53. M. Jaschke, H. J. Butt, H. E. Gaub and S. Manne, *Langmuir*, **13**, (6), 1381-1384, (1997)
54. R. A. Johnson and R. Nagarajan, *Colloids and Surfaces A: Physicochemical and Engineering Aspects*, **167**, (1-2), 31-46, (2000)
55. M. Chen, I. Burgess and J. Lipkowski, *Surface Science*, **603**, (10-12), 1878-1891, (2009)
56. C. L. Brosseau, E. Sheepwash, I. J. Burgess, E. Cholewa, S. G. Roscoe and J. Lipkowski, *Langmuir*, **23**, (4), 1784-1791, (2006)
57. H. C. Schniepp, D. A. Saville and I. A. Aksay, *Langmuir*, **24**, (3), 626-631, (2008)
58. A. V. Teplyakov, A. B. Gurevich, M. X. Yang, B. E. Bent and J. G. Chen, *Surface Science*, **396**, (1-3), 340-348, (1998)
59. B. A. Sexton and A. E. Hughes, *Surface Science*, **140**, (1), 227-248, (1984)
60. A. Raducan, A. Olteanu, M. Puiu and D. Oancea, *Central European Journal of Chemistry*, **6**, (1), 89-92, (2008)
61. J. Lipkowski, Z. Shi, A. Chen, B. Pettinger and C. Bilger, *Electrochimica Acta*, **43**, (19-20), 2875-2888, (1998)
62. S. K. Samanta, S. Bhattacharya and P. K. Maiti, *The Journal of Physical Chemistry B*, **113**, (41), 13545-13550, (2009)

Appendix A. Corrosion of 316L Stainless Steel, Haynes Alloy 230, and Haynes Alloy 617

Buyang Cao and David Gross are gratefully acknowledged for their assistance in obtaining SEM images of the Haynes Alloys. The Department of Energy provided financial support for this work.

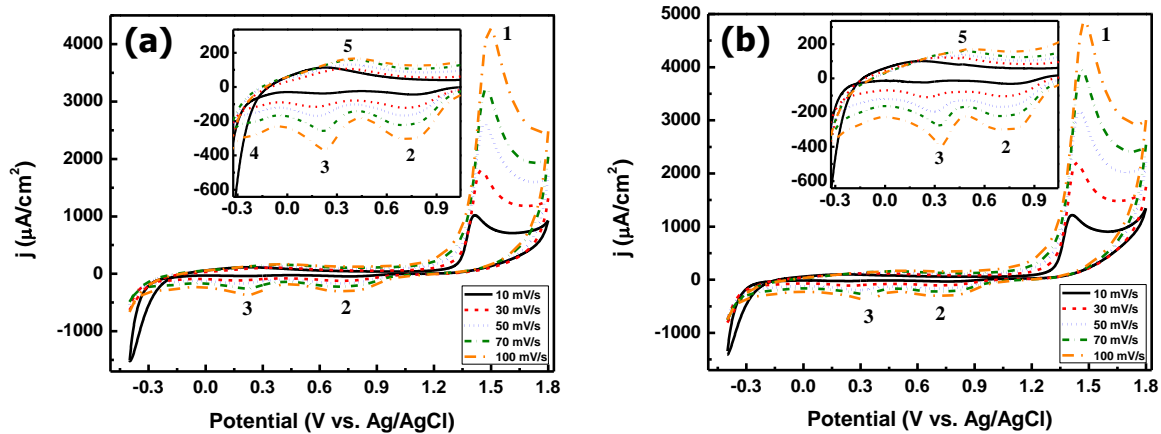
All samples were prepared for experiments as described in the experimental chapter.

Stainless Steel 316L

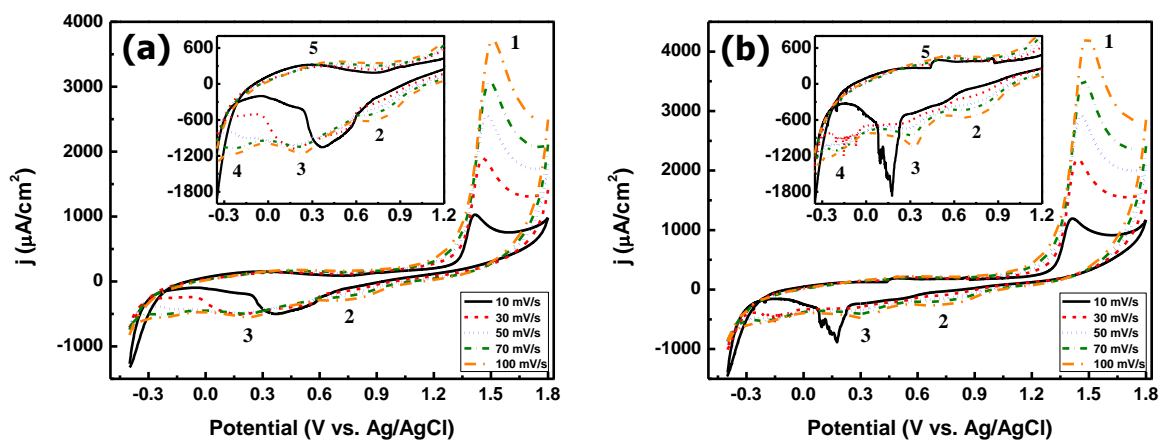
Single crystalline (with respect to the fcc Fe matrix) 316L stainless steel samples were acquired from Professor Hisham Hussein in the Material Science and Engineering department at the University of Illinois at Urbana-Champaign. Two samples were provided for the corrosion study. The first was an unstressed specimen which was cut from the corner of a “pull tab.” The second sample was a stressed sample also cut from a second “pull tab” which had been subjected to a pulling force until it fractured completely.

Haynes Alloys

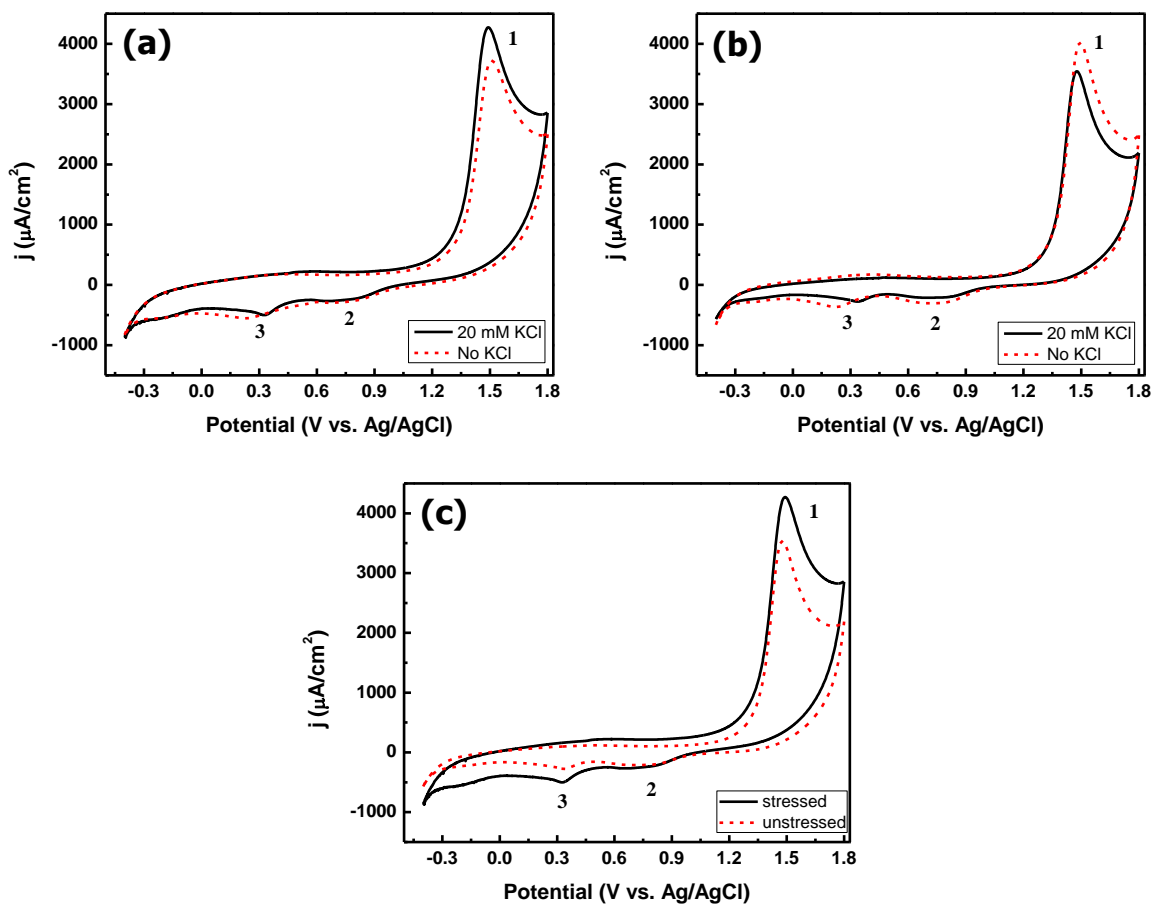
Samples of Haynes Alloys 230 and 617 were acquired from Professor James Stubbins in the Nuclear Engineering department at the University of Illinois at Urbana-Champaign. The samples were divided into three categories. The first types of sample were those that were kept as they were received. The second types of samples were heated at 900°C for 3000 hours. The third types of samples were heated at 1000°C for 3000 hours.



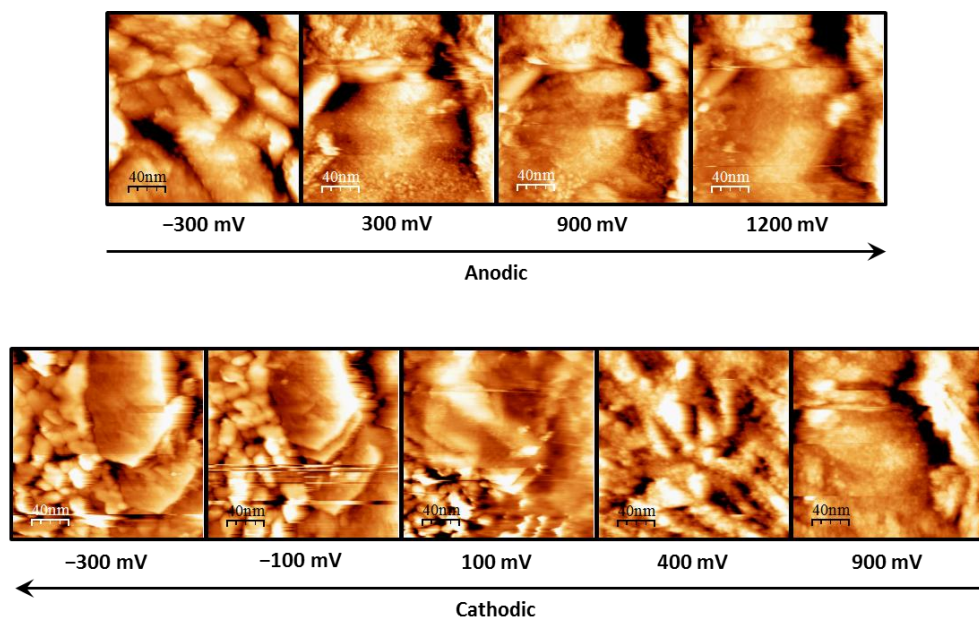
Appendix Figure A.1: (a) Voltammetry of an unstressed 316L stainless steel sample immersed in a 0.1 M HClO_4 solution. (b) Voltammetry of an unstressed 316L stainless steel sample immersed in a 0.1 M HClO_4 + 20 mM KCl solution.



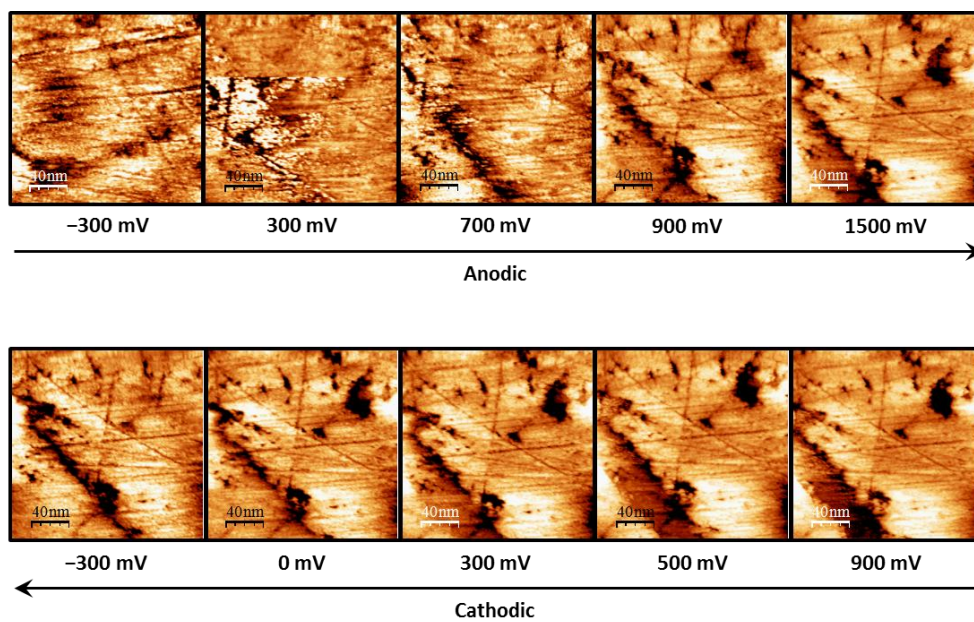
Appendix Figure A.2: (a) Voltammetry of a stressed 316L stainless steel sample immersed in a 0.1 M HClO_4 solution. (b) Voltammetry of a stressed 316L stainless steel sample immersed in a 0.1 M $\text{HClO}_4 + 20 \text{ mM KCl}$ solution.



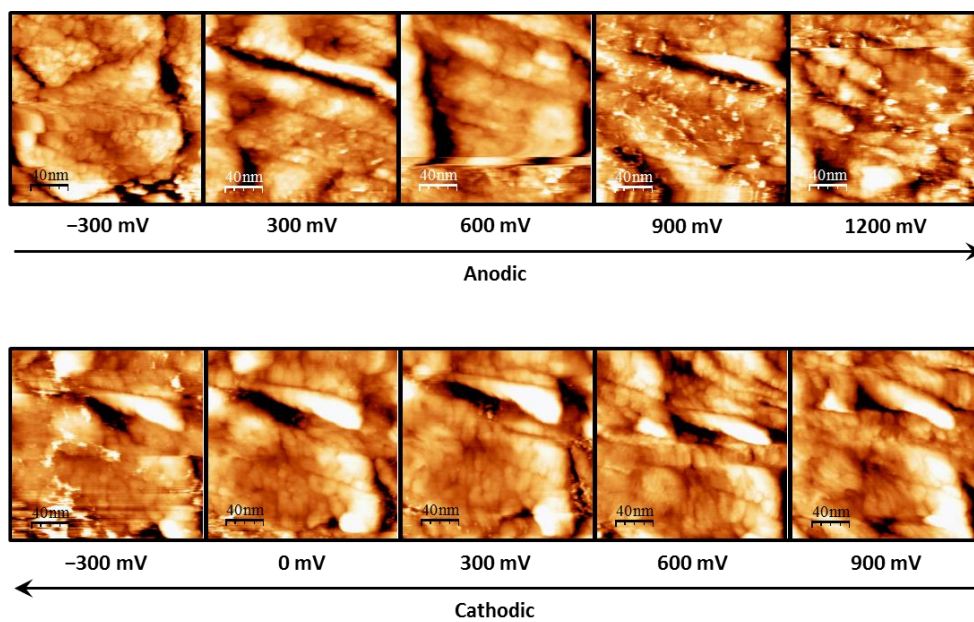
Appendix Figure A.3: Voltammetric comparison of single crystalline 316L stainless steel samples immersed in a 0.1 M HClO_4 solution or a 0.1 M HClO_4 + 20 mM KCl solution, and obtained at a scan rate of 100 mV/s. (a) The effect of Cl^- on the unstressed 316L stainless steel sample. (b) The effect of Cl^- on the stressed stainless steel sample. (c) Comparison of the voltammetry of the stressed and unstressed samples immersed in the Cl^- containing solution.



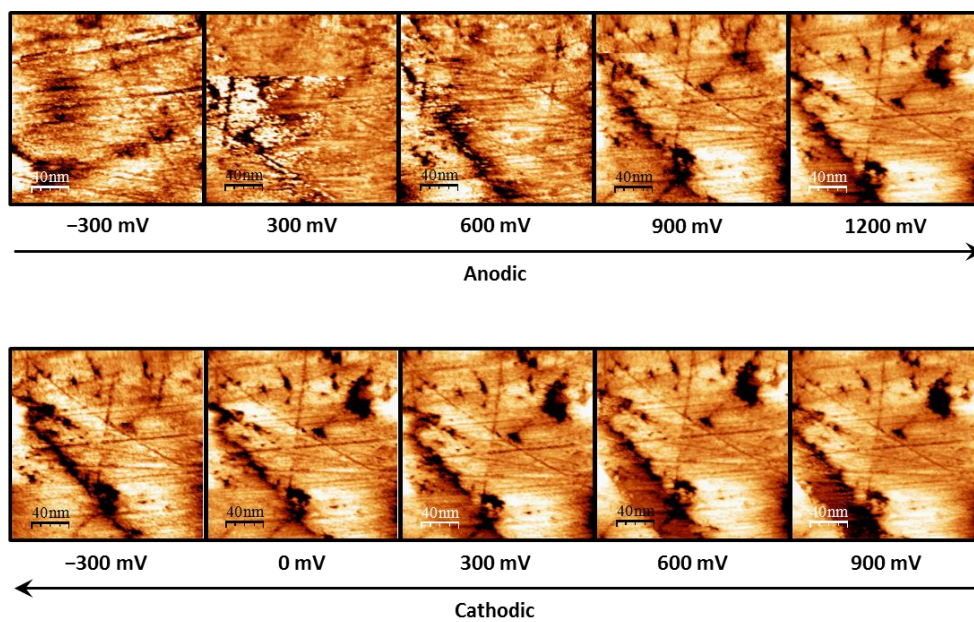
Appendix Figure A.4: EC-STM images of single crystalline 316L stainless steel immersed in a 0.1 M HClO_4 solution.



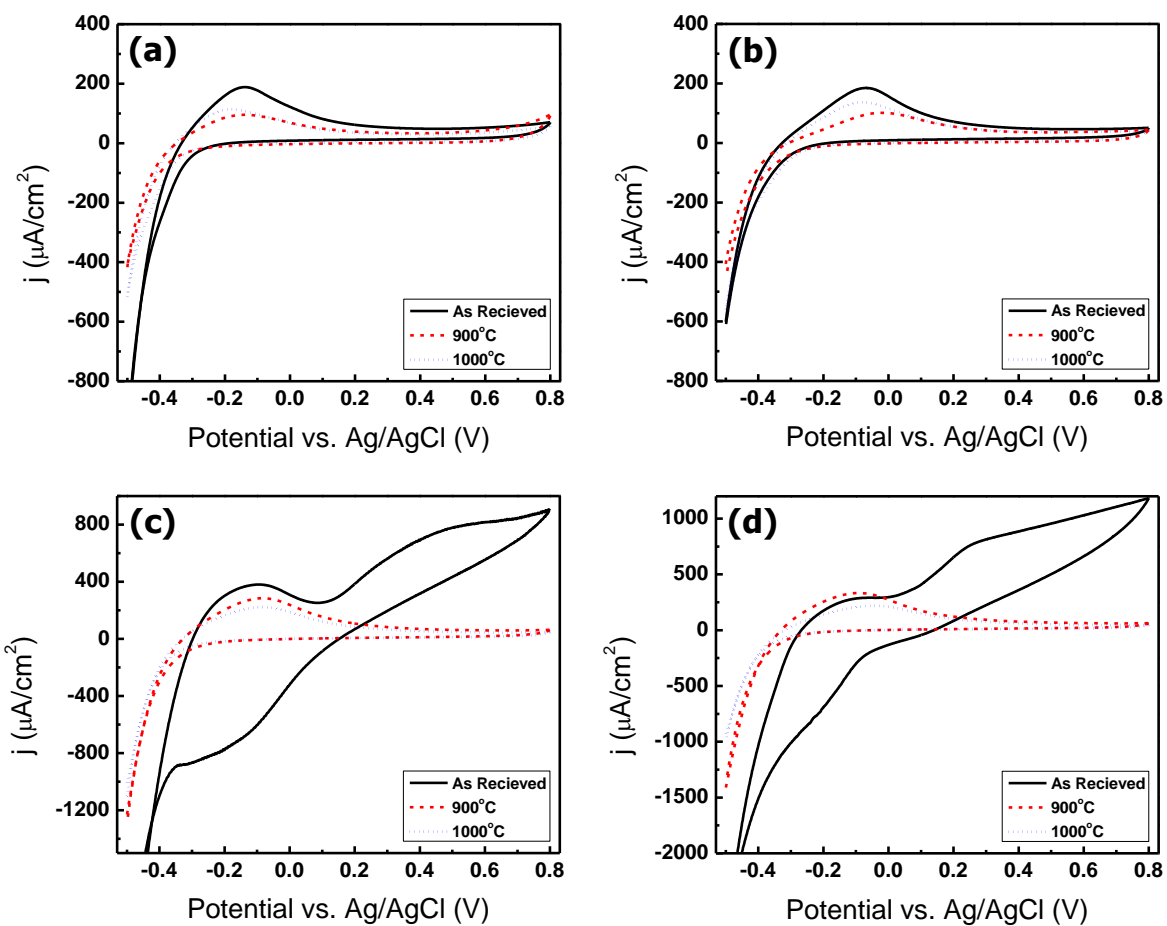
Appendix Figure A.5: EC-STM images of single crystalline 316L stainless steel immersed in a 0.1 M HClO_4 solution containing 20 mM KCl.



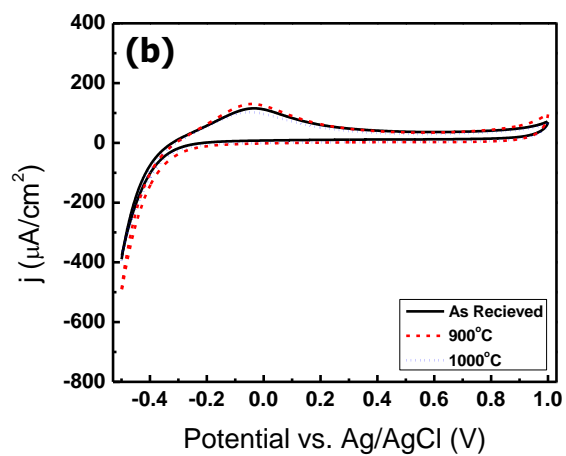
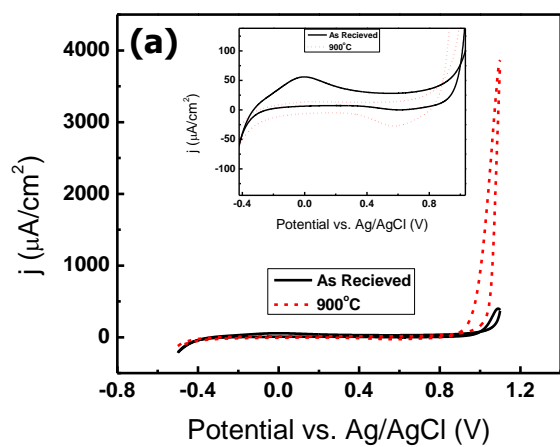
Appendix Figure A.6: EC-STM images of a stressed 316L stainless steel sample immersed in a 0.1 M HClO₄ solution.



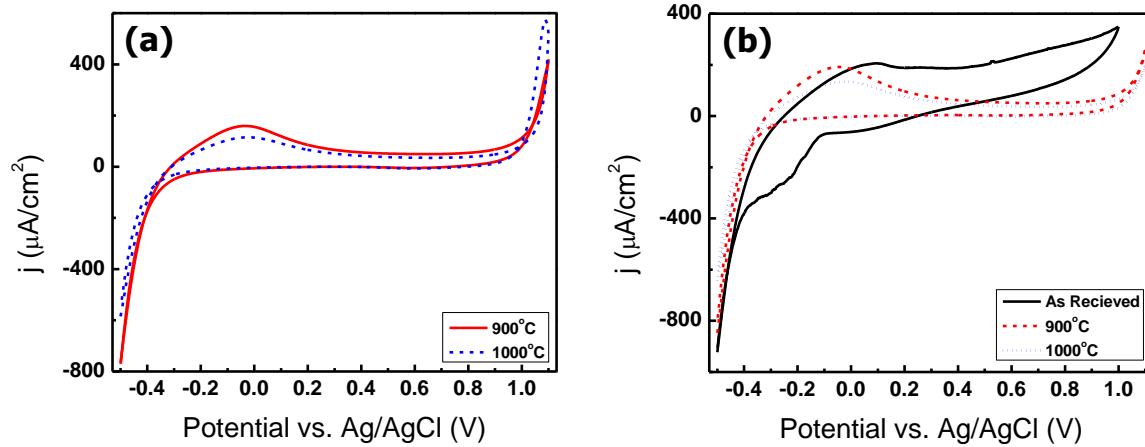
Appendix Figure A.7: EC-STM images of a stressed 316L stainless steel sample immersed in a 0.1 M HClO_4 solution containing 20 mM KCl.



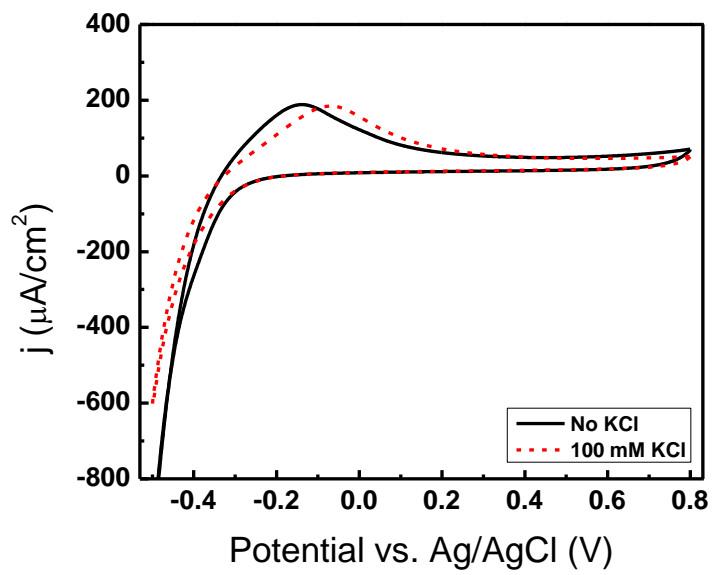
Appendix Figure A.8: Voltammetry of Haynes Alloys 230 and 617 immersed in 0.1 M H_2SO_4 with, (a) and (c), and without, (b) and (d), the addition of 0.1 M KCl. The scan rate was 50 mV/s. Each graph compares three samples of each alloy which have been heated for 3000 hrs at 900 C, 1000 C, or “as received” (unheated). (a) and (b) show voltammetric data of Haynes Alloy 230. (c) and (d) show voltammetric data of Haynes Alloy 617.



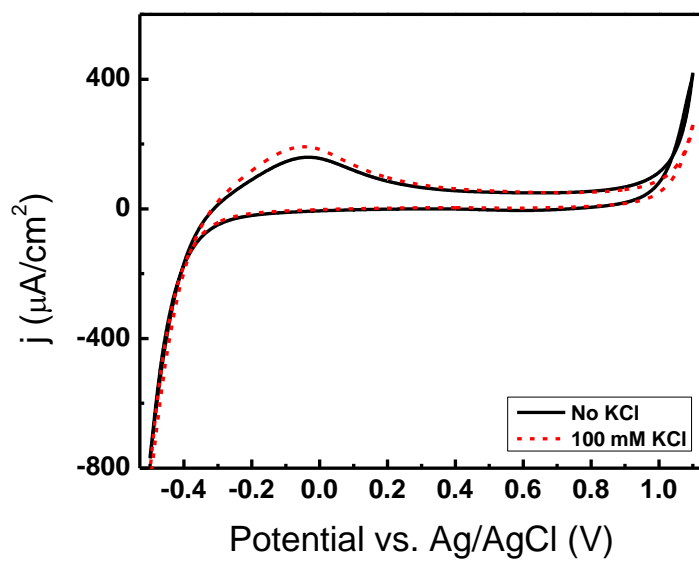
Appendix Figure A.9: Voltammetry of Haynes Alloy 230 immersed in immersed in 0.1 M H_2SO_4 with (a) and without (b) the addition of 0.1 M KCl extending the potential range upto 1.1 V vs. Ag/AgCl.



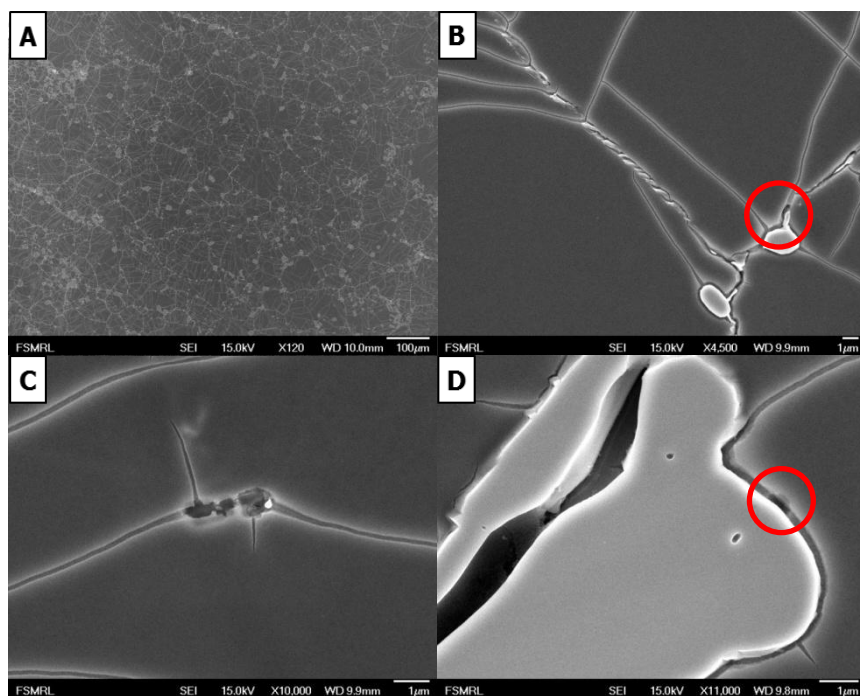
Appendix Figure A.10: Voltammetry of Haynes Alloy 617 immersed in immersed in 0.1 M H₂SO₄ with (a) and without (b) the addition of 0.1 M KCl extending the potential range upto 1.1 V vs. Ag/AgCl. 50 mV/s scan rate.



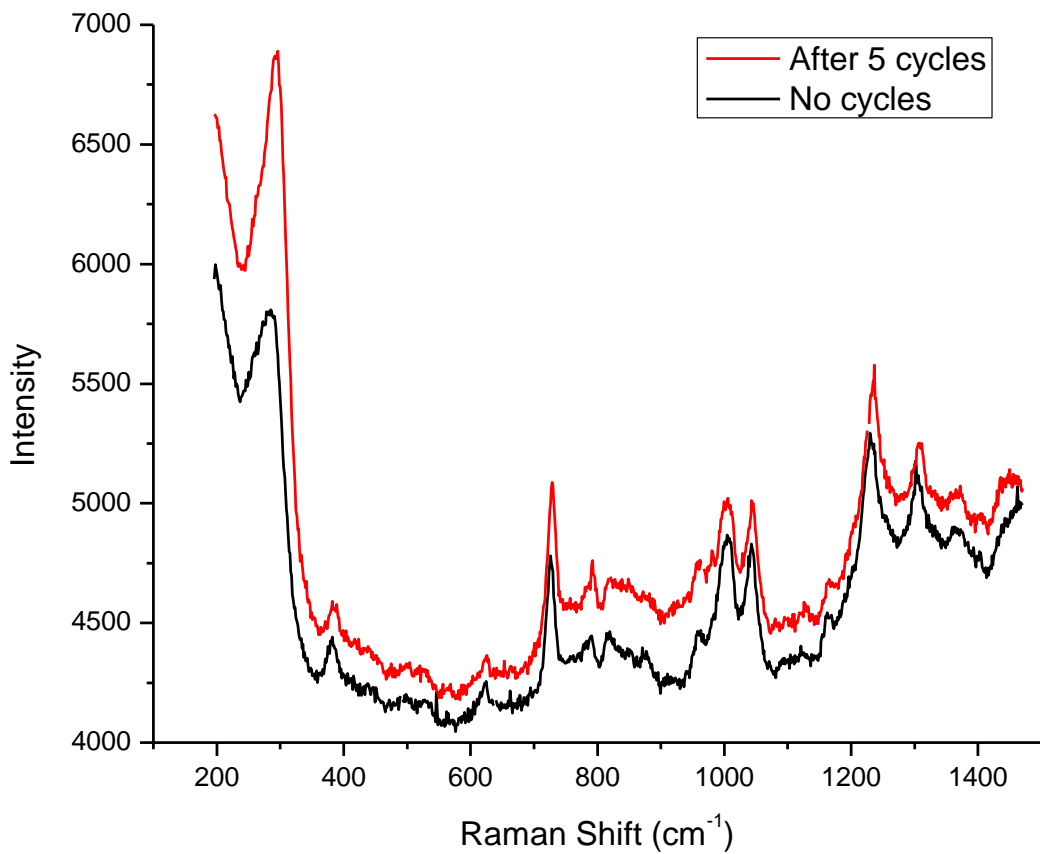
Appendix Figure A.11: Comparison of the Haynes Alloy 230 immersed in immersed in immersed in 0.1 M H_2SO_4 with the addition of 0.1 M KCl at a scan rate of 50 mV/s.



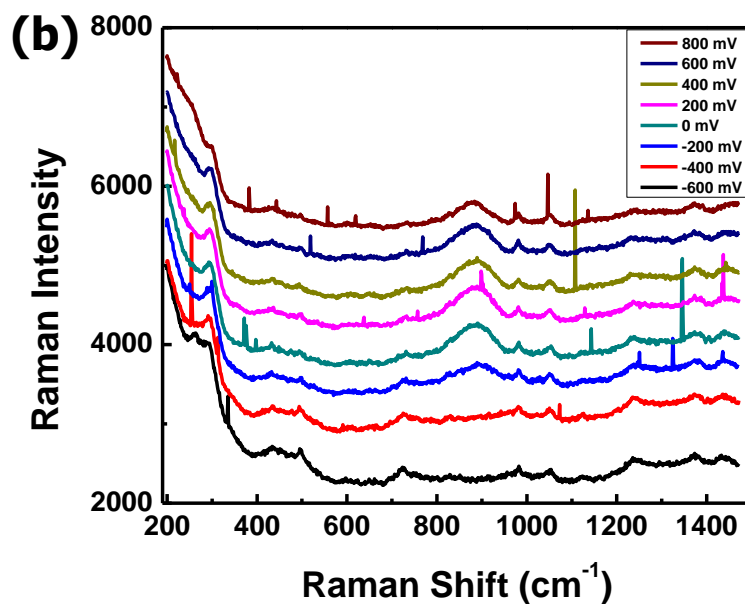
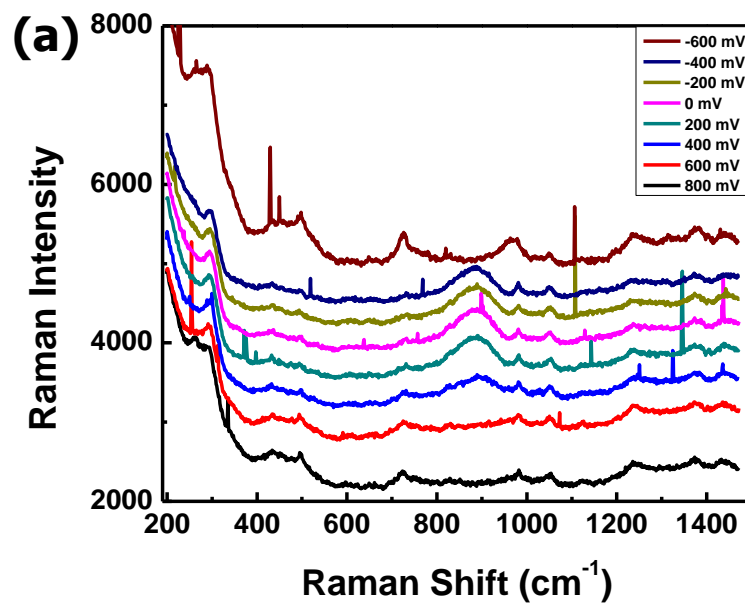
Appendix Figure A.12: Comparison of the Haynes Alloy 617 immersed in immersed in immersed in 0.1 M H_2SO_4 with the addition of 0.1 M KCl at a scan rate of 50 mV/s.



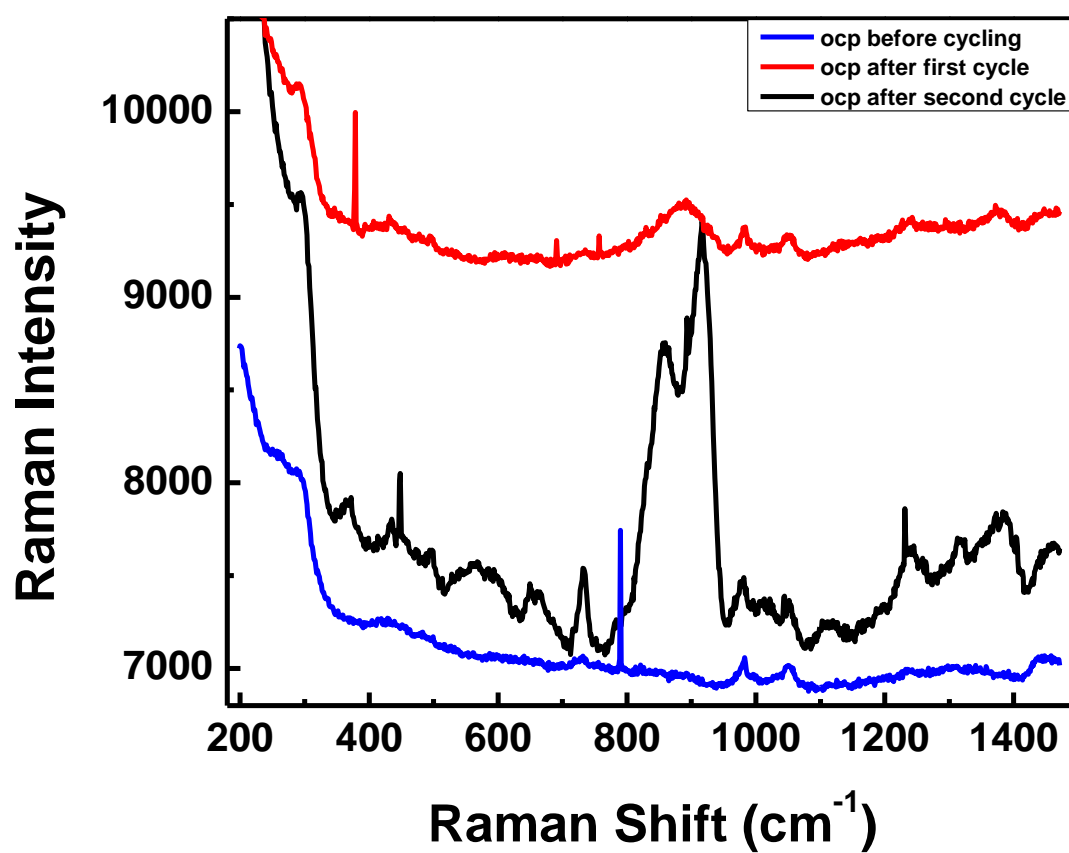
Appendix Figure A.13: Images of Haynes alloy 230 after exposure to 0.1 M H_2SO_4 and held at a potential of 0.98 V vs. Ag/AgCl for 5 minutes. Image A shows a large area of the surface. The surface contains numerous precipitates and fine crack features. The fine cracking features emanate from the precipitates. Images B, C, and D, show close-ups of the features. In all of the images fine cracks are observed. Pit formation originates in the cracks near precipitates as can be observed in images B, C, and D (red circles in B and D).



Appendix Figure A.14: Raman spectra obtained from Haynes Alloy 230 immersed in 0.1 M H₂SO₄ with the use of SHINNERS. Both spectra were obtained at open circuit potential (ocp). The black spectrum was acquired first while the red spectrum was acquired after cycling between -0.5 and 1.2 V five times.



Appendix Figure A.15: Raman spectra obtained from Haynes Alloy 230 immersed in 0.1 M H_2SO_4 with the use of SHINNERS. (a) The potential was scanned anodically from -600 mV to 800 mV vs. Ag/AgCl. (b) The potential was scanned cathodically from 800 mV to -600 mV vs. Ag/AgCl.



Appendix Figure A.16: Raman spectra obtained from Haynes Alloy 230 immersed in 0.1 M H₂SO₄ with the use of SHINNERS. Both spectra were obtained at open circuit potential (ocp). Each spectrum was collected after consecutive cycles.

Appendix B. Roughening Macros

Au Roughening Macro

```
ûtech:lsv
```

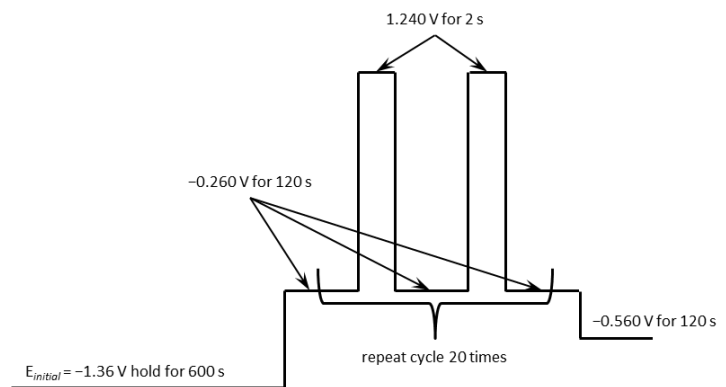
```
pcon  
pce1:-1.36  
pct1:600  
ei:-1.36  
ef:-.26  
v:0.75  
sens:1e-2  
qt:0  
run
```

```
pcon  
pce1:-0.26  
pct1:120  
ei:-0.26  
ef:1.24  
v:0.75  
sens:1e-2  
qt:0  
run
```

```
pcon  
pce1:1.24  
pct1:2  
ei:1.24  
ef:-.26  
v:0.75  
sens:1e-2  
qt:0  
run
```

```
for: 20
```

```
pcon  
pce1:-0.26  
pct1:30  
ei:-0.26  
ef:1.24  
v:0.75  
sens:1e-2  
qt:0  
run
```



Appendix Figure B.1: Schematic of the potential cycling program for roughening of Au electrodes.

```

pcon
pce1:1.24
pct1:2
ei:1.24
ef:-.26
v:0.75
sens:1e-2
qt:0
pce1:1.24
pct1:3
run

```

```

next
pcon
pce1:-.56
pct1:120
ei:-.46
ef:-.56
v:0.75
sens:1e-2
qt:0
run

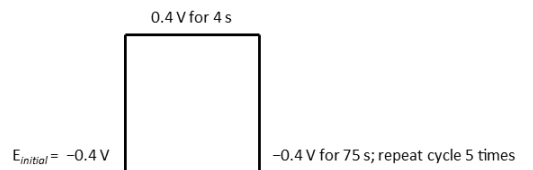
```

Cu Roughening Macro

```

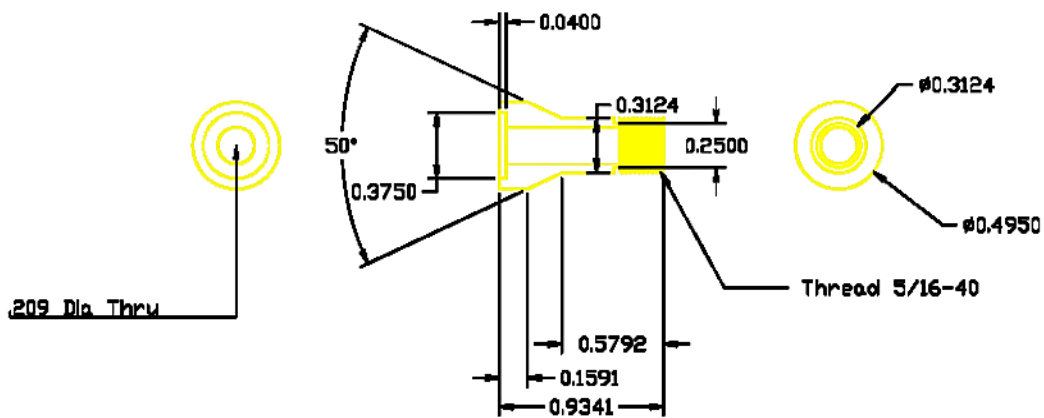
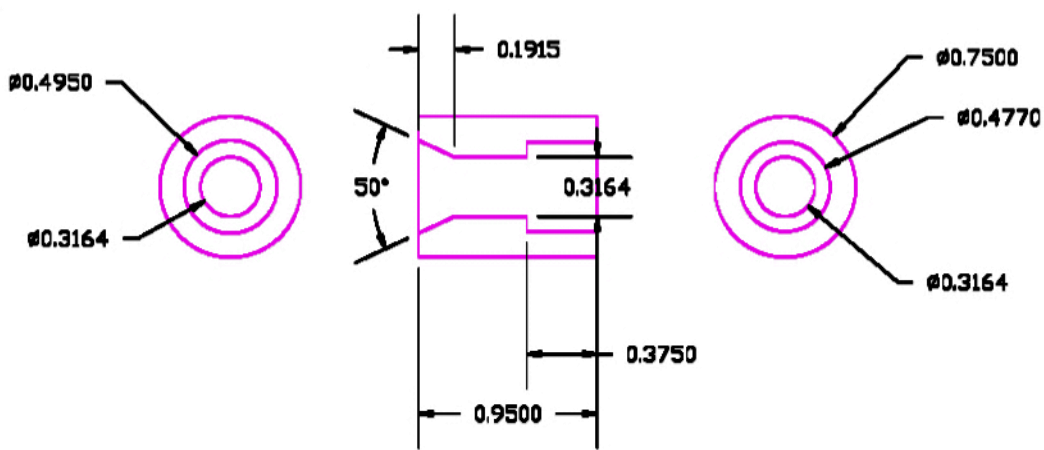
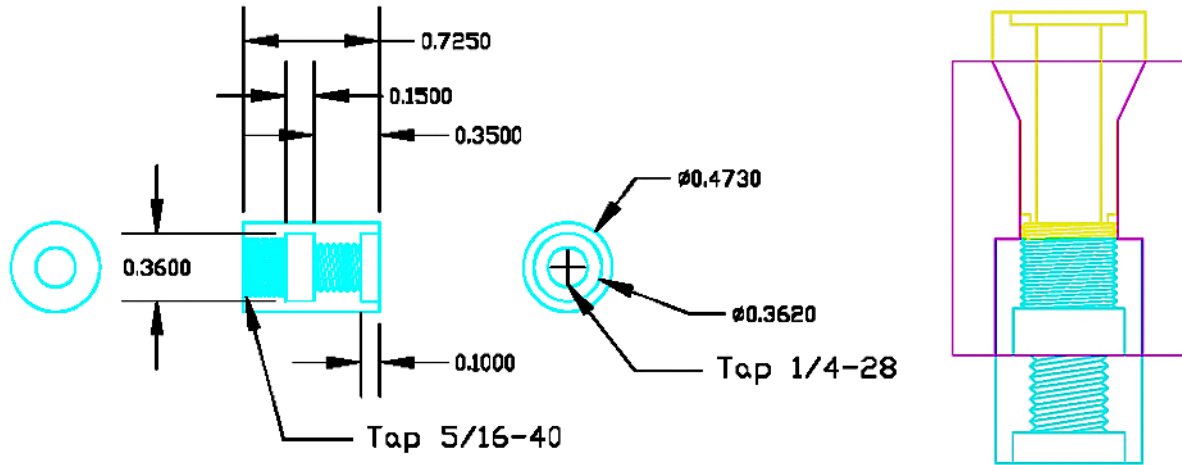
Y tech: step
sens: 1e-2
qt=0
ei=-0.4
es1=0.4
st1=4
es2=-0.4
st2=75
for:5
run
next

```

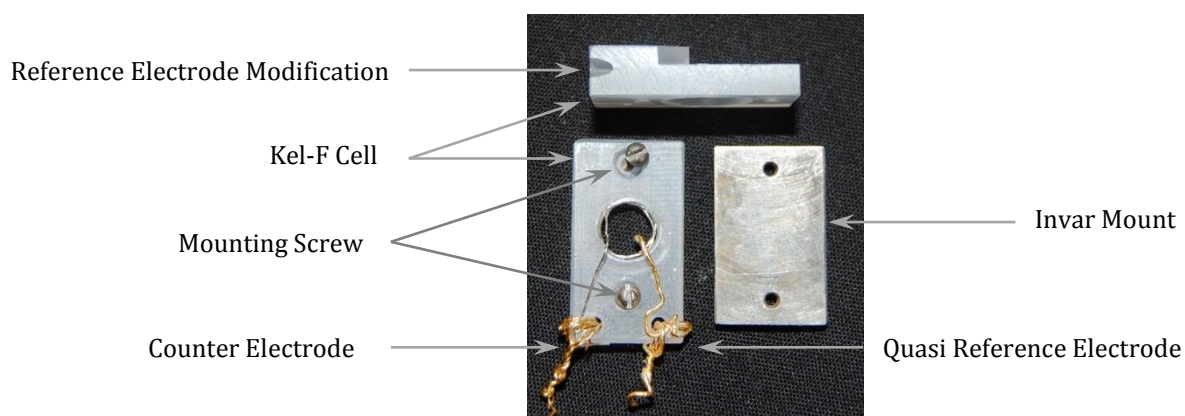


Appendix Figure B.2: Schematic of the potential cycling program for roughening Cu electrodes.

Appendix C. Collet Design for Rotating Experiments

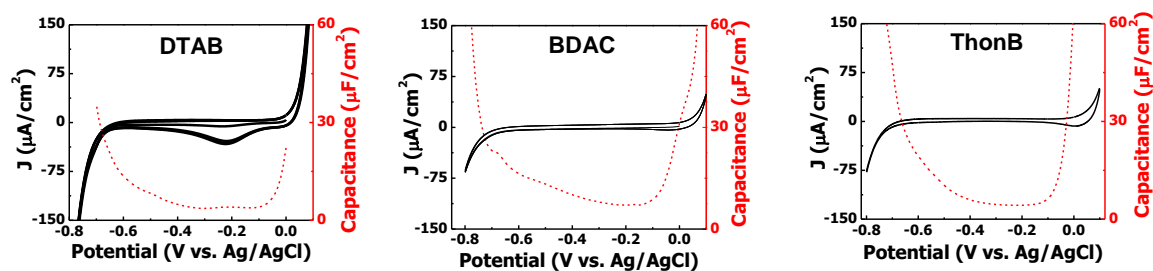


Appendix D. EC-STM Fluid Cell



Appendix Figure D.1: The EC-STM fluid cell is made of Kel-F and held in place via two screws. The cell also functions as a clamp which holds the sample onto the invar mount. The counter and reference electrodes are attached to the cell; care is taken to ensure that they do not touch one another. The top cell has been modified so that a “no-leak” Ag/AgCl reference electrode can be utilized instead of a quasi-reference electrode wire.

Appendix E. Supplemental Information to Chapter 4



Appendix Figure E.1: Cyclic voltammetry overlaid with differential capacitance measurements of a Cu(poly) disk immersed in a solution containing 0.1 M H_2SO_4 + 10 ppm of one of the following levelers: dodecyltrimethyl ammonium bromide (DTAB), benzyltrimethylhexadecyl ammonium chloride (BDAC), or thonzonium bromide (ThonB). Differential capacitance curves were collected while the potential was swept in the cathodic direction. The excitation frequency was 25 Hz and the amplitude was 10 mV.

Author's Curriculum Vitae

Education

Ph.D. Chemistry 2011

University of Illinois at Urbana-Champaign, Urbana, IL

Dissertation:

In-Situ Electrochemical Spectroscopy and Probe Microscopy Studies of Electrodeposition

Advisor: Professor Andrew Gewirth

B.S. Chemistry, Magna Cum Laude 2004

University of New Mexico, Albuquerque, NM

Advisor: Dr. David Keller

A.A. Liberal Arts, With Honors 2002

Albuquerque Technical Vocational Institute CC, Albuquerque, NM

Research Related Experience

Graduate Research Assistant 2005-Current

University of Illinois at Urbana-Champaign, Urbana, IL

- Utilized EC-STM, EC-AFM, SERS, and electrochemical methods to characterize the electrochemical deposition of chromate on Au
- Studied corrosion of novel stainless steel using EC-STM and electrochemical methods
- Studied effect of plating levelers on copper surface SERS and electrochemical methods
- Trained other lab associates in use of SERS and EC-STM

Temporary Staff Employee/Intern 2004-2005

Sandia National Labs, Albuquerque, NM

- Synthesized metal nanoparticles for use in our group
- Used air sensitive chemistry techniques (schlenk line and glove box manipulations)
- Carried out chemical analysis of synthetic products using UV-Vis, IR, and chromatography

Undergraduate Research Assistant 2004

University of New Mexico, Albuquerque, NM

- Carried out site-directed mutagenesis of HIV reverse transcriptase
- Performed purification of plasmid DNA
- Expressed plasmid DNA using an E. coli cell line
- Harvested HIV reverse transcriptase from cell line
- Analyzed data from fret experiments

Publications

Hatch, Jeremy J.; Wiley, Mark J.; Gewirth, Andrew A. "Influence of Aromatic functionality on Quaternary Ammonium Levels for Cu Plating" *Journal of the Electrochemical Society*, **2011**, 158, D323-D329

Thorum, Matthew S.; Anderson, Cyrus A.; Hatch, Jeremy J.; Campbell, Andrew S.; Marshall, Nicholas M.; Zimmerman, Steven C.; Lu, Yi and Gewirth, Andrew A. "Direct, Electrocatalytic Oxygen Reduction by Laccase on Anthracene-2-methanethiol-Modified Gold" *J. Phys. Chem. Lett.*, **2010**, 1, 2251-2254

Hatch, Jeremy J.; Gewirth, Andrew A. "Potential Dependent Chromate Adsorption on Gold" *Journal of the Electrochemical Society*, **2009**, 156, D497-D502

Theodore P Ortiz, Jason A Marshall, Lauren A Meyer, Ryan W Davis, Jed C Macosko, Jeremy Hatch, David J Keller, James A Brozik "Stepping Statistics of Single HIV-1 Reverse Transcriptase Molecules During DNA Polymerization" *J. Phys. Chem. B*, **2005**, 109, 33, 16127-31

Other Professional Experience

Graduate Teaching Assistant 2005-2006

University of Illinois at Urbana-Champaign, Urbana, IL

General Chemistry classes and labs – 2 semesters, 3 sections/semester, approximately 120 students/semester

Quantitative Analysis lab – Head lab T.A.; in addition taught 1 section, approximately 20 students

- Demonstrated proper lab technique and safety
- Created and graded quizzes, maintained electronic grade book
- Prepared stock chemicals and demonstrations for classes and labs
- Substituted for professors as needed

Student Intern 2003-2004

New Mexico State Scientific Lab Division, Albuquerque, NM

- Performed sample extraction and analysis
- Carried out the analysis of water samples using HPLC and GC/MS
- Tracked chemical and supply inventory for the lab

Fab Operator 2000-2001

Phillips Semiconductors Inc., Albuquerque, NM

- Knowledge of clean room protocol
- Operated diffusion wet stations and furnaces
- Worked in a team to maintain and improve operating standards

Technical Skills

- Electrochemical Scanning Tunneling Microscopy
- Electrochemical Atomic Force Microscopy
- Surface Enhanced Raman Spectroscopy
- Electrochemical Measurement Techniques
- UV-Vis Spectroscopy
- IR-Spectroscopy
- Instrumental Laser/Optic Design
- Software: Origin, Spartan 08/10, Nanoscope 5.4r1, WSxM, Endnote, Materials Studio, Andor Idus, Office 2003/2007
- Other: Clean room experience, forklift operation

Awards and Honors

List of Teachers ranked as excellent by their students	2006
Dr. Thomas Whaley Endowed Memorial Scholarship	2004
Dean E. Uhl Award	2003
Golden Key International Honor Society member	2003
UNM's Dean's List	2002, 2004
L. B. Reeder Scholarship	2002
Vice President's Honor Roll	2002
The National Dean's List	2001-2002
Phi Theta Kappa International Honor Society member	2001
Eagle Scout	1997